universität
wien

MASTERARBEIT / MASTER'S THESIS

Titel der Masterarbeit / Title of the Master's Thesis

Optical diffraction mechanisms for molecules at DUV light gratings

verfasst von / submitted by

Richard Ferstl, BSc

angestrebter akademischer Grad / in partial fulfilment of the requirements for the degree of

Master of Science (MSc)

Wien, 2023 / Vienna, 2023

Studienkennzahl lt. Studienblatt / degree programme code as it appears on the student record sheet:	A 066 876
Studienrichtung lt. Studienblatt / degree programme as it appears on the student record sheet:	Masterstudium Physics UG2002
Betreut von / Supervisor:	Univ.-Prof. Dr. Markus Arndt

Abstract

Interactions between light and matter define the way we can study and control small systems like atoms, molecules and nanoparticles. For many applications involving such objects it is necessary to design tools which utilize such interactions. Matter-wave experiments exploring the limits of quantum superposition need such tools to realize diffraction gratings for molecules, metal clusters and proteins. There are however many ways in which photons can interact with such composite objects. This leads to a variety of grating mechanisms which can be applied to matter-wave interferometry. Which ones are relevant depends on the properties of the particular system. It turns out that ultra violet (UV) light, often yields interesting and useful interactions for the particles one would like to study. Higher photon energies can result in photochemical processes like photocleavage, photoionization or photoisomerization. These interactions present the possibility of realizing new grating mechanisms. On the other hand, optical properties of the molecules themselves are usually not as well known in the deep UV region, in particular for the gas phase. In general conventional methods for such measurements in the gas phase are met with a number of complications when attempting to extract absolute values. Measurements in solution on the other hand are subject to influences of the solvents.

Here we use $1\,\mathrm{W}$ of UV light at $266\,\mathrm{nm}$ to form the diffracting element in a far-field matter-wave interferometer for molecules. By testing this setup on a selection of different molecules we study the influence of different interactions between the molecules and the light grating. We demonstrate how the optical properties of the molecules at this wavelength, namely the mean electric dipole polarizability and the absorption cross-section, can in principle be estimated from such a diffraction experiment. To do this we also present a theoretical model for the experiment, which is able to give good reproductions of the observed data. Furthermore we present diffraction measurements of a molecule functionalized with photocleavable groups. We use our theoretical model to show a strong indication that we can realize a photocleavage grating for molecules this way, introducing a novel grating mechanism for matter-wave diffraction. Because of the variety of properties for the molecules we present here, we can see directly how the different mechanisms influence diffraction measurements. Finally we will also present a molecule which may have the necessary properties to realize a photoisomerization grating in the near future.

This thesis begins with a brief historical retrospective on the field of matter-wave interferometery. We will then study the molecular properties, which are relevant for the measurements presented here in more detail. The experimental setup and its components will be discussed in the following sections, after which the theoretical model will also be analyzed. The results of the diffractions experiments will be compared both quantitatively and qualitatively with simulations based on this model.

Zusammenfassung

Interaktionen zwischen Licht und Materie definieren, auf welche Art kleine Systeme, wie Atome, Moleküle und Nanoteilchen, untersucht und kontrolliert werden können. Viele der Anwendungen, die auf solche Systeme zurückgreifen, erfordern Werkzeuge, die auf diesen Interaktionen basieren. Materiewellen-Experimente, die die Gültigkeitsgrenzen von Quantensuperposition ausloten, brauchen solche Interaktionen beispielsweise, um Beugungsgitter für Moleküle, Metall Cluster und Proteine zu realisieren. Es gibt jedoch zahlreiche Interaktionsmöglichkeiten zwischen solch komplexen Objekten und Photonen. Daraus ergeben sich auch viele verschiedene Gittermechanismen, die in der Materiewellen-Interferometrie angewendet werden können. Welche davon relevant sind, hängt von den Eigenschaften des spezifischen Systems, das im Interferometer verwendet wird, ab. Für viele Teilchen mit vielversprechenden Anwendungen in diesem Bereich gibt es zahlreiche interessante Interaktionen mit ultraviolettem (UV) Licht. Die höheren Energien der UV Photonen erlauben es, dass photochemische Prozesse, wie Photospaltung, Photoionisation oder Photoisomerisierung, stattfinden. Solche Interaktionen können als Grundlage für neue Gittermechanismen dienen. Weiters sind Eigenschaften der Moleküle selbst im tiefen UV Bereich in der Regel weniger gut bekannt. Das ist insbesondere der Fall für die Gasphase, in der mit konventionellen Messmethoden in der Regel nur schwer Absolutwerte bestimmt werden können. Messungen in Lösung werden hingegen vom verwendeten Lösungsmittel beeinflusst.

Diese Arbeit präsentiert ein $1\,\mathrm{W}$ UV Lichtgitter mit $266\,\mathrm{nm}$ Wellenlänge als Beugungselement in einem Fernfeld Materiewellen-Interferometer für Moleküle. Anwendung dieses Interferometers mit einer Auswahl an verschiedenen Molekülen demonstriert den Einfluss der verschiedenen Interaktionen zwischen dem Lichtgitter und den Teilchen auf die Beugungsmessungen. Es wird gezeigt, dass gewisse optische Eigenschaften der Moleküle im UV, insbesondere die mittlere elektrische Polarisierbarkeit und der Absorptionsquerschnitt, aus solchen Messungen prinzipiell extrahiert werden können. Als Grundlage dafür dient ein theoretisches Modell, das es erlaubt, solche Beugungsmessungen vorherzusagen. Außerdem werden Beugungsmessungen eines Moleküls gezeigt, welches mit photospaltbaren Funktionellen Gruppen modifiziert wurde. Das theoretische Modell gibt starke Indizien dafür, dass mit diesem Molekül ein Photospaltgitter in diesem Experiment realisiert wird. Somit wird ein neuer Gittermechanismus für Materiewellen-Interferometrie demonstriert. Die stark verschiedenen Eigenschaften der Moleküle, die in dieser Arbeit untersucht werden, erlauben es auch, direkt zu sehen, auf welche Weise die verschiedenen Gittermechanismen die Beugungsmessungen beeinflussen. Ein weiteres Molekül, dessen Eigenschaften es in der nahen Zukunft ermöglichen könnten, ein Photoisomerisierungsgitter zu realisieren, wird als Abschluss vorgestellt.

Diese Arbeit beginnt mit einem kompakten Rückblick auf die Geschichte der Materiewellen-Interferometrie. Danach werden die Eigenschaften von Molekülen, die für die hier präsentierten Messungen relevant sind, vorgestellt. Die darauffolgenden Abschnitte beschreiben den Versuchsaufbau und seine Komponenten, im Anschluss wird auch das theoretische Modelle erklärt. Simulationen, die auf diesem Modell basieren, werden sowohl qualitativ als auch quantitativ mit den experimentellen Ergebnissen verglichen.

Contents

1. Introduction

A central element to any kind of interferometer is a coherent beam splitting mechanism. Developing methods which achieve this with the necessary coherence and efficiency is still one of the many challenges in molecular matter-wave interferometry. The internal complexity of large composite systems such as molecules means that many of the well refined beam splitting methods of atom interferometry are not easily adapted for this application. Nevertheless there has been a continuous stream of new developments over the past years, a recent examples being Bragg diffraction of molecules [1], nanomechanical gratings as thin as a single layer of atoms [2] and optical ionization gratings [3]. Many of the methods, which are currently being used, have in common that the rely on the interaction of the particles with light. Even though these interactions are less well defined than for atoms, there are many ways in which they are useful for diffraction experiments with composite objects. In particular compared to material gratings their perfect periodicity, high transmission and the impossibility of e.g. clogging makes gratings made of light very attractive [4]. Which interactions occur between the molecules and the light grating however can vary a lot depending on the details of the systems involved. This is fascinating because it not only allows us to study a range of different effects but also because it can result in entirely new grating mechanisms. It turns out that it would be beneficial for several interesting application to use UV light to form the light gratings. This is the case for current prospects for high-mass interferometry using metal clusters [5–7], but UV light is also of interest for smaller biological molecules where it can cause a variety of different effects. In the next section we will take a closer look at some of these mechanisms, which can occur at a light-grating.

1.1. Optical grating effects

The effects a molecule experiences when being diffracted at an optical grating depend both on the properties of the molecule itself and the parameters of the grating. A selection of the most important effects at thin optical gratings is sketched in figure 1.1. Most phenomena are connected to the absorption of photons in the grating. However, even if effectively no absorption occurs the standing light wave can still act as a phase grating (figure 1.1a). In this case the dipole potential proportional to the mean polarizability $\bar{\alpha}$ of the molecule imprints a periodic phase shift onto the molecular wavefunction [8]. If the absorption cross-section σ is non-negligible the effects of absorption also become relevant. In the simplest case the absorption effectively only raises the internal temperature of the molecule but does not result in a change of the chemical structure (figure 1.1b). The effect of such an absorption grating is twofold. For the class of molecules with the initial internal temperature the absorption in the antinodes of the standing light wave results in the light grating effectively only being transmissive in the regions of the nodes. The standing light wave thus acts similar to a material absorptive mask for this class of molecules. Molecules which undergo absorption get heated to a higher temperature class. They are however still mutually coherent and give contributions to the far-field diffraction in the form of additional peaks [9]. The detectors which are currently being used are not sensitive to the internal temperature of the molecules, thus these two contributions cannot be distinguished directly. The two effects (figure 1.1a,b) are directly dependent on the properties $\bar{\alpha}$ and σ of the molecules. These properties in turn are also frequency dependent. Learning more about such molecular properties in the UV region is particularly interesting for smaller bio molecules, many of which have strong transitions in the UV or show other interesting photophysical behaviour in this spectral region [10]. One of the aims of this work is to present results in which the phase grating and absorption grating effects are the main contributors and where we can use them to estimate optical properties of the molecules.

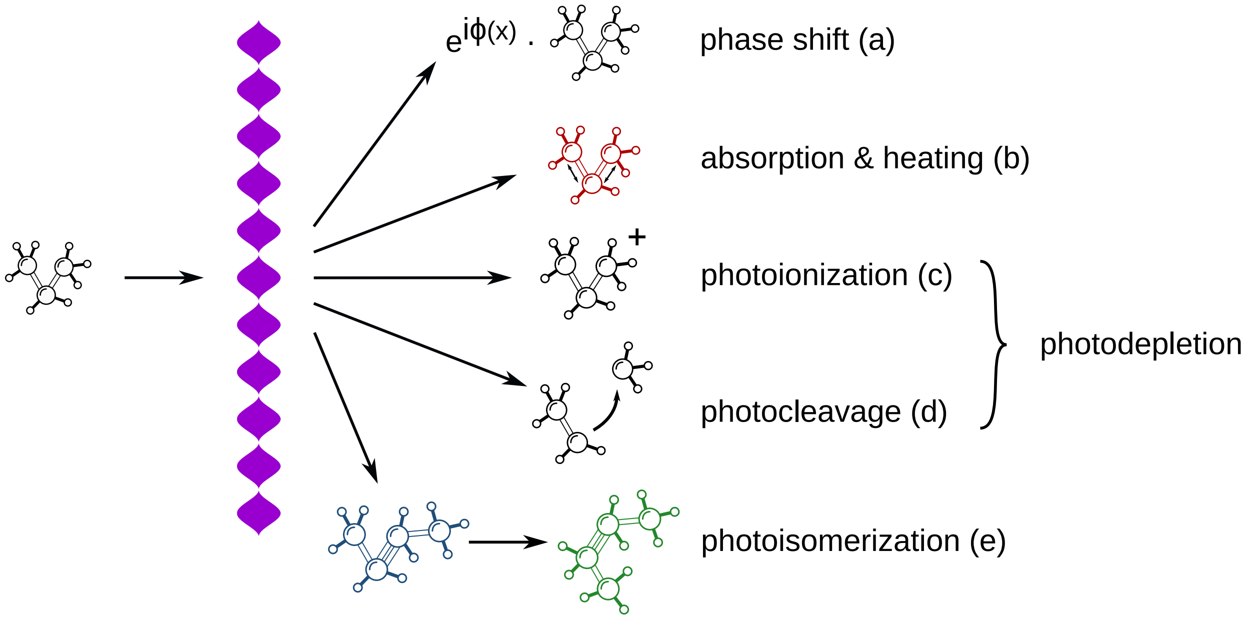

Figure 1.1: Overview of the most important optical grating mechanisms in molecular matter-wave interferometry for thin light gratings.

Absorption of photons in a light grating can however have other effects, which result in a more drastic change in the molecular structure. Because of their high energy UV photons can lead to photoionization of some molecules (figure 1.1c). This process has been used with pulsed $157\,\mathrm{nm}$ light gratings to realize a matter-wave interferometer in the time-domain [3]. Ionization of metal clusters using continuous wave (cw) UV lasers is the grating mechanism used for the aforementioned current efforts in high-mass interferometry with metal clusters [5]. A similar process is the one of photocleavage (figure 1.1d). Here absorption of a photon leads to the removal of an entire functional group from the molecule. Such leaving groups are often active in the UV and designing leaving groups which also absorb at longer wavelengths remains a challenging task [11]. For matter-wave interferometry photocleavage presents a new kind of grating mechanism which has interesting prospects for future interference experiments with biological molecules. In this work we present first results of diffraction experiments with molecules where we have strong indications that photocleavage occurs. Both photoionization and photocleavage gratings act as photodepletion gratings in the sense that molecules which absorb photons are effectively removed from the signal. In the former case this can be attributed to stray electric fields deflecting the molecules. For photocleavage the recoil from the leaving group gives a randomly oriented momentum kick to the remaining part of the molecule, which either prevents the molecules from reaching the detection at all or at most gives a more or less homogeneous background. Photodepletion grating effectively act as absorptive masks similar to material gratings. However, they do have the advantages of having a perfect periodicity and an effective opening fraction, which can be tuned by the laser power. Another phenomenon, which can occur after absorption, is photoisomerization (figure 1.1e). In this case the absorption does lead to a structural change of the molecule, which in contrast to just heating the molecule, potentially makes it distinguishable from the original one. Since the isomerization does not lead to a loss of the molecules as is the case for photodepletion gratings, we expect a photoisomarization grating to yield diffraction with contributions from both isomers.

1.2. Overview of this work

This thesis presents experimental work whose goal was to diffract a variety of (organic) molecules at $266\,\mathrm{nm}$ UV light gratings and study the involved effects. We show how the polarizability $\bar{\alpha}$ and the absorption cross-section σ can be estimated from the diffraction when the mechanisms a and b in figure 1.1 are most relevant. We also highlight some of the complications involved when e.g. the influences of fluorescence would need to be considered as well. Additionally we show a photocleavage grating with specially tailored molecules.

Section 2 starts with an in-depth view on the history of matter-wave interferometry. On the one hand to put the current experiments into the context of the many efforts of previous experimentalists and theorists, on the other hand to acknowledge the one hundred year anniversary of the very idea of matter-waves. In section 3 we will continue with a deeper look into the molecular properties, which are relevant for the effects we discussed in section 1.1. Section 4 discusses the details of the experimental setup, the procedures used and the challenges involved. We will describe the physical function and details in the implementation of the individual components. Section 4.7 will also give a summary of the molecules which are used in the experiment. In section 5 we will describe a theoretical model for the experimental setup, which will be used to analyze the experimental results. The details of this evaluation are summarized in section 6. Section 7 contains the experimental results, which are interpreted with the help of the model described in the previous two section. In section 8.1 we will discuss these results in the context of the grating mechanisms outlined in section 1.1. Finally, we present a potential candidate for photoisomerization gratings in section 8.3.

2. One hundred years of matter-waves - a historical perspective

The concept of matter-waves originates from Louis de Broglies work one century ago. His aim to extend the idea of wave-particle duality, first introduced by Einstein for light [12], led to the introduction of the *de Broglie wavelength*

$$\lambda_{dB} = \frac{h}{p} \tag{2.1}$$

which describes the wave nature of a massive particle with momentum p [13]. De Broglies ideas were soon put onto a more sound theoretical footing by Erwin Schrödinger [14]. In the last 100 years the existence of matter-waves has not only been confirmed, but they have quickly become a very useful tool for material science, precision measurements and probing the limits of quantum theory, as we will see in the following subsections. We will give a brief historical overview of the major experimental developments in matter-wave interferometry to put the work covered in this thesis into context of the many experiments that have been done before. We will review the developments from the first experiments with electrons, neutrons and atoms to more modern setups using macromolecules.

2.1. Electrons

Davisson and Germer were the first to experimentally confirm de Broglies hypothesis. They observed that the angular distribution of electrons reflected at a nickel crystal match the predictions of the matter-wave model [15, 16]. In the same year Thomson and Reid published the first demonstration of electron diffraction in transmission [17]. Electron diffraction in reflection was quickly adapted to characterize a wide range of materials. Slow electrons in particular give insight into the potential within a material [18–21]. A versions Youngs classic double-slit experiment [22] was only realized with electrons almost three decades after the first diffraction experiments. Möllenstedt and Düker were able to use a tungsten wire to create a briprism for electrons, which acted as a double slit for the electron matter-waves [23]. Jönsson took this a step further several years later and showed diffraction at a set of mechanical slits [24]. These experimental results have taken what was once considered an "imaginary experiment" and turned it into reality [25]. A more recent demonstration of the electron double-slit experiment uses electrons created by photoionization of H_2 molecules [26]. Electron matter-wave experiments have also been crucial in verifying the Aharonov-Bohm effect [27], first predicted in 1959. A number of experiments in the following years demonstrated that an electromagnetic vectorpotential enclosed in an interferometer does indeed cause a phase shift [28–31]. Another important development, which relies on the wave nature of electrons and is very relevant today, is electron microscopy. Its invention goes back to 1932 [32]. Excellent historical perspectives of this field can be found in [33–35].

Already in 1933, only a few years after the fist electron diffraction experiments, Kapitza and Dirac predicted a different kind of diffraction mechanism [36]. This *Kapitza-Dirac effect* reverses the roles of matter and light in comparison to the usual diffraction experiments. A standing light wave takes on the role of the grating at which the electron wave diffracts. As we will see in the following sections, this effect also takes on a central role in the molecular interference experiments presented here. For electrons it took until 2001 for this effect to be experimentally observed [37]. However, the high-intensity case, not showcasing coherent interference, was observed already in 1988 [38].

An impressive demonstration of the wave nature of electrons was given by Crommie et al. in 1993, who confined electrons within barriers formed by iron atoms on a metal surface, which allowed a scanning tunneling microscope (STM) to directly observe the probability densities belonging to the electronic eigenstates within this barrier [39]. Mach-Zehnder [40] and three-grating [41] interferometers have also been built for electrons. Using graphite films as phase plate [42] and holographic masks [43, 44] vortex beams of elecron matter-waves have been demonstrated. [45] gives an insight into many of the developments in electron interferometry, which could not be covered in this short section.

2.2. Neutrons

It took only four years following the discovery of the neutron in 1932 [46] for it to be used in diffraction experiments. Bragg reflection was demonstrated by Mitchell and powers [47], while Halban could show diffraction in transmission [48]. Coincidentally 1932 was also the year in which diffraction of the other nucleon, the proton, was observed [49]. The first interferometer for neutrons was built by Maier-Leibnitz and Springer in 1962 [50]. Similar to Möllenstedt and Dükers experiment they constructed a Fresnel biprism to realize double-slit interference with neutrons. Diffraction of neutrons at a single slit [51] and a grating formed by grooves in a piece of glass [52] were shown in 1969. More refined measurements of neutron diffractions at slits have been carried out by Zeilinger et al. in 1988 [53]. In 1991 neutrons were also diffracted at a phase grating [54].

The first neutron interferometer enclosing a macroscopic area was developed by Rauch et al. in 1974 [55]. This Mach-Zehnder interferometer was manufactured from a single Si-crystal. This type of neutron interferometer was quickly adapted for measuring the effects of gravity [56, 57] and demonstrating the properties of spin-$\frac{1}{2}$ systems under rotations [58]. A similar interferometer for cold neutrons has been realized via holographically written gratings [59, 60]. By entangling in the path and spin of neutrons Rauch was able to demonstrate a violation of a Bell inequality in his interferometer [61]. The violation of a similar inequality for three-partite systems was shown for a Greenberger-Horne-Zeilinger (GHZ) state of the path, spin and energy degrees of freedom of neutrons [62]. This type of entanglement has been used recently to show localization of individual properties of the neutron in interferometer arms [63]. For a more in depth look at neutron interferometer the reader is directed to Helumut Rauchs excellent book on the topic [64].

2.3. Atoms

The first diffraction experiment with atoms falls in the same time frame as for electrons in neutrons. Estermann and Stern observed the diffraction of He atoms and H_2 molecules at a variety of crystal lattices in 1929 [65, 66]. The Kapitza-Dirac effect, first introduced for electrons, also allows for atoms to be diffracted at a standing light wave [67]. David Pritchard et al. were the first to demonstrate this experimentally with sodium atoms beginning in 1983 [68, 69]. However, scattering of atoms at standing light waves was already observed two years before [70, 71]. Bragg scattering of atoms at a standing light wave was shown shortly after as well [72]. Keith et al. observed diffraction of sodium atoms at a mechanical grating made out of a gold membrane in 1988 [73]. Diffraction at a mechanical double-slit was observed by Carnal et al. in 1991 [74] and Shimizu in 1992 [75].

In 1991 Keith and Pritchard used a similar grating to their previous experiment, this time made out of silicon nitride, as a beam splitter in order to construct a Mach-Zehnder interferometer for sodium atoms [76]. A similar setup using light gratings was realized by Rasel in 1995 [77]. In 1991 two more closed Mach-Zehnder like interferometers were also first demonstrated for atoms. Following up on an idea from two years earlier [78] Bordé et al. used the recoil from 1-photon absorptions to split a molecular beam. By applying $\frac{\pi}{2}$ pulses they could create a coherent splitting, which was also labelled by the atoms internal state. Four such beamsplitters form an interferometer for Ca atoms, which was used to measure rotations [79]. Kasevich and Chu built a Mach-Zehnder interferometer which relied on 2-photon Raman transitions between hyperfine states of Sodium as a beam splitting mechanism. Similar to Bordés scheme, the photon recoil transferred momentum to the atoms and the momentum states were labelled by the internal hyperfine states. The full interferometer scheme consists of a sequence of $\frac{\pi}{2}$-π-$\frac{\pi}{2}$ Raman pulses acting on sodium atoms in a magneto-optical trap (MOT). Using this scheme Kasevich and Chu were able to measure the local gravitational acceleration with high accuracy [80]. The possibility of using atom interferometers as highly precise inertial sensors was already suggested by Clauser in 1988 [81]. Kasevich and others were able to continuously improve their measurements of gravitational acceleration and rotations since then [82–90]. Atom interferometry has also proven a useful tool for measuring atomic properties [91–95] and fundamental constants [96–99].

Weitz and Chu introduced another kind of beam splitter for atoms based on adiabatic following in 1994 [100]. A three grating interferometer based on the Talbot-Lau effect was presented by Clauser and Li in 1994 [101]. We will see in the next section that this kind of interferometer setup is very useful in molecule diffraction experiments. Bragg scattering of atoms at standing light waves, first observed in 1988 [72], has been used in beam splitters with very large momentum transfers [102–104]. There have also been experiments using holographic masks to create specific diffraction patterns of atoms [105–108]. Another significant development is the creation of atomic Bose-Einstein condensates, which was first realized in 1995 [109, 110]. Bose-Einstein condensates have been utilized in a number of interference experiments [96, 111–115].

2.4. Molecules

Even though Estermann and Stern were able to show diffraction of H_2 molecules in 1929 [65, 66], it took until the 90s for molecular interference experiments to advance further. In 1994 Schöllkopf and Toennies were able to diffract H_2 and D_2 molecules as well as small He clusters at a silicon nitride grating [116]. Also in 1994 Bordé built an interferometer for I_2 molecules similar to his 1991 design for atoms [117]. Pritchard also adapted his Mach-Zehnder interferometer for atoms from a few years before to interfere Na_2 molecules [118].

The first step beyond di- and triatomic molecules came in 1999, when Arndt et al. first showed the wave nature of a larger molecule by diffracting C_{60} at a silicon nitride grating [119]. This experiment was soon repeated with a standing light wave acting as the grating structure [8]. The basic experimental setup used in this diffraction experiment is the same as for the one presented in this work. This far-field configuration has also been further developed in the meantime. In 2012 Juffmann et al introduced single-molecule imaging to the setup [120]. This setup was also utilized for studying the interactions of molecules with material gratings [2, 121, 122]. A similar setup involving a single light grating has been used to demonstrate Bragg diffraction of molecules in 2020 [1].

Efforts to show interference of even more massive molecules have lead to the developments of near-field interferometers for molecules. A three grating configuration based on the Talbot-Lau effect [123] has proven to be favorable for such experiments. This Talbot–Lau interferometer (TLI) was first demonstrated with three gold gratings for C_{70} [124]. The same setup was used to show diffraction of tetraphenylporphyrin $C_{44}H_{30}N_4$ (TPP) and the fluorofullerene $C_{60}F_{48}$ in 2003 [125]. Static polarizabilities of molecules have been measured in such a setup via deflection [126]. A further iteration of this setup introduced a standing light-wave as one of the gratings, forming a so called Kapitza–Dirac–Talbot–Lau interferometer (KDTLI) [127, 128]. This setup also allowed for the determination of optical polarizabilities and other molecular properties [129–133]. There have also been suggestions for different methods with which one might distinguish molecular isomers via matter-wave diffraction [134, 135]. Using the KDTLI configuration interference of molecules was demonstrated with masses up to $6910\,\mathrm{u}$ in 2011 [136], more than $10\,000\,\mathrm{u}$ in 2013 [137] and finally more than $25\,000\,\mathrm{u}$ in 2019 [5]. Efforts to create Bose-Einstein condensates of diatomic molecules have been undertaken as well [138–141]. An slightly different interferometer setup for large molecules, based on the Talbot-Lau effect in the time domain, was presented in 2013 [3]. It utilizes photoionization gratings and later also photofragmentation gratings [142]. Further developments of this interferometer have allowed to study gravitational free fall [143] and demonstrate interference of a polypeptide [144].

3. Optical properties of molecules

As already briefly mentioned in section 1.1, the different effects occurring at optical gratings are closely connected to the properties of the molecules, which are diffracted at such gratings. It is therefore instructive to take a closer look at physical nature of the most relevant of these molecular properties. We will start by giving an overview of the electric dipole polarizability in section 3.1. The absorption of photons, which is determined by the optical absorption cross-section of the molecules, can lead to a variety of effects as discussed in section 1.1. We will take a deeper look into this in section 3.2.

3.1. Dipole polarizability

3.1.1. Introduction

The polarizability $\boldsymbol{\alpha}$ describes the linear response of the electric dipole moment $\mathbf{d}$ of a particle to an external electric field $\mathbf{E}$. In general we can expand the dipole moment of such a particle as follows:

$$\mathbf{d} = \mathbf{d}_0 + \boldsymbol{\alpha} \cdot \mathbf{E} + \frac{1}{2}\boldsymbol{\beta} : \mathbf{E}^2 + \frac{1}{6}\boldsymbol{\gamma} \,\vdots\, \mathbf{E}^3 + \dots \tag{3.1}$$

$\mathbf{d}_0$ is the electric dipole moment of the particle without the electric field. The contribution to the induced dipole moment which is discussed in this section is given by the second term. In general the polarizability $\boldsymbol{\alpha}$ is a rank 2 tensor, which can be conveniently expressed as a 3×3 matrix in Cartesian coordinates with components α_{ij}. Additionally there are also higher order terms, containing the hyperpolarizabilities $\boldsymbol{\beta}$, $\boldsymbol{\gamma}$, …, which are tensors of higher ranks. In principle there are also contributions involving $\nabla\mathbf{E}$. If the electric field is relatively weak, in particular for static electric fields, one can generally neglect the contributions from hyperpolarizabilities. They are however relevant in intense laser fields and play an important role in non-linear optics [145–147]. One application of these non-linear effects is briefly discussed in section 4.4.1 of this work. In this section we restrict our discussion to the polarizability and thus write the induced dipole moment as

$$\mathbf{d}_{\mathsf{ind}} = \boldsymbol{\alpha} \cdot \mathbf{E} \tag{3.2}$$

The SI unit of polarizability is $\mathrm{C\,m^2\,V^{-1}}$. Experimental values however are often preferably given as polarizability volumes $\tilde{\boldsymbol{\alpha}}$ by factoring out $4\pi\varepsilon_0$, which is set to be numerically equal to one in atomic units. The volume is usually given in $\mathrm{\AA}^3$ or in units of the Bohr radius cubed a_0^3 when using atomic units [148, 149]. In this work we will use SI units but write numerical values explicitly as $4\pi\varepsilon_0 \cdot \tilde{\boldsymbol{\alpha}}$ to facilitate comparison with literature values for polarizability volumes. Note that [145] uses polarizability volumes, giving rise to additional factors of $4\pi\varepsilon_0$ in the expressions given there.

The polarizability tensor can be decomposed into a symmetric and an antisymmetric part. It turns out the antisymmetric part vanishes for static electric fields. Here we are however interested in the *dynamic* polarizability $\boldsymbol{\alpha}(\omega)$. The latter describes the linear response (3.2) in non-static electric field, i.e. in a light field with frequency ω. This frequency dependent quantity can have an antisymmetric part and is in general also complex [145]. The imaginary component of $\boldsymbol{\alpha}$, which usually goes to zero in the static limit $\omega \to 0$, is identified as the absorptive part of the polarizability tensor. As the name suggests this part describes absorption processes, e.g. followed by relaxation via spontaneous emission or collisions. It is in fact directly proportional to the total photon absorption cross section. This follows from the optical theorem. In case the polarizability for a given frequency can be sufficiently described by a single scalar $\alpha(\omega)$, i.e. in the isotropic case, the absorption cross section is given by [145, 150]

$$\sigma(\omega) = \frac{\omega}{\varepsilon_0 c} \mathrm{Im}\left\{\alpha(\omega)\right\} \tag{3.3}$$

The real part of the polarizability is called the dispersive part. It can be understood to describe absorption of a photon followed by immediate stimulated emission. [145]. As we will discuss further in section 5.5, the dispersive part will be responsible for the phase grating effect of the standing light wave. In general the polarizability of individual particles is connected to optical properties of the bulk material. The susceptibility is proportional to the mean polarizability per unit volume. It follow that the dielectric constant and the refractive index of a material are also related to the polarizability. E.g. for a dilute gas of atoms the refractive index can be written as [145, 148, 151]

$$n \simeq 1 + \frac{N\bar{\alpha}}{2\varepsilon_0} \tag{3.4}$$

N is the number density of the gas and $\bar{\alpha}$ is the mean polarizability.

3.1.2. Quantum mechanical expressions

So far the discussion of the polarizability has been entirely classical. Since atoms and molecules are however quantum mechanical systems, it is necessary to employ a quantum formalism to describe and compute their polarizabilities. The generalization of (3.2) to the quantum picture is straightforward. We write the first order corrections to the diagonal elements of the dipole moment operators $\hat{\mathbf{d}}$ as

$$\hat{\mathbf{d}}_{kk}^{(1)}(t) = \frac{1}{2}\left(\hat{\mathbf{d}}_{kk}(\omega)e^{-i\omega t} + c.c.\right) \tag{3.5}$$

This is is appropriate since the perturbations of the dipole operators are expected to oscillate with the same frequency ω as the perturbing electric field. The dipole moment operators in (3.5) are related to the amplitude $\mathbf{E}_0$ of the external field via [145, 152]

$$\hat{\mathbf{d}}_{kk}(\omega) = \hat{\boldsymbol{\alpha}}_{kk}(\omega) \cdot \mathbf{E}_0 \tag{3.6}$$

in analogy to (3.2). The indices kk refer to the matrix elements of the quantum mechanical operators in (3.5) and (3.6). I.e. k denotes a particular state of the particle. $\hat{\boldsymbol{\alpha}}_{kk}$ is the expectation value of the polarizability operator for a system in this particular state. It also has two implicit Cartesian components because of the tensorial nature of $\boldsymbol{\alpha}$. These matrix elements are also called transition polarizabilities. Often one refers to the ground state when evaluating (3.6). More generally, the classical relationship (3.2) is recovered when referring to expectation values of both the dipole moment and the polarizability operator [153].

In principle the transition polarizabilities $\hat{\boldsymbol{\alpha}}_{kk}(\omega)$ can be computed using perturbation theory. The Cartesian components ij of the transition polarizability are then given by [145, 153]

$$\left(\hat{\alpha}_{ij}\right)_{kk}(\omega) = \sum_{l \neq k} \left\{ \frac{\left(\hat{d}_i\right)_{kl} \left(\hat{d}_j\right)_{lk}}{\hbar\left(\omega_{lk} - \omega - i\frac{\Gamma_l}{2}\right)} + \frac{\left(\hat{d}_j\right)_{kl} \left(\hat{d}_i\right)_{lk}}{\hbar\left(\omega_{lk} + \omega + i\frac{\Gamma_l}{2}\right)} \right\} \tag{3.7}$$

The sum runs over all other states k and becomes an integral for continuous states. $\left(\hat{d}_i\right)_{kl}$ denote the i-th Cartesian component of transition matrix element, ω_{lk} are the transition frequencies between the states l and k and Γ_l is the linewidth of the state l. The notion of the transition polarizabilities as defined above can be generalized further by also introducing off diagonal elements kl. These objects are then related to the scattering tensor [145, 152]. Off resonance, if the linewidth Γ_l is negligible compared to the other terms, (3.7) can be approximated as the real expression [145, 151]

$$\left(\hat{\alpha}_{ij}\right)_{kk}(\omega) = \sum_{l \neq k} \frac{2\omega_{lk} \left(\hat{d}_i\right)_{kl} \left(\hat{d}_j\right)_{lk}}{\hbar\left(\omega_{lk}^2 - \omega^2\right)} \tag{3.8}$$

The discussion from section 3.1.1 regarding the real and imaginary parts still holds for the polarizability operator. It can be decomposed into a Hermitian and an anti-Hermitian part:

$$\hat{\boldsymbol{\alpha}}(\omega) = \hat{\boldsymbol{\alpha}}'(\omega) + i\hat{\boldsymbol{\alpha}}''(\omega) \tag{3.9}$$

The Hermitian part $\hat{\boldsymbol{\alpha}}'$ accounts for the dispersive interaction with the light field, giving rise to an energy shift (see section 3.1.3). The anti-Hermitian component $\hat{\boldsymbol{\alpha}}''$ is associated with the effects of absorption [145].

In general the polarizability operator can also be decomposed into a scalar, vector and tensor component, coresponding to the irreducible components of the spherical-tensor basis. The isotropic scalar polarizability for a particle in state k is represented by a single scalar $\bar{\alpha}$, which can be conveniently expressed using the oscillator strengths f_{lk} of the system:

$$\bar{\alpha}(\omega) = \frac{e^2}{m_e} \sum_l \frac{f_{lk}}{\omega_{lk}^2 - \omega^2 + i\Gamma_l\omega} \tag{3.10}$$

For simplicity we do not explicitly denote the quantum state k. Oscillator strengths are given by

$$f_{lk} = \frac{2m_e\omega_{lk}}{3\hbar g_J e^2} \langle k||\hat{d}||le\rangle \tag{3.11}$$

The last factor in this expression is the reduced matrix element as defined in the Wigner-Eckart theorem [154]. m_e is the electron mass, e is the elementary charge and $g_J = 2J + 1$ is the degeneracy of the ground state with rotational quantum number J. Relation (3.10) can be used to compute polarizabilities if the oscillator strengths have been measured via other experimental methods. Even if only some of them are known, one can use (3.10) to give an estimate on the scalar polarizability by making use of sum rules for the oscillator strengths. This is particularly useful for alkali atoms where only one electron is responsible for most of the polarizability [145–148, 150].

3.1.3. Dipole potential

The interaction of a polarizable particle with an external light field is of interest to us as it defines the phase grating mechanism in our experiment described in section 5.5. Quantum mechanically the Hamiltonian of the system is modified by the term

$$\delta\hat{H} = -\frac{|E_0|^2}{4} \cdot \mathbf{e}^* \cdot \hat{\boldsymbol{\alpha}} \cdot \mathbf{e} \tag{3.12}$$

Here E_0 is the amplitude of the oscillating light field and $\mathbf{e}$ is its polarization vector. As already mentioned, the Hermitian part of the operator results in an energy shift while the anti-Hermitian part describes absorption. At this point we restrict our discussion to the influence of the dispersive (Hermitian) part of the polarizability. To find the energy shift in a particular state one has to take the expectation value of (3.12). For a pure state $|k\rangle$ this yields

$$\delta E = \langle \delta\hat{H} \rangle = -\frac{|E_0|^2}{4} \cdot \mathbf{e}^* \cdot \hat{\boldsymbol{\alpha}}_{kk} \cdot \mathbf{e} \tag{3.13}$$

Note that by definition $\langle k|\hat{\boldsymbol{\alpha}}|k\rangle = \hat{\boldsymbol{\alpha}}_{kk}$. It is also possible to compute this energy shift of the particle as the second order correction in perturbation theory. This is also an alternative way of defining the polarizability tensor [145, 147, 148, 153].

We can view the energy shift (3.13) caused by the external light field as a potential U seen by the polarizable particle. As we will see in the next section, often only the isotropic component of the polarizability is important. In this case we can express this potential in terms of the intensity I of the light field as

$$U = -\bar{\alpha} \cdot \frac{|E_0|^2}{4} = -\bar{\alpha} \cdot \frac{I}{2c\varepsilon_0} \tag{3.14}$$

For a static electric field $\mathbf{E}$ this potential energy is

$$U = -\bar{\alpha} \cdot \frac{|\mathbf{E}|^2}{2} \tag{3.15}$$

If we replace the absolute value of the static field with the average for an oscillating field we recover (3.14).

3.1.4. Polarizabilities of molecules

For evaluating the components of the transition matrix elements $(\hat{p}_i)_{kl}$ in (3.7) one has to choose a particular coordinate system. For molecules it is convenient to choose a coordinate frame fixed with respect to some molecular axis. However, to describe interactions with external fields it is more natural to choose a space fixed coordinates system with respect to the light field. In general it is easy to perform a rotation in order to transform from one frame to another. Experimentally one however usually deals with ensembles of randomly orientated, rotating molecules. In this case the only accessible quantities are the rotational invariants. In particular this is the isotropic scalar polarizability in the space fixed frame [145–147, 155]:

$$\bar{\alpha} = \frac{1}{3} \operatorname{Tr} \boldsymbol{\alpha} \tag{3.16}$$

For randomly orientated molecules as are present in the experiment, this is the relevant quantity in the potential (3.14). In principle the polarizability anisotropy

$$(\Delta\alpha)^2 = \frac{1}{2}\left(3\,\mathrm{Tr}\,\boldsymbol{\alpha}^2 - (\mathrm{Tr}\,\boldsymbol{\alpha})^2\right) \tag{3.17}$$

is also a rotational invariant [145, 146]. It is however not directly relevant for the measurement results in this work. We will therefore restrict our discussion to the average isotropic polarizability $\bar{\alpha}$ from now on.

For molecules the average polarizability has contributions from both the electrons as well as the vibrational and rotational motion of the molecule. The computation of the average polarizability for diatomic molecules in particular is described extensively in [155] and also summarized in [145, 153]. We briefly reproduce the key ideas here.

In the *clamped-nucleus* method one first assumes the molecular axes, i.e. the position of the nuclei as fixed. The polarizability caused by the electrons of the molecule is first separately computed using e.g. (3.7). A variety of techniques [155] can be used to account for the vibrational motions. A value for the isotropic polarizability can then be found by taking a classical thermal average of the electronic and vibrational contributions to the polarizability tensor.

The *sum-over-states* technique represents a more rigorous quantum mechanical treatment. The molecular wave function is written as a combination of electronic, vibrational and rotational components in the Born-Oppenheimer approximation. For this quantum state describing the entire molecule one computes the polarizability using (3.7) directly in a space fixed frame. One usually considers the energy shift which depends on the diagonal components of the polarizability tensor for linear polarized light. The transition matrix elements can be written using their respective expressions in the molecular fixed frame using the usual rotation transformations. The energy shift derived this way can be divided into contributions corresponding to electronic, vibrational and rotational polarizabilities. These expressions account for interaction between different electronic, vibrational and rotational levels respectively. In most cases the coupling of the electronic component to different rovibrational states can be neglected. Thermal averages of these values are computed by averaging over a Maxwell-Boltzmann distribution of the corresponding quantum numbers (J, M, ν). The electronic, vibrational and rotational contributions to the polarizability are significant if the frequency of the driving electric field is close to the respective energy spacing. For optical frequencies this means that usually only the electronic component is relevant [153, 155].

Polarizabilities of larger molecules can also be computed with the sum-over states method or other perturbative methods. The necessary electronic wavefunctions can be determined using e.g. the Hatree-Fock method. Rotations can be accounted for similarly to the diatomic case by considering the molecule as a rigid rotor. Density-functional theory (DFT) is also used to determine polarizabilities [145, 147, 156]. There are also a number of semi-empirical methods for computing polarizabilities of molecules, most importantly the so called additivity methods. Here we briefly give an overview of some of them.

In the induced dipole model one associates a polarizability $\boldsymbol{\alpha}_i$ with each atomic site i. The induced dipole moment at each site is then proportional to the *local* electric field E_i, which is the sum of the externally applied field and the fields of the induced dipoles at all other sites.

$$\boldsymbol{d}_i = \boldsymbol{\alpha}_i \cdot \mathbf{E}_i = \boldsymbol{\alpha}_i \cdot \left[\mathbf{E}_{i,0} - \sum_{j\neq i} \boldsymbol{T}_{ij}\mathbf{d}_j\right] \tag{3.18}$$

The tensor $\mathbf{T}_{ij}$ describes the electric field at site i induced by the dipole at site j and $\mathbf{E}_{0,i}$ is the external electric field at site i. (3.18) can then be used to derive an expression for the local dipole moments and consequently also the total induced dipole moment in terms of the external electirc field. From this one can compute the polarizability tensor and the average polarizability using (3.16) as usual [157–161].

Another additive approach is to associate empirically determined effective polarizabilities with each atom depending on its environment. Estimates for the total average polarizabilities are given by the sum of all atomic contributions. Methods of this type differ depending on how the effective polarizabilities are assigned. For example effective polarizabilities might be given for specific bonds or chemical subgroups within the molecules. In the atomic hybrid polarizability method the effective polarizabilities depend on the state of hybridization of the atom but not the atoms it is bonded to. A related method is the atomic hybrid component method. In any case it is not sufficient to simply add up the contributions of the isolated atoms [145, 159, 162–164].

At the end of this section it should be noted that the discussions covered above usually assume linearly polarized light. In this case only the diagonal components of the polarizability are relevant for the energy shift (3.13) (for an appropriate choice of basis). In particular this means that the vector component of the polarizability can be disregarded. Averaging over random orientations of the diagonal elements leads to the isotropic polarizability (3.16). However, by experimental necessity our experiment uses circularly polarized light for the standing light wave (see section 4.4). For circular polarization the expression in (3.13) in general also involves off-diagonal elements of the polarizability tensor. It turns out however that for the molecules investigated here (see section 4.7) these off-diagonal elements vanish because of the molecular symmetries, if the molecules are viewed as rigid. This is usually not the case, but we may still assume the discussion only involving the diagonal elements to be approximately valid [145, 151].

3.1.5. Measuring polarizabilities

Most conventional methods for determining polarizabilities rely on measuring bulk properties, which depend on the polarizabilities of the individual particles. Naturally this only gives information about average isotropic polarizabilities as particles will in general be randomly oriented and in a thermal distribution of states. One of these bulk properties is the dielectric constant ε, which is related to the polarizability via the Debye equation (Clausius-Mossotti relation if there are no orientating effects). The dielectric constant can be determined by inserting the material between the plates of capacitor, changing the capacitance. This gives accurate results for low frequencies. Similarly one can use the relationship between the average polarizability $\bar{\alpha}$ and the refractive index n of a material to determine $\bar{\alpha}$. As already mentioned for dilute gases equation (3.4) holds, which is a special case of the more general Lorentz-Lorenz relation, which holds for high frequencies, where orientating effects are negligible. Accurate determination of n is possible via interferometric methods [165, 166]. For biomolecules in particular these methods are often challenging because it either requires the molecules to be in solution or to be brought into gas form. Within solvents the properties of the molecules are modified by intermolecular interactions. Depending on the chemical stability of the molecules creating a vapor with a well known and high enough density is also often challenging [145–147, 167].

Other techniques for measuring polarizabilities rely on Rayleigh scattering [168, 169] or, for static polarizabilities, the deflection of atomic / molecular beams [145–147, 167]. More closely related to the technique described in this thesis are methods based on atom interferometry. In a Mach-Zehnder interferometer one applies different electric fields to each one of the interferometer arms. The dipole potential (3.15) then introduce a phase shift proportional to the mean polarizability and the square of the applied voltage. If the geometry of the interaction region is known this allows to deduce $\bar{\alpha}$ of the atoms [93, 145, 146, 170]. For larger molecules static polarizabilities have also been determined using deflection in near field interferometers of TLI and KDTLI type [126, 132, 133, 171]. Optical polarizabilities have been measured in the KDTLI setup as well. Like the experiment described here is based on the light grating acting as a phase grating [128, 129, 133].

3.2. Absorption of photons

3.2.1. Introduction

The probability for a particle to absorb a photon can be quantified by the optical absorption cross-section $\sigma(\omega)$. It is the effective area a single photon must "hit" to be absorbed. I.e. the number of absorbed photons per unit time $\dot{n}$ is equal to the photon flux times the absorption cross-section [172]. For a given laser intensity I this is then given by

$$\dot{n} = \frac{\sigma(\omega) I}{\hbar\omega} \tag{3.19}$$

As outlined in the previous sections absorption is described by the imaginary part of the complex polarizability. The two are related via (3.3). Naturally the absorption cross-section is also frequency dependent. Having already given an overview of the basics of the quantum mechanical description for the polarizability in section 3.1.2 we want to focus on a more qualitative description in this section to give some insight into the processes following absorption.

The physical details of the most important processes that a molecule might undergo can be better understood with the help of a Jablonski diagram [173], which illustrates the energy levels of a molecule in a simplified way. An example of such a diagram is shown in figure 3.1. For simplicity we only consider three electronic states in the diagram: the singlet ground state S_0, the first excited singlet state S_1 and the lowest triplet state T_1. For each of the electronic states a set of vibrational states exist for the nuclei forming the molecule. Note that the triplet state T_1 is of slightly lower energy than the corresponding singlet state S_1. The molecule can absorb a photon matching the energy difference between the ground state and a vibrational level of the S_1 state (k_{abs}) [174, 175]. The relative strengths (i.e. extinction coefficients) of transitions to different vibrational levels are given by the transition dipole moments and consequently by the oscillator strengths (3.11). This defines the fundamental shape of the absorption spectrum, although e.g. solvent effects can in general further influence it. Usually the vibrational equilibrium positions of the nuclei are different in the electronic ground state S_0 and the excited state S_1. As a consequence of the Franck-Condon principle transitions to higher vibrational levels are therefore in general favored, i.e. the absorption maximum corresponds to a transition to a vibrationally excited state [175–177]. Once the molecule has been excited into a higher vibrational state of the electronic configuration S_1 it usually quickly relaxes to the vibrational ground state of S_1 predominantly non-radiatively. Usually this occurs on the time scale of picoseconds [174, 178]. During this process, which is termed intramolecular vibrational randomization (IVR), the excess energy is redistributed among the internal degrees of freedom of the molecule [179–181].

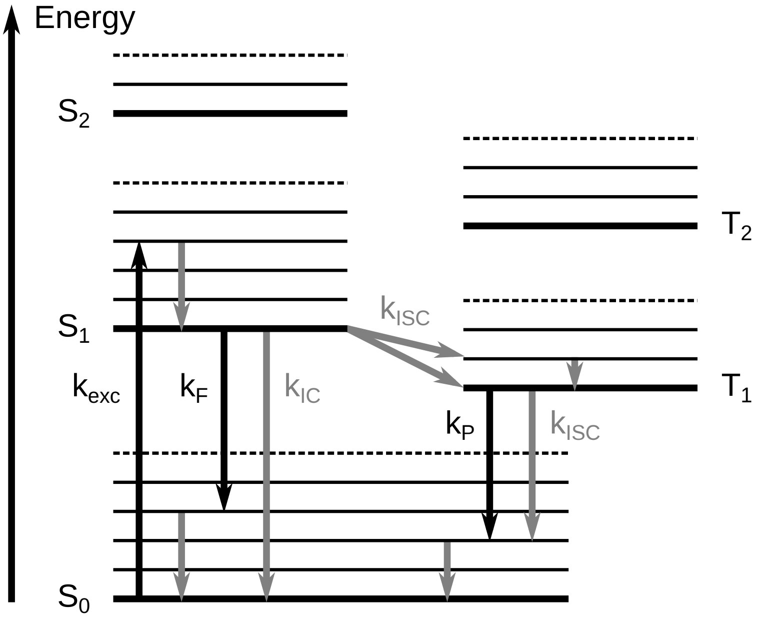

Figure 3.1: Jablonski diagram illustrating the most important photophysical processes. Adapted from [178] and [175]. Nonradiative processes are marked in grey, radiative ones in black. They are labelled as follows: k_{exc} singlet-singlet absorption, k_{F} fluorescence, k_{IC} internal conversion, k_{ISC} intersystem crossing, k_{P} phosphorescence.

After excitation of the molecule there are different relaxation pathways to the ground, as illustrated in figure 3.1. The molecule can undergo a direct radiative transition via the emission of a photon, i.e. fluorescence (k_{F}). This is briefly discussed below. There is also the possibility of reaching the ground state directly via non-radiative decay (internal conversion, k_{IC}). Another non-radiative process is intersystem crossing (k_{ISC}). This allows the molecule to transition from the singlet state S_1 to the triplet state T_1 via spin-flip. From there the molecule can again decay to the electronic ground state S_0 by emission of a photon (k_{P}). The process of light emission via a $T_1 \rightarrow S_0$ transition is called phosphorescence. The term fluorescence meanwhile is reserved for $S_1 \rightarrow S_0$ transitions. The main physical difference between these two processes is that fluorescence occurs much faster than phosphorescence [172, 174]. The lifetimes for fluorescence are commonly on the scale of nanoseconds, with the longest known lifetimes at the order of microseconds. The lifetime of the triplet states associated with phosphorescence are on the scale of microseconds up to multiple seconds for the longest lived ones [174, 175]. The reason for the longer lifetimes of the triplet state is that radiative transitions from T_1 to the electronic ground state S_0 are spin-forbidden. This is also the reason why direct excitation from S_0 to T_1 via absorption can usually be neglected compared to $S_0 \rightarrow S_n$ transitions [172, 175, 177].

The characteristic feature of a molecules exhibiting fluorescence is the absorption of light at some wavelength λ_{abs} and subsequent emission at some longer, i.e. less energetic wavelength $\lambda_{\text{em}} > \lambda_{\text{abs}}$ (Stokes shift). In reality both the absorption and emission spectrum will be relatively broad due to the number of possible transitions between the initial and possible excited states of the molecule. Interactions with e.g. a solvent can further broaden the spectra [172, 174, 176, 178]. After relaxing to the excited singlet state S_1 the molecule in the vibrational ground level of S_1 can eventually reach the ground state S_0 again by emitting a fluorescence photon. Because of the energy dissipated during the transition from the originally higher vibrational level of S_1 to the lowest one, the energy gap between S_0 and the excited state is now narrower than during the absorption process. This is the origin of the Stokes shift. In analogy to the absorption process the transition to the lower electronic state may in fact reach higher vibrational levels of S_0 before again dissipating the excess vibrational energy via non-radiative pathways. Because the vibrational structures are usually similar for S_0 and S_1 the absorption and fluorescence spectra are often (approximately) mirror images of each other [172, 174, 175, 177].

The discussion so far has not considered potential changes in the chemical structure of the molecule. A more refined picture than the Jablonski diagram in figure 3.1 is the one of potential energy surfaces parametrized by reaction coordinates (e.g. the positions of the nuclei). Stable configuration of the molecule are identified with minima in these potential energy surfaces. In adiabatic photoreactions energy barriers between local minima of the molecular configuration are mirrored in the excited state potential energy surfaces. However, the barriers are usually lowered such that thermal energy might overcome them, allowing the molecule to reach a different configuration than it was in initially. In the case of diabatic photoreactions the excited state energy surface comes very close to or crosses the ground state energy surface at an intermediate configuration between two stable configurations in the ground state S_0. After a transition to the excited state via absorption the molecule has a high probability of transitioning to the lower state at this point where the surfaces are close. From there it can also transition to a different minima of the ground state energy surface than the initial one. In a similar type of process the excited state energy surface has a minimum at some intermediate configuration. The excited molecule first relaxes to this intermediate before transitioning to the ground state. From the intermediate configuration in the ground state it can reach a stable minimum different from the initial one [10, 175]. We will discuss two processes that change the chemical structure upon photon absorption in more detail in sections 3.2.2 and 3.2.3.

3.2.2. Photocleavage

Photodissociation or photofragmentation is generally characterized by the absorption of a photon causing the cleavage (breakage) of a chemical bond. Such cleavage reactions of (sigma) bonds can usually be categorized as one of two types: homolytic cleavage and heterolytic cleavage. In the former case the resulting fragments are a pair of radicals. The latter case referes to the production of an ion pair. After photocleavage the products usually undergo additional chemical reactions depending in the particular bonds which were broken. The process by which absorption leads to the actual photodissociation can also vary. For diatomic molecules optical dissociation is a common pathway. In this case the energy delivered by the photon is enough to directly allow for the constituent atoms to separate. For larger molecules the process of predissociation is more relevant. Here the energy of the electronically excited state the molecule is in after absorption is not above its dissociation threshold. However, the molecule can undergo radiationless transitions to another electronically excited state, which has a lower dissociation limit. Such transitions are favored when the potential energy surfaces of the two excited states cross. In complex molecules there usually exist a number of different pathways to dissociation. Redistribution of internal energy also allows the bond cleavage to happen at another part of the molecule from where the absorbed energy was initially localized [175, 182].

A special case of photodissociation involves the cleavage of a specific functional group. Such functional groups are of great interest as photoremovable protecting groups (PPGs) in chemical and biological applications. They allow a molecule or a functional group of a molecule to be activated on demand via irradiation with light of a particular wavelength. A molecule or drug can therefore be delivered in a "caged" form and made active with precise high spatial and temporal control. One advantage of using light is that is non-invasive and does not cause any contamination in contrast to chemical ways of control. Wavelength selective PPGs allow for the controlled release of one molecule or functional group out of multiple. This expands the possibilities for controlling chemical and bimolecular processes [11, 183, 184]. Photocleavable tags also have applications as a tool for controlling the charge state of peptides and proteins in the gas phase [185, 186].

One of the challenges for biological applications is designing PPGs that are active at suitable wavelengths. The activation wavelengths for most of the commonly used PPGs are in the UV. However, the transparency of biological tissue to UV light is usually low and UV light may also be harmful to it. Motivated by this and other factors a large number of PPGs suitable for different applications have been studied [11, 184, 187]. In this work we make use of the effectiveness of UV light for photocleavage by employing a light grating at $266\,\mathrm{nm}$. The molecules used for this purpose (see section 4.7.4) are specifically tailored to cleave at this wavelength. The photocleavable groups in this compound are formed by nitrobenzyl groups. Nitrobenzyl and its derivatives are one of the most widely used PPGs and also one of the first which were studied. The primary photoprocess is understood to be excited-state hydrogen transfer to the nitro group [11, 187–189].

3.2.3. Photoisomerization

As the name suggests photoisomerization involves a molecule changing from one structural isomer to another, i.e. undergoing some structural rearrangements. The most important types of photoisomerization reactions we want to mention here are cis-trans isomerization and ring opening / closing reactions. The prototypical system for cis-trans isomerization are ethylene derivatives. The isomerization corresponds to a $180°$ rotation around the molecules double bond. In this process an electron is excited from a bonding to an antibonding orbital. In this electronic state the configuration where the molecule is rotated by $90°$ around the former double bond is favored. After the molecule relaxes back to the ground state it can reach a different isomer compared to the one as which it started. Ring opening and closing is usually characterized by the formation or cleavage of a sigma bond between the termini of a linear system of pi electrons (electrocyclic reactions). If two new sigma bonds are formed to form rings one speaks of intramolecular cycloadditions. In both cases the particular mechanisms vary depending on the molecular system under consideration [175, 182].

An appealing property that often goes hand in hand with photosiomerization is photochromism. Photochromic compounds exhibit a reversible change in their absorption spectra, i.e. their color, induced by irradiation with light. This can often be attributed to different electronic structures of the two isomers. Photochromic molecules that are fluorescent usually also change their fluorescence spectra in this case. It might, for example, be the case that one isomer is strongly fluorescent while the other is non-fluorescent. There is a large number of different mechanism for photochromism, in general not limited to photoisomerization. Many well studied photochromic molecules, such as stilbenes [190] and azobenzenes [191], do rely on the aforementioned process of cis-trans isomerization. Reversible opening and closing of rings also enables photochromism in some molecules [192–194]. A rich class of molecules belonging to the latter category are diarylethenes. Molecules of this type show excellent stability once switched. Also among the many compounds studied so far there are several which show a distinct "on/off" switching of fluorescence. Because of this diarylethenes have also been studied with the prospect of optical memory [195–197].

3.2.4. Gas-phase spectroscopy

The study of biomolecules in the gas-phase is mainly motivated by the fact that it gives access to the properties of the molecules in an isolated state. On the one hand this allows for a better comparison with theory as the latter usually also only describes isolated systems. On the other hand gas-phase measurement act as a complement to other measurement techniques. Comparison of different phases gives insight into which properties are intrinsic to the molecules and which are induced by the interaction with the environment. This makes it interesting to study molecules in the gas-phase even though this differs significantly from the usual state they are in when acting in biological systems [198, 199]. Spectra measured in solution can show notable differences to the gas-phase spectra for both absorption and fluorescence emission. Solvents can reduce molecular energy levels thus changing transition frequencies. Perturbations caused by the solvent can also enhance other transitions which might otherwise not be relevant. These effect are naturally dependent on both the molecules in question and the properties of the solvent. Usually the effects are larger for polar solvents. Solvents also bring broadening of the spectral lines, which usually requires gas-phase measurements to be avoided [172, 182].

In principle gas-phase spectra can be measured analogous to spectra in solution by comparing the intensity before and after the sample and evaluating the result following Lambert-Beer's law. This technique of direct spectroscopy is in most cases not suitable for biomolecules as usually only very dilute gases of these molecules can be created. Thus very long path lengths would be needed to see a significant effect this way. Instead one usually employs techniques collectively termed action spectroscopy. In this case the fraction of the molecules which absorbed a photon is compared. Two such methods which are used for UV spectroscopy in molecular beams are resonance-enhanced multiphoton ionization (REMPI) and laser-induced fluorescence (LIF) [199, 200]. These and other methods have been refined to allow for recording spectra with high precision. However, it is usually not possible to extract accurate values for the absolute absorption cross-sections. Lack of exact knowledge of the molecular density or fluctuations in the source prevent a precise determination of the absorption cross-section. Matter-wave interferometers are an interesting alternative for such measurements because the can in principle operate on a per molecule basis. Absorption cross-section can in principle be deduced directly from photon-recoils as proposed for near-field setups [201, 202]. While the scheme presented here also indirectly relies on this recoil it differs in that it is directly measuring the absorption in the grating responsible for the refraction. As a far-field setup it is also less complex than near-field configurations.

4. The Far-field setup

Having reviewed both the historical developments of matter-wave interferometry and the basics of molecular physics necessary to understand the experiment described here, we now want to turn to a detailed description of the setup with which the experiment was carried out. The experimental apparatus used for the measurements presented in this work builds on the ideas developed and used in a number of previous experiments throughout the last two decades [1, 2, 8, 119, 120, 122]. We will begin this section by giving an overview of the experiment and its components. In the following sections the various parts and their functionality will be discussed in more detail.

4.1. Overview of the experiment

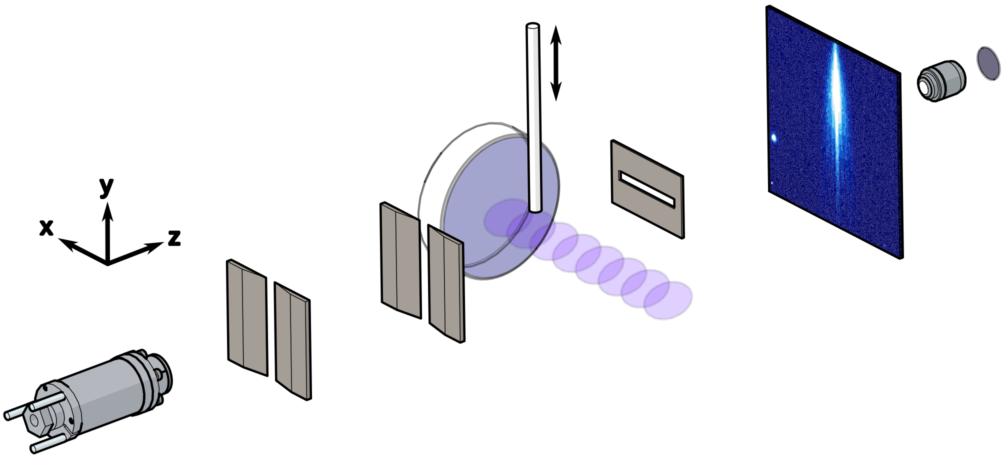

Figure 4.1: Sketch of the experiment showing the source, collimation slits and light grating. The fiber profiler described in section 4.4.2 is also illustrated.

The concept behind far-field diffraction of molecules is very similar to the textbook example of light being diffracted at a periodic grating. The molecules are emitted from some source, which has to provide the necessary coherence to later resolve the diffraction effects. They then impinge on a periodic structure, the grating. At a distance from this grating a spatially resolving detector is located. As in the case of light, this yields a diffraction pattern consisting of intensity maxima and minima. The separation of these peaks is directly proportional to the ratio of the de Broglie wavelength λ_{dB} to the period d of the grating [203, 204]. While near-field interferometers have a more favourable scaling of the grating period with the mass of the object [123, 205], the far-field configuration allows for a more direct observation of the interference effect by direct imaging and only requires one grating, which makes the setup more easy to implement. In this setup the grating structure is a standing light wave, which interacts with the molecule via the Kapitza-Dirac (phase grating) effect [36] and via absorption. We will discuss the details of these effects in section 5.5.

Figure 4.2 shows a sketch of the setup used here. The experiment is contained in a high vacuum (HV) chamber, which is divided into three subsections. The sections are connected along the axis of the molecular beam and are separated by skimmers. The first chamber contains the source for the molecular beam. The pressure in the *source chamber* is usually on the order of $1 \cdot 10^{-6}\,\mathrm{mbar}$. The source used in this experiment is discussed in more detail in section 4.2. The *main chamber*, which is usually at a pressure of $2 \cdot 10^{-7}\,\mathrm{mbar}$, contains a number of collimation slits used to prepare the transversal and longitudinal coherence. The details of the collimation are described in section 4.3. The main chamber also houses the grating itself. For the optical measurements presented in this work a deep UV light grating was used. Section 4.4 contains an overview of the optical setup used to create the grating. After the main chamber the molecular beam reaches the *detection chamber* where the molecules impinge on a quartz window and are detected via fluorescence microscopy, as explained further in section 4.6. The detection chamber is kept at a pressure lower than the main chamber, at the order of $5 \cdot 10^{-8}\,\mathrm{mbar} - 1 \cdot 10^{-7}\,\mathrm{mbar}$.

One of the main experimental challenges with this setup is to ensure proper alignment of all the components. The small physical sizes of the structures make precise positioning necessary, which needs to be verified in an appropriate way. We describe the most important procedures used to achieve this in section 4.5. Based on the constraints invoked by the different components of the experiment we will give a selection of molecules, for which the measurements covered in this work will be demonstrated, in section 4.7.

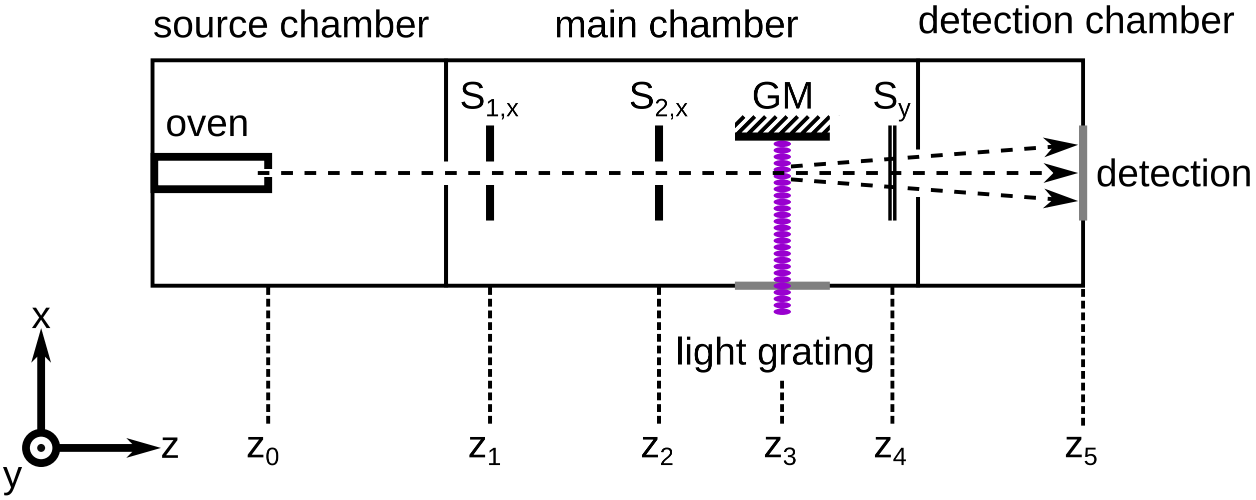

Figure 4.2: Schematic overview of the experimental setup. The sketch shows the view from the top, the coordinate axes are defined as indicated in the bottom left corner with the z axis along the molecular beam and the y axis oriented vertically. $S_{1,x}$ and $S_{2,x}$ are the transversal collimation slits, S_y is the velocity selector and GM denotes the grating mirror. The positions of the components along the z axis are labeled as indicated. The values for the distance between the components are collected in table 1.

$\Delta z_{30} = z_3 - z_0$	$\Delta z_{53} = z_5 - z_3$	$\Delta z_{43} = z_4 - z_3$	$\Delta z_{31} = z_3 - z_1$	$\Delta z_{32} = z_3 - z_2$
$(90.5 \pm 1.0)\,\mathrm{cm}$	$(70.0 \pm 1.0)\,\mathrm{cm}$	$(8.5 \pm 1.0)\,\mathrm{cm}$	$(38 \pm 5)\,\mathrm{cm}$	$(8 \pm 2)\,\mathrm{cm}$

Table 1: Measured distances between the components of the experiment. The exact positions of the collimation slits inside the vacuum chamber were not directly accessible leading to the relatively high uncertainties in some of the distances.

4.2. Knudsen cell

An effusive oven source is used for the measurements at light gratings. The oven follows a basic single-chamber design, figure 4.3 shows a cross-section of the source. The molecular sample (usually in powder form) is filled in a crucible inserted into the oven. A heating wire with a resistance of $R_B = 200\,\Omega$ is coiled around the *body* section of the oven, which contains the crucible. The orifice of the oven is formed by a circular pinhole with a diameter of $D_S = 200\,\mu\mathrm{m}$. To avoid clogging of the pinhole via condensation the *nozzle* section of the oven containing the pinhole is heated separately by a $R_N = 100\,\Omega$ heating wire and kept at a higher temperature than the rest of the oven. The nozzle and body sections are sealed by a silver gasket. Their temperatures are monitored individually by two type-K thermocouples [206].

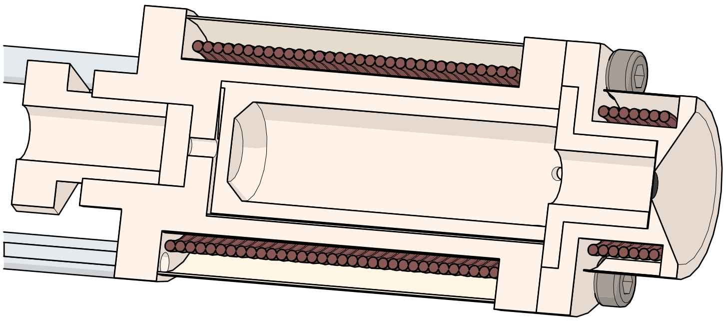

Figure 4.3: Cross-section of the effusive oven source used in the experiment. A second heating wire is used to keep the nozzle at a slightly higher temperature and thus avoid clogging.

Since the aperture of the source is much smaller than the oven chamber itself, it can be assumed that the vapor molecules within the oven is in thermal equilibrium with the chamber walls and that their velocities can be described by a Maxwell-Boltzmann distribution:

$$f(v)\ \mathrm{d}v = \sqrt{\frac{2}{\pi}} \cdot \left(\frac{m}{k_B T}\right)^{\frac{3}{2}} \cdot v^2 \cdot \exp\left(-\frac{mv^2}{2k_B T}\right) \mathrm{d}v \tag{4.1}$$

The rate at which molecules are exiting the nozzle is proportional to their velocity v. Thus the velocity distribution of the flux exiting the source should be proportional to the distribution within the chamber multiplied with v. After normalization this yields the distribution

$$\Phi(v)\ \mathrm{d}v = \frac{1}{2} \cdot \left(\frac{m}{k_B T}\right)^{2} \cdot v^3 \cdot \exp\left(-\frac{mv^2}{2k_B T}\right) \mathrm{d}v \tag{4.2}$$

This description of the velocities is only valid if the aperture is much thinner than its diameter and if the mean free path with in the source is larger than the aperture itself. The thickness of the pinhole used here is approximately $50\,\mu\mathrm{m}$, which should be small enough compared to the $200\,\mu\mathrm{m}$ diameter such that collisions with the walls of the aperture during the passage of molecules can be neglected. However, it turns out that the approximation of a much larger mean free path is not fully valid. Collisions between particles close to the nozzle cannot be fully neglected. The model of free-jet expansion gives a better reproduction of the experimental results in our case. An effective description of the downstream particle flux in this situation is given by introducing a velocity shift w to (4.2) [206–208]:

$$\Phi(v)\ \mathrm{d}v = C \cdot \left(\frac{m}{2k_B T}\right)^{\frac{3}{2}} \cdot v^3 \cdot \exp\left(-\frac{m \cdot (v-w)^2}{2k_B T}\right) \mathrm{d}v \tag{4.3}$$

C is a normalization constant. The angular dependence of the flux for effusive sources follows a cosine law

$$I(\theta)\ \mathrm{d}\Omega = I_0 \cos\theta\ \mathrm{d}\Omega \tag{4.4}$$

$d\Omega$ is the infinitesimal solid angle element into which the flux is emitted and θ is the angle with respect to the direction orthonormal to the aperture. The skimmer between the first and the second vacuum chamber restricts the relevant angles to well below $10\,\mathrm{mrad}$, therefore we will neglect the angle dependence (4.4) in the following discussion [206, 208].

The detector used in this experiment (see section 4.6) records a signal proportional to the number of molecules reaching the detection area within a given time. It therefore effectively measures the flux, which follows the distribution (4.2) for an ideal effusive source and (4.3) for free-jet expansion. In the former case both the mean velocity of the distribution (4.2)

$$\bar{v} = \sqrt{\frac{9\pi k_B T}{8m}} \tag{4.5}$$

and the most probable velocity

$$v_{\mathsf{mp}} = \sqrt{\frac{3k_B T}{m}} \tag{4.6}$$

are approximately $20\ \%$ larger than the corresponding values for the Maxwell-Boltzmann distribution (4.1). As already mentioned however a better description of the experimentally observed velocities is given by (4.2). The mean and most probable velocities (4.5) and (4.6) are thus shifted to even faster velocities depending on w. In this case the analytical forms of these parameters are not quite as simple. In our analysis the parameter w is determined empirically by fitting (4.3) to the velocity distributions extracted from the diffraction measurements. We generatlly see good agreement of this velocity distribution with the experiment and the measured source temperatures as long as there are no there effects changing the distribution of molecules. For more details see section 6.3, figure 6.2 shows an example of such a fit. Typical values for the steady state temperatures of the oven body and nozzle during the measurements are collected in table 2, the characteristic velocities and the de Broglie wavelengths (2.1) are also shown in this table. For the typical velocities we use the mean velocity (4.5) based on the nozzle temperature T_{N}. Despite the additional contribution introduced by the parameter w for the free jet expansion, this still gives a good estimate for the velocities extracted from the fits to the experimental data as described in section 6.3. Of course there is a broader distribution of velocities, which contributes to the signal overall.

molecule	mass m (u)	body temp. T_{B} (°C)	nozzle temp. T_{N} (°C)	$\bar{v}$ ($\mathrm{m\,s^{-1}}$)	λ_{dB} (pm)
H_2-phthalocyanine	514.5	419	473	206	3.8
meso-tetraphenylporphyrin	614.7	372	422	182	3.6
dihydroxy-naphthacenedione	290.3	251	266	234	5.9
photocleavable Zn-phthalocyanine	1182.4	414	442	133	2.5

Table 2: Overview of source temperatures, typical velocities and de Broglie wavelengths. The mean velocities are computed using (4.5) for the nozzle temperatures, which agrees well with the typical velocities observed in the experiment.

4.3. Coherence preparation

In order for interference effects to be observed the superposition of quantum states must be coherent, that is, the phase relation between the states must be well defined. In the Schrödinger wave description of the motional degrees of freedom this can be interpreted analogously to classical wave optics. Coherence is then quantified by the correlation of the wave function at different points in time and in space. The former defines the temporal or longitudinal coherence, the latter is related to the transversal (spatial) coherence [209, 210]. More generally one can associate the coherence of a mixed quantum state with the presence of off-diagonal elements in its density matrix [211]. In this experiment coherence between different rotational and vibrational internal states of the molecules emitted by the source cannot be ensured. However, if the evolution of the spatial degrees of freedom of the state can be regarded as independent of the specific internal state (e.g. approximately the same polarizability for all initial rovibrational states) the coherent superpositions of motional degrees of freedom will be independent as well and yield the same interference pattern for all of them. The internal and motional degrees of freedom can still get coupled if for example a photon is absorbed. Different such entangled states will then not show coherent interference with each other [9, 203]. If we assume that the specific initial state can be viewed as irrelevant for this absorption process as well, we only need to ensure the aforementioned coherence of the spatial degrees of freedom.

4.3.1. Longitudinal coherence

The Wiener-Khinchin theorem relates the temporal coherence to the Fourier transform of the power spectral density. The coherence length, characterizing the maximum path length difference below which interference can be observed, can be estimated from the bandwidth $\Delta\lambda$ as [209, 212]

$$l_c \simeq \frac{\lambda^2}{\Delta\lambda} \tag{4.7}$$

λ denotes the center wavelength. Strictly speaking (4.7) is only valid if $\Delta\lambda$ is small. Since each diffraction peak in an interference experiment at a grating or a double slit corresponds to a path length difference of λ, (4.7) allows us to estimate the highest observable peak order as [212]

$$n_{\mathsf{max}} \approx \frac{l_c}{\lambda} = \frac{\lambda}{\Delta\lambda} \tag{4.8}$$

The de Broglie relation (2.1) relates the wavelength to the velocity of the particle. It follows from the discussion in section 4.2 that our source is not monochromatic as the source emits a relatively wide distribution of different velocities. Intuitively these different velocities would yield interference patterns with different spacings between the maxima. These intensity distributions add up incoherently because of the lack of quantum coherence between the initial states with different velocities, resulting in a "washing out" of the interference maxima [213]. This is illustrated in figures 4.4 and 4.5 for the example of the diffraction at a double slit. Figure 4.4 shows the intensity distributions as functions of the diffraction angle θ for a selection of wavelengths $\lambda = \lambda_0 + \delta\lambda$. It is apparent that the maxima of the different wavelengths agree less and less with each other for higher diffraction orders. In figure 4.5 the sum of the different intensity contribution is plotted. Because the maxima do not match for higher orders anymore, the visibility for orders higher than ~ 10 $(\theta = 0.10)$ is comparatively small. This agrees with the estimation given by (4.8) for a full width of $\Delta\lambda \approx 0.1 \cdot \lambda$.

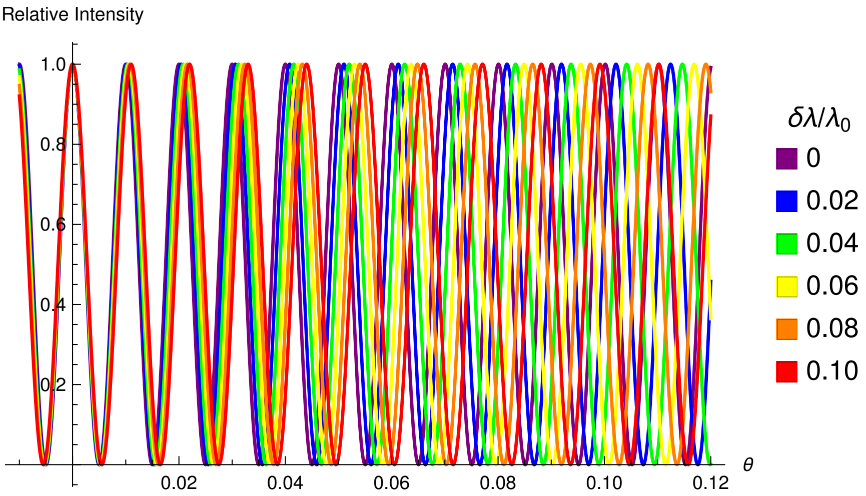

Figure 4.4: Plots of the diffraction patterns calculated for an ordinary double slit with period $a = 100\lambda_0$ and zero slit width [204]. The wavelengths are given by $\lambda = \lambda_0 + \delta\lambda$. The horizontal axis shows the diffraction angle θ, maxima occur at $\theta = \frac{n \cdot \lambda}{a}$. For higher orders the peaks corresponding to the different wavelengths become more and more mismatched.

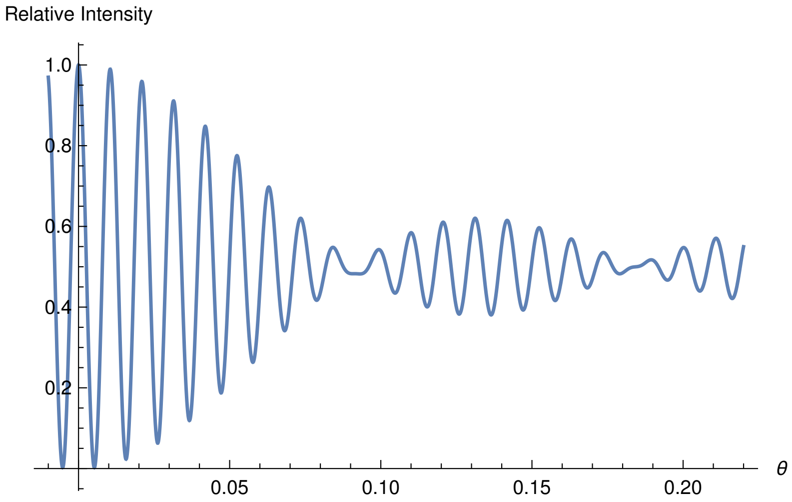

Figure 4.5: The sum of the intensity contributions of different wavelengths plotted in figure 4.4. The visibility is only high for the first few orders and becomes negligible at order $n \sim 10$. This is consistent with (4.8) for $\Delta\lambda/\lambda = 0.1$.

4.3.2. Velocity selection

The previous sections illustrates that it is necessary to either select certain velocities from a relatively narrow range for the diffraction experiment, or to at least separate them from each other. There exists a variety of methods for achieving this for a thermal beam. A common solution is to use rotating slotted disks. If the detection scheme is time resolved, such a disk can be used to imprint a pseudorandom modulation onto the molecular beam. The velocities can then be distinguished by time of flight. For continuously integrating detection scheme multiple disks can be used to only let molecules with certain flight times between them, i.e. velocities, pass [4, 208]. The scheme we use here relies on the free fall of the molecules in earths gravitational field during their transit through the interferometer. This method has already been successfully used in both near [124, 127, 136, 137] and far-field [1, 2, 120, 214, 215] setups. Since only small deviations from forward propagation (along the z axis) make it through the interferometer, the forward velocity v_z is much larger than the other components and thus predominantly determines the de Broglie wavelength. The flight parabola of these molecules can be expressed as

$$y(z) = y_0 + v_{y,0} \cdot \frac{z}{v_z} - \frac{g}{2} \cdot \left(\frac{z}{v_z}\right)^2 \tag{4.9}$$

where g is the gravitational acceleration, z is the coordinate along the flight direction and y_0, $v_{y,0}$ give the initial conditions. By fixing three points along this parabola, e.g. $y(z_0 = 0) = y_0$, $y(z_4) = y_4$ and $y(z_5) = y_5$, it is uniquely defined. Here we chose the notation to be consistent with our coordinates defined in figure 4.2 and we set $z_0 = 0$. One can then find that the parabola fixed by these three points corresponds to the forward velocity

$$v_z = \sqrt{\frac{g}{2} \cdot \frac{z_4 z_5 \cdot (z_5 - z_4)}{z_5 \cdot (y_4 - y_0) - z_4 \cdot (y_5 - y_0)}} \tag{4.10}$$

Experimentally y_0 is defined by the vertical position of the source. y_4 is defined by a horizontal slit (*velocity selector*) labeled as S_y in figure 4.2. Each height y_5 at the detection then corresponds to a different velocity as given by (4.10). Different velocity classes are thus separated vertically in the detection region.

In reality both the source and the velocity selector have a finite size ($\Delta y_0 \equiv D_\mathsf{S}$ and $\Delta y_4 \equiv S_y$ respectively). As a consequence of this not only a single velocity but a certain velocity range arrives at each detection height y_5. The relative width of this velocity distribution, which is equal to the relative bandwidth, can be evaluated as

$$\frac{\Delta v_z}{\overline{v_z}} = \frac{\Delta\lambda}{\lambda} = 2 - 4 \cdot \left(1 + \sqrt{1 + \frac{2v_\mathsf{max}^2}{g} \cdot \frac{\Delta y_4 \cdot z_5 + \Delta y_0 \cdot (z_5 - z_4)}{z_4 z_5 \cdot (z_5 - z_4)}}\right)^{-1} \tag{4.11}$$

Here v_max denotes the maximum velocity in the corresponding velocity range. A derivation of (4.11) can be found in appendix A. Notably the relative velocity spread (4.11) is independent of the absolute positions of the source and the velocity selector slits, instead only depending on their widths.

The velocity selector used in the experiment is a *Thorlabs* S20RD slit with a width of $\Delta y_4 \equiv S_y = (20 \pm 2)\,\mu\mathrm{m}$. By the measurements in table 1 its distance to the source is $\Delta y_{40} = (0.99 \pm 0.02)\,\mathrm{m}$. The slit is mounted on a *Smaract* SLC-1740 piezo stage, which allows for adjustment of its vertical position. With the source size $\Delta y_0 \equiv D_\mathsf{S} = (200 \pm 6)\,\mu\mathrm{m}$ and the total length of the interferometer $\Delta z_{50} = 1.6\,\mathrm{m}$ we can estimate the relative velocity spread from (4.11). Figure 4.6a shows $\frac{\Delta v_z}{v_z}$ as a function of v_max. In figure 4.6b the same quantity is plotted in dependence of the mean velocity calculated as $\overline{v_z} = v_\mathsf{max} - \frac{\Delta v_z}{2}$. As is apparent from this figure the longitudinal coherence becomes worse with larger velocities. Using (4.8) we can estimate that we can distinguish at least the first two diffraction orders for velocities up to mean velocities of $\sim 180\,\mathrm{m\,s^{-1}}$. As we will become apparent when evaluating our results (see section 7) the intensities of higher orders are too weak to accurately measure them in our detection for the experimental parameters used here. However, the interaction with the light grating gives raise to additional peaks between the actual diffraction orders as a consequence of photon absorption in the light grating. Thus more than two intensity peaks on each side of the central maximum are still observable. As discussed more extensively in appendix A we technically only give an upper bound for the bandwidth here. Particularly when $\frac{\Delta v_z}{v_z}$ becomes large, the velocity distribution of the source itself (4.2) becomes relevant as well, which will slightly reduce the velocity spread.

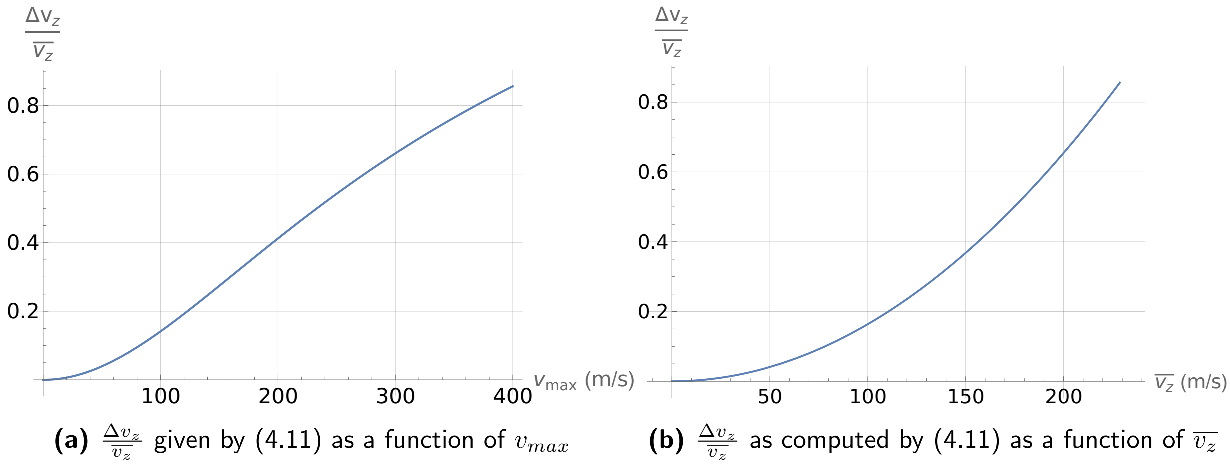

(a) $\frac{\Delta v_z}{\overline{v_z}}$ given by (4.11) as a function of v_{max} **(b)** $\frac{\Delta v_z}{\overline{v_z}}$ as computed by (4.11) as a function of $\overline{v_z}$

Figure 4.6: Relative velocity spread $\frac{\Delta v_z}{\overline{v_z}}$ for different maximum and mean velocities. The relative bandwidth $\frac{\Delta \lambda}{\lambda}$ is equal to this quantity.

4.3.3. Transversal coherence

Even for a perfectly monochromatic wave interference effects can only be observed if the amplitudes at different grating slits are also sufficiently correlated. The characteristic length scale over which this is the case is called coherence width W_c. As a general guideline, this width has to extend over at least one grating period d. The transverse coherence is limited by the fact that a realistic source, like the one used in the experiment, has a finite physical size. This can be modelled by an array of independent point sources. The transverse coherence is consequently usually very small close to the source. In general the degree of coherence however increases with larger distance from the source. This is described by the van Cittert–Zernike theorem. In brief, its statement is that the mutual coherence function at equal times is proportional to the Fourier transform of the intensity distribution at the source (i.e. the shape of the source). One finds that the coherence width at a distance L from a source with diameter D_S is given by

$$W_c = \frac{\lambda \cdot L}{D_S} \tag{4.12}$$

Here we treat the problem one-dimensionally, since the grating is only periodic along one axis we are only interested in interference effects in that direction. More generally one might want to consider diffraction in two transverse dimensions. In this case the coherence area A_c is introduced, which scales quadratically with the distance to the source [203, 209, 216]. The coherence width (4.12) can also be derived directly in the Wigner formalism introduced in section 5.1 as the characteristic length scale over which the off-diagonal elements of the density matrix decrease [217]. An intuitive way to understand the limitations introduced by finite transverse coherence is to consider that molecules emitted by the source will have random transverse momenta [213]. This momentum distribution gives rise to a divergence of the molecular beam. If the source is spatially extended, a range of different initial momenta can reach the grating. The beam divergence will be imprinted onto the intensity distribution at the detector, as the diffraction patterns of the individual molecules will be shifted proportionally to their transverse momenta. Since this effectively broadens the diffraction peaks, one will only be able to observe good interference contrast if the divergence angle of the molecular beam arriving at the detector is smaller than the diffraction angle. Assuming the extension of the grating to be small compared to the source and detection regions (as is usually the case when applying the far-field approximation) one can estimate the divergence angle after the grating to be $\theta_{\text{div}} \approx \frac{D_S}{L}$. Requiring this to be smaller than the diffraction angle $\theta = \frac{\lambda}{d}$ again yields the condition $W_c \simeq d$ for the coherence width defined in (4.12) [212].

4.3.4. Transversal collimation

The oven source used for the measurements conducted at light gratings (see section 4.2) has a size of $D_S = 200\,\mu\mathrm{m}$. For a typical de Broglie wavelength of $\lambda_{\mathrm{dB}} \simeq 4\,\mathrm{pm}$ (see table 2) and a grating period of $d = 133\,\mathrm{nm}$, the grating would need to be at a distance of $L \simeq 6.65\,\mathrm{m}$ from the source in order to achieve a coherence width $W_c \simeq d$. The true distance between the source and the grating is almost an order of magnitude smaller (see table 1). In order to prepare the transverse coherence needed for the diffraction experiment a set of two collimation slits is used. The slits restrict the transverse momenta, which can travel through the setup, thus reducing the divergence angle of the beam below the width needed to resolve diffraction peaks. The increased transverse coherence can also be understood from the point of view that the collimation restricts the region in the source from which the molecules can originate, thus effectively reducing the size D_S of the source [4, 218].

We can estimate the divergence angle θ_{div} from geometric considerations as sketched in figure 4.7. This assumes classical trajectories and a negligible thickness of the slits. Since the source size is typically much larger than the slits, we do not take it into account here.

$$\tan\frac{\theta_{\mathrm{div}}}{2} = \frac{S_{1,x} + S_{2,x}}{2\Delta z_{21}} \tag{4.13}$$

$S_{1,x}$ and $S_{2,x}$ are the widths of the slits and Δz_{21} is their distance. In our setup we have $\Delta z_{21} \simeq 30\,\mathrm{cm}$ (see table 1). For $\lambda_{\mathrm{dB}} \simeq 4\,\mathrm{pm}$ and $d = 133\,\mathrm{nm}$ the expected diffraction angle is $\theta \simeq 30\,\mu\mathrm{rad}$. Therefore the condition for the divergence angle (4.13) to be smaller than that is $S_{1,x} + S_{2,x} \lesssim 9\,\mu\mathrm{m}$.

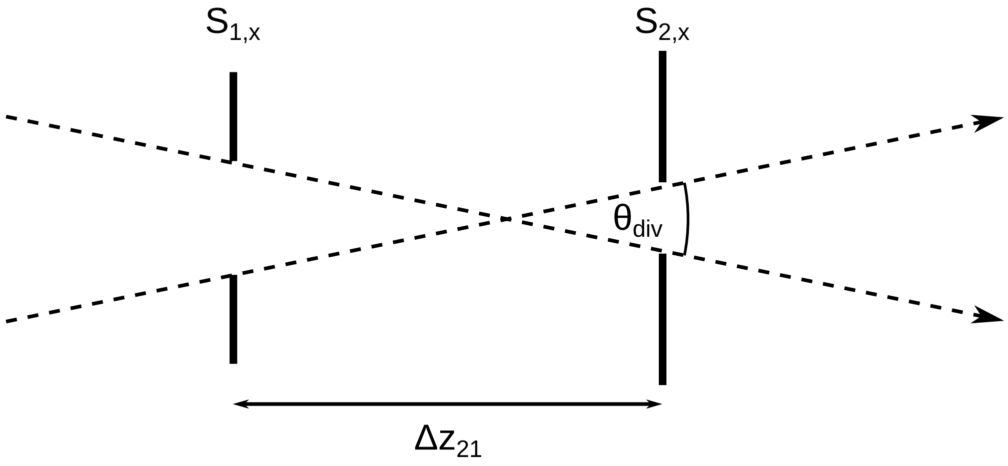

Figure 4.7: Geometrical estimate of the transversal collimation angle θ_{div}

The classical treatment of the slits is certainly justified for the first slit as the source can be considered approximately completely incoherent because of its comparatively large size. For very small widths diffraction at the second slit might however become relevant as the first slit provides some transversal coherence [219, 220]. In our theoretical treatment in section 5.4 we will account for this by only approximating the first slit as classical.

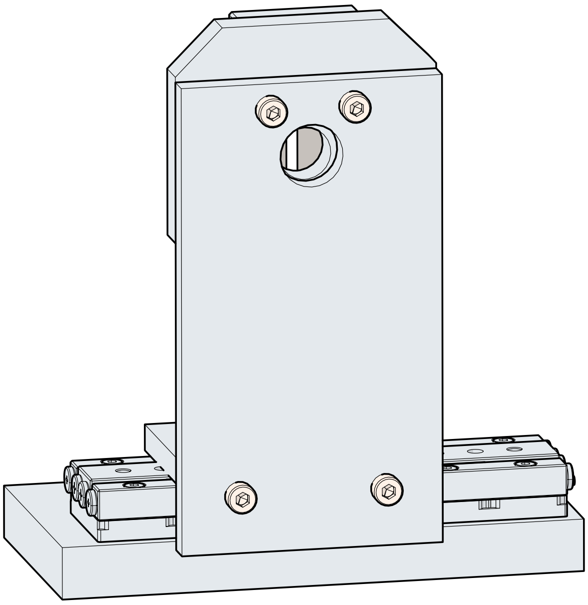

Figure 4.8: Sketch of the assembly of the transversal collimation slits. The molecular beam passes through the circular opening and is collimated by two razor blades mounted on a piezo. The slits are mounted to a rigid bar as shown in figure 4.11

The slits used here are made of two razor blades mounted on a piezo. Figure 4.8 shows a sketch of the slit assembly. Because the piezos can only provide position data relative to the setting where they are completely open, their absolute opening widths are not directly accessible. We calibrate the relative change in width by observing the diffraction pattern of a $\lambda = 532\,\mathrm{nm}$ laser sent through the slits at different piezo settings. The distances between the first minima Δx_1 and between the second minima Δx_2 of the diffraction pattern were measured at a distance of l from the slit. The corresponding widths of the slit are then calculated via [204]

$$S_x = \frac{2n\lambda l}{\Delta x_n} \tag{4.14}$$

where $n = 1, 2$ for the first and second minima respectively. The results for the calibration of first slit are plotted in figure 4.9. The corresponding parameters for the linear fits are collected in table 3. The slope of the fits shown in these figures are all $A \approx -1$. The slits are thus further closed for larger position values and we see good agreement for the relative change in width displayed by the piezo readout. The constant coefficients from the linear fits could be used to give an estimate of the piezo positionings for zero slit widths, i.e. for completely closed slits. However, because the razor blades forming the slits are not necessarily perfectly parallel, the true width seen by the molecular beam might have a constant offset from this value if it hits the slit at a different hight than the calibration laser. We therefore instead observe at which slit setting no transmission is visible anymore and use this value as the zero width for the slits. We find that the slits show no transmission for the settings $S_{1,x} = (201.0 \pm 0.5)\,\mathrm{\mu m}$ and $S_{2,x} = (124.5 \pm 0.5)\,\mathrm{\mu m}$ respectively. In principle we could try to use these values to compute the actual widths from the readout values of the piezos. However, since it is not possible to experimentally ensure that the height at which the molecular beam passes the slits never changes, this might not always give accurate results or at least requires regular recalibration. Instead we optimize the slit widths to fit the observed collimation angle for our theoretical discussion, was is described in section 6.3.

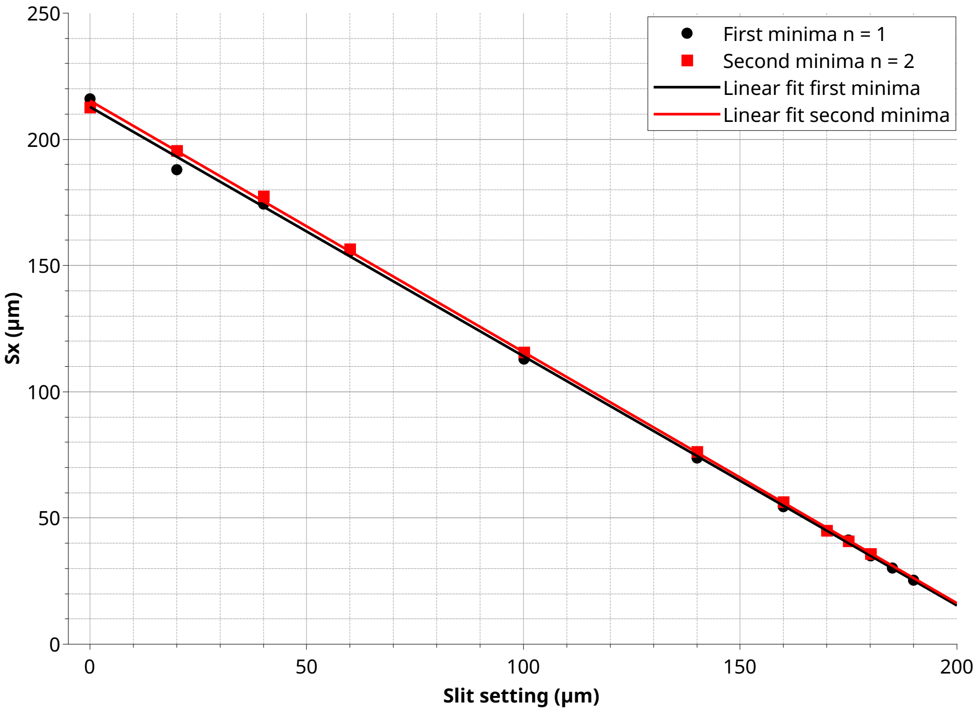

Figure 4.9: Comparison of slit widths computed via the first and second diffraction minima and the value of the piezo readout (slit setting). For this calibration the diffraction minima were measured at a distance of $l = 136\,\mathrm{cm}$. The computed parameters for the linear fits shown in this figure are given in table 3.

n	A	B	R^2
1	-0.988 ± 0.009	$(212.9 \pm 1.3)\,\mu\mathrm{m}$	0.9992
2	-0.995 ± 0.006	$(215.3 \pm 0.8)\,\mu\mathrm{m}$	0.9997

Table 3: Computed parameters for the linear fits $S_x = A \cdot x = B$ shown in figure 4.9 for minima $n = 1, 2$. $A \approx -1$ indicates that relative changes in width are correctly represented by the setting of the piezo.

4.4. Light grating

The molecules in this experiment are diffracted at a light grating with a wavelength of $\lambda = 266\,\mathrm{nm}$. The UV light is generated via second harmonic generation (SHG) [212, 221] from a $532\,\mathrm{nm}$ laser beam. As discussed in more detail in section 5.5 a standing light wave acts as a periodic dipole potential for a polarizable molecule. In addition to the effects of absorption this creates the necessary periodic modulation of the incoming matter-wave, which is needed to observe diffraction. An overview of the optical setup used to implement this standing light wave is sketched in figure 4.10.

The $532\,\mathrm{nm}$ light is provided by a *Coherent Verdi V-10*. This commercial Nd:YVO$_4$ laser generates the desired wavelength by doubling $1064\,\mathrm{nm}$ light internally also employing SHG in a LBO crystal [222]. The green light passes an attenuator formed by the half-wave plate $\lambda/2$ A and PBS 1. The laser light then enters an external frequency doubler as indicated in figure 4.10. The waveplate $\lambda/2$ B and the lens L1 ensure the proper coupling. The doubler used is a *WaveTrain 2* by *Spectra Physics*, it uses a BBO crystal within a triangular cavity for SHG [223, 224]. Further details on the frequency doubling

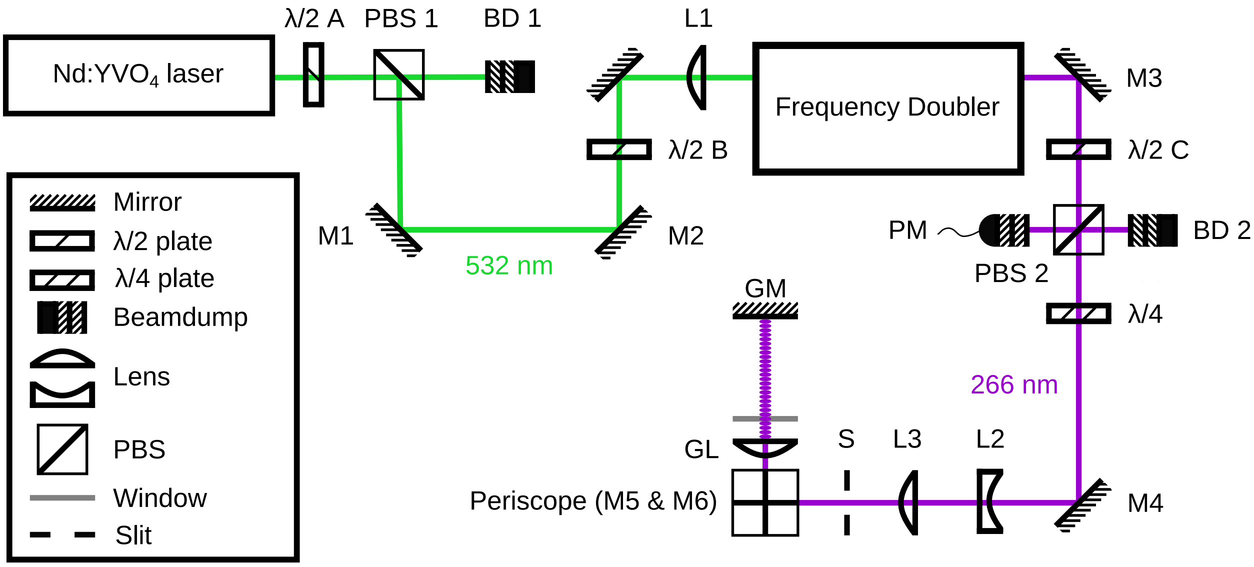

Figure 4.10: Sketch of the optical setup used for generating the UV light grating. $532\,\mathrm{nm}$ light is generated by the Nd:YVO$_4$ laser and sent to the frequency doubler. The $266\,\mathrm{nm}$UV light passes through an optical isolater and an beam expander and is finally focused onto the grating mirror GM by the grating lens GL.

will be given in section 4.4.1. The doubled light passes the half-wave $\lambda/2$ C followed by PBS 2 and the quarter-wave plate $\lambda/4$. Adjusting the polarization of the UV light with the half-wave plate $\lambda/2$ C allows modifying the intensity transmitted to the experiment. The quarter wave-plate $\lambda/4$ prevents the back reflected beam of the standing light wave from re-entering the frequency doubler by redirecting it to the power meter PM at one of the ports of the polarizing beam splitter (PBS). As a consequence of this the standing light wave is circularly polarized. The power meter PM additionally allows for monitoring the relative fluctuations of the UV laser power during the course of the experiment. As shown in figure 4.10 the UV light transmitted through the wave plates and PBS 2 is first magnified by a 2x beam expander made up of a lens L2 ($f = -50\,\mathrm{mm}$) and lens L3 ($f = 100\,\mathrm{mm}$). It is then brought to the grating lens GL ($f = 250\,\mathrm{mm}$) by a periscope formed by the mirrors M5 and M6. Enlarging the waist of the beam with the beam expander allows this lens to achieve a smaller beam diameter at the focus [212]. The periscope is mounted on a translation stage, which allows it to be translated in the z direction. The upper mirror of the periscope is mounted on another translation stage, which enables it to be moved vertically. The combination of these two degrees of freedom allows free positioning of the beam exiting the periscope within the y-z plane. The $f = 250\,\mathrm{mm}$ lens GL is attached directly to the upper periscope mirror, this way the laser beam always stays on the optical axis of the lens when being translated. The lens GL focuses the UV laser onto the grating mirror GM located within the vacuum chamber. The beam is retro reflected from this mirror, forming the standing light wave used for the diffraction experiment. The back propagating beam is overlapped with the incoming beam by adjusting the final mirror M6 of the periscope. It is then redirected to the power meter PM at one of the ports of PBS 2 as described above.

The grating mirror is mounted on an steel bar together with the collimation slits in order to prevent any relative movement between them. A sketch of this assembly is shown in figure 4.11. The mirror mount itself sits on a translation stage, which is able to move it along the x axis, and a piezo rotation stage. The latter is able to change the angle of the mirror around the vertical (y) axis (*yaw angle*). As will be further discussed in section 4.5.2 it is important to adjust this angle to make the surface of the mirror as parallel to the molecular beam as possible, which is the reason why precise control of it is needed. The assembly of the grating mirror on these stages is sketched in figure 4.12.

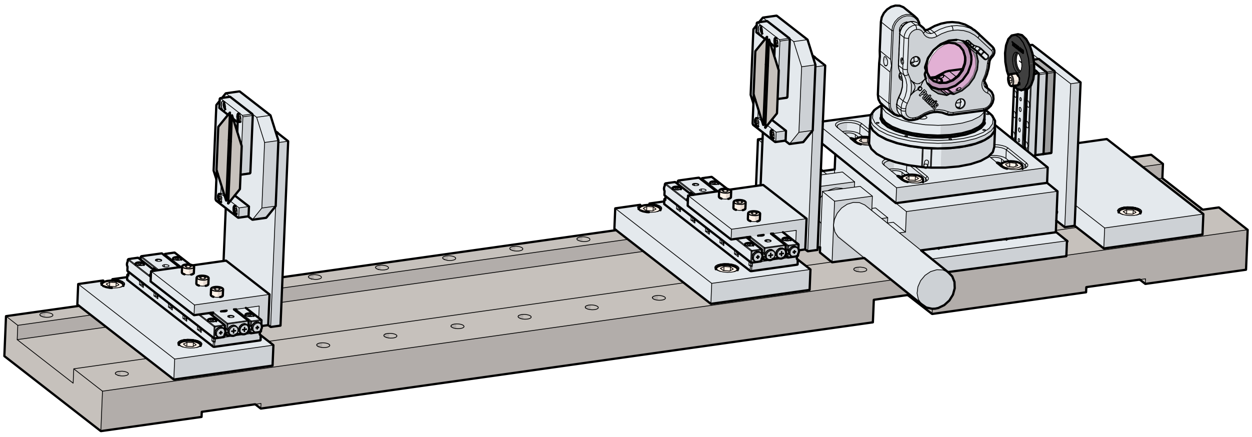

Figure 4.11: The bar on which the transversal collimation slits $S_{1,x}$, $S_{2,x}$, the grating mirror and the velocity selector S_y are mounted (from left to right). A more detailed view of the grating mirror is shown in figure 4.12.

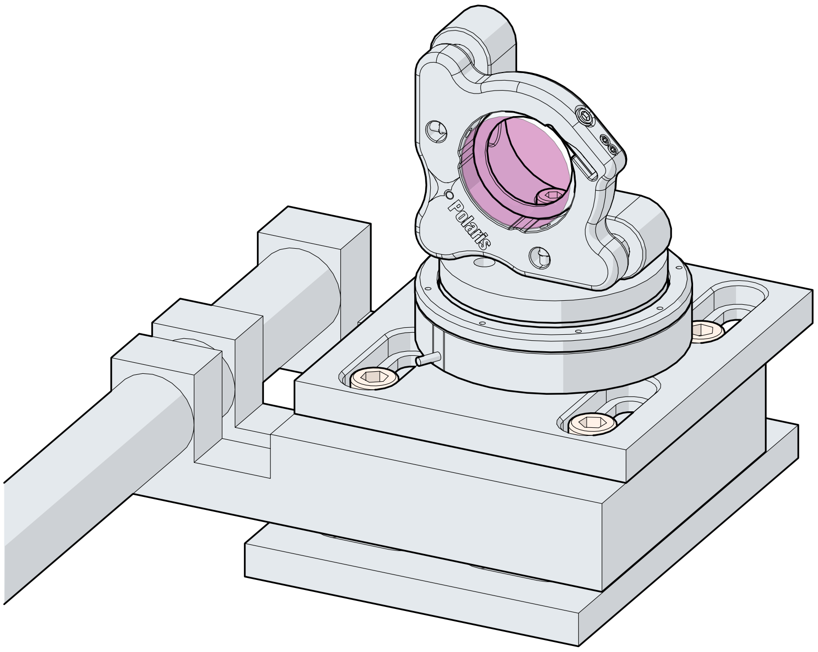

Figure 4.12: Sketch of the grating mirror assembly. The mirror mount sits on a rotation stage which itself sets on a linear translation stage, which can move the mirror along the x axis.

4.4.1. Second harmonic generation

Second harmonic generation (SHG) is a special form of sum frequency generation. It allows coherent light of (angular) frequency ω to be converted into coherent light of twice that frequency 2ω. The physical principle this is based on is the non-linear dielectric response of an optical medium to an electric field. The dependence of the (dielectric) polarization $\mathbf{P}$ on an external electric field $\mathbf{E}$ may be written as an expansion of the form

$$P_\alpha = \varepsilon_0 \left(\chi^{(1)}_{\alpha\beta} E_\beta + \chi^{(2)}_{\alpha\beta\gamma} E_\beta E_\gamma + \chi^{(3)}_{\alpha\beta\gamma\delta} E_\beta E_\gamma E_\delta + \dots \right) \tag{4.15}$$

The linear susceptibility $\chi^{(1)}$ is joined by the higher order non-linear susceptibilities $\chi^{(2)}$, $\chi^{(3)}$ and so forth. They are given by tensors of rank $2, 3, 4, \dots$ respectively. We use the usual sum convention for writing equation (4.15). In general the susceptibilities of increasing orders are very small, thus they only become relevant for very strong light fields. In the following discussions we will restrict ourselves to the second order in (4.15), as this the one responsible for second harmonic generation. It should be noted that the second order susceptibility is in general only non-zero for materials without inversion symmetry [221, 225–227].

Strictly speaking (4.15) is only true for slowly varying electric fields as it assumes that the response of the material is instant. In a more physical formulation one has to consider that the polarization at time t will depend on the electric field at all times $t' < t$. For electromagnetic radiation it is then instructive to look at the Fourier components of the quantities in equation (4.15). The Fourier component of the second order in the expansion of $\mathbf{P}$ is then given by

$$P^{(2)}_\alpha \left(\omega = \omega_1 + \omega_2\right) = \epsilon_0 \chi^{(2)}_{\alpha\beta\gamma} \left(\omega_1, \omega_2\right) E_\beta(\omega_1) E_\gamma(\omega_2) \tag{4.16}$$

Similar relations exist for the other orders. Note that the second order susceptibility is in general also frequency dependent. We see from equation (4.16) how two electromagnetic fields with frequencies ω_1 and ω_2 will give rise to a polarization with the sum of the two frequencies. If only light of frequency ω_0 is initially present this will yield twice the initial frequency $\omega = 2\omega_0$. The non-linear dielectric polarization $\mathbf{P}'(\omega)$ couples to the light field with frequency ω via a non-linear wave equation. Thus electromagnetic radiation at the new frequency ω will be created as well [226, 228].

The conversion efficiency of light with frequency ω_0 to $2\omega_0$ will be very low unless the *phase mismatch factor*

$$\begin{aligned} \Delta k &= 2k_{\omega_0} - k_{2\omega_0} \\ &= \frac{2\omega_0}{c} \cdot \left(n(\omega_0) - n(2\omega_0)\right) \end{aligned} \tag{4.17}$$

is zero or at least close to it. Because of dispersion the refractive indices are typically not equal for both frequencies ($n(\omega_0) < n(2\omega_0)$). Intuitively we can understand that $\Delta k \neq 0$ corresponds to different speeds of propagation within the medium for the fundamental (ω_0) and harmonic ($2\omega_0$) wave. Light converted at different points within the e.g. crystal will then not be in phase [225, 228–231].

Second harmonic generation can also be understood from a quantum point of view. The second order susceptibility $\chi^{(2)}_{\alpha\beta\gamma}$ introduces three photon interaction terms into the Hamiltonian. The conversion of light from the fundamental frequency to the harmonic is then described by the annihilation of two photons with frequency ω_0 and the creation of one with frequency $2\omega_0$. The phase matching condition $\Delta k = 0$ is then simply a consequence of the conservation of momentum during this process [226, 228].

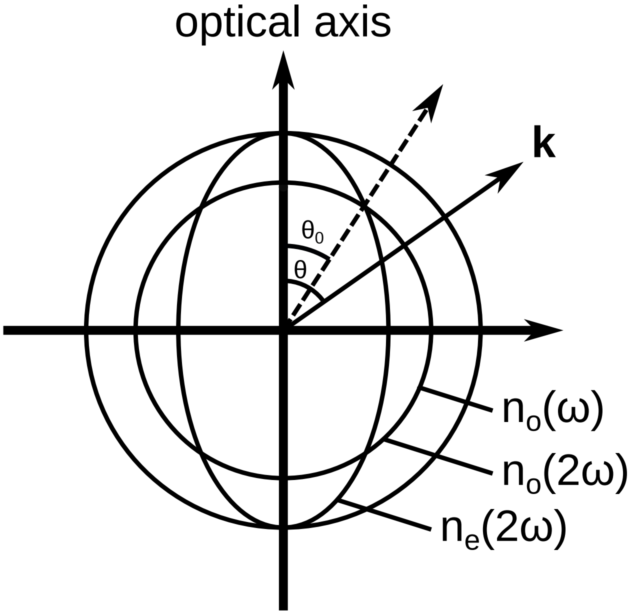

Figure 4.13: Type 1 critical phase matching. If the beam propagates at an angle θ_0 with respect to the optical axis of the crystal the refractive indices of the ordinary beam at frequency ω and the extraordinary beam at 2ω become equal. Adapted from [226].

A common way to achieve phase matching is to use birefringence. In an uniaxial crystal the effective refractive indices for light with ordinary polarization n_o is independent of the direction of propagation (relative to the crystal axis), the index for extraordinary polarization is however n_e not. In type 1 critical phase matching the fundamental beam has ordinary polarization and the harmonic has a component with extraordinary polarization. As indicated in figure 4.13 there is a particular angle between the propagation direction and the crystal axis θ_0 (phase matching angle) for which $n_o(\omega_0) = n_e(2\omega_0)$. Type 2 critical phase matching differs from this by having a fundamental beam with both ordinary and extraordinary polarization components, which leads to a slightly different condition, where the average refractive index for the fundamental beam must match the one for the extraordinary harmonic beam. Another phase matching method is non-critical phase matching. In this case the propagation direction of the light is chosen orthogonal to the crystal axis and the refractive indices are tuned to match by changing the temperature of the crystal. While the range over which this tuning is possible is usually smaller than what can be achieved with critical phase matching, non-critical phase matching avoids beam walk-off (see below)[225, 226, 228, 232].

The frequency doubler used in this experiment employs critical phase matching. The BBO is placed in a triangular cavity which is locked using Pound–Drever–Hall method. The cavity enhances the intensity of the fundamental wave and increases the effective interaction length within the crystal [223, 228, 233]. For a typical input power of $5\,\mathrm{W}$ $532\,\mathrm{nm}$ light one gets around $1.2\,\mathrm{W}$ UV output at $266\,\mathrm{nm}$. Due to losses at other optical components along the beam path from the frequency doubler to the vacuum chamber as sketched in figure 4.10 the power directly in front of the laser window is lower, usually around $1\,\mathrm{W}$. While staying locked at large input powers for a longer time period without adjustments to the doubling cavities the power output decreases slightly. As mentioned, the power meter PM records the UV power reflected from the grating mirror, which gives information of the relative decrease in output power of the UV light. Typically the power drops by around $10 - 15\ \%$ over the course of a typical measurement lasting $2 - 2.5\,\mathrm{h}$. The decrease in conversion efficiency can most likely be attributed to thermal drifts in the doubling cavity and potentially degradation of the non-linear crystal.

In general the harmonic output power is proportional to the square of the fundamental power.

$$P_{2\omega_0} = C \cdot P_{\omega_0}^2 \tag{4.18}$$

A comprehensive study of SHG for the realistic case of focused Gaussian beams and their optimal parameters has been given by Boyd and Kleinman [234]. It turns out that for such Gaussian beams the phase matching condition $\Delta k = 0$ is no longer the optimal case. Instead there is some value $\Delta k > 0$ for which this is the case [234, 235].

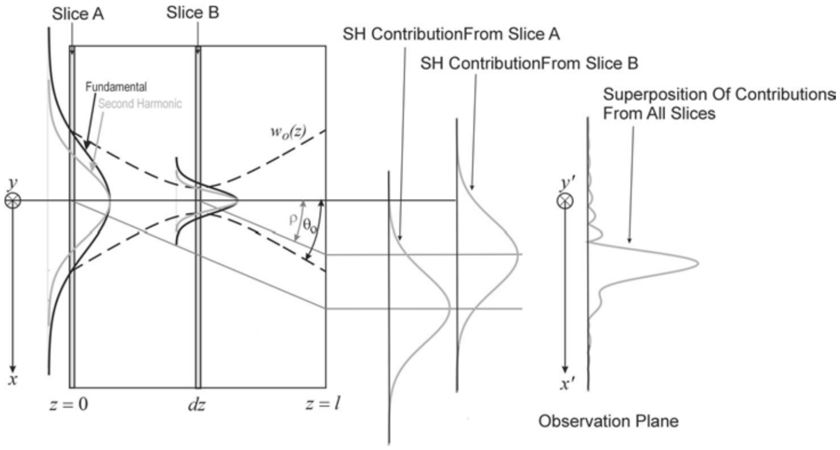

Figure 4.14: Effect of beam walk-off of the second harmonic within a non-linear crystal on the output beam. Reproduced from [235].

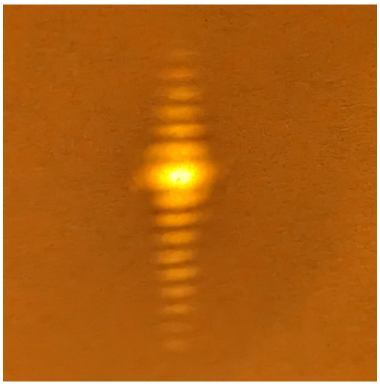

Figure 4.15: Photograph of the beam emitted by the frequency doubler hitting fluorescent paper. A larger number of weaker side fringes are located above and below the nearly Gaussian main lobe.

As mentioned, a drawback of critical phase matching as used here is that the extraordinary beam in a birefringent material experiences beam walk-off. As a consequence the extraordinary second harmonic light will travel through the crystal at some double-refraction angle ρ with respect to the fundamental beam. As illustrated in figure 4.14 this will cause contributions from different depths within the crystal to not fully overlap. As a consequence the harmonic output beam is in general no longer Gaussian. Instead it shows a characteristic "edge" shape, with bright fringes to one side and much weaker fringes to the other [235–237]. In the commercial frequency doubler used here this non Gaussian profile is partially compensated by beam shaping optics [223]. Nevertheless, the output beam still features additional fringes. Figure 4.15 shows a photo of the $266\,\mathrm{nm}$ harmonic laser spot hitting fluorescent paper. One can clearly see the fringes along the vertical axis to both sides of the nearly Gaussian main peak. In figure 4.16 a beam profile along the vertical axis of the harmonic is shown. It was recorded after the slit

S at the location of the periscope (see figure 4.10) using a *Coherent BeamMaster BM-7 (UV)*. From the beam profile in figure 4.16 we can deduce that approximately $80\ \%$ of the laser power are contained within the main peak, making the contribution to the fringes very low. To have a well characterized beam for the interference experiments an adjustable slit is used to cut out the outer fringes from the beam. The slit S is placed directly after the beam expander formed by lenses L2 and L3 as indicated in figure 4.10, where the beam diameter is large enough to position the slit appropriately. In figure 4.17 a beam profile similar to figure 4.16 is shown with the adjustable slit in place.

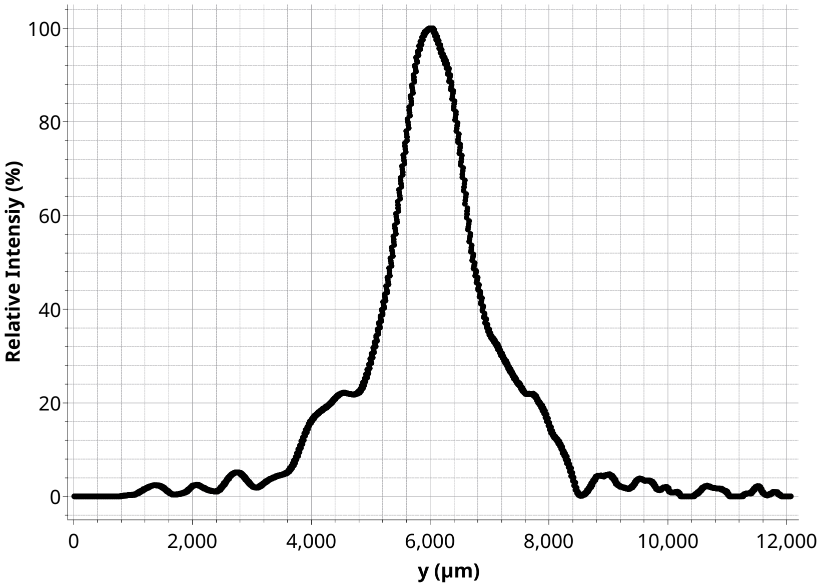

Figure 4.16: Beamprofile of the UV laser along the vertical axis without slit S. Several smaller side peaks are visible but they are significantly smaller than the main lobe.

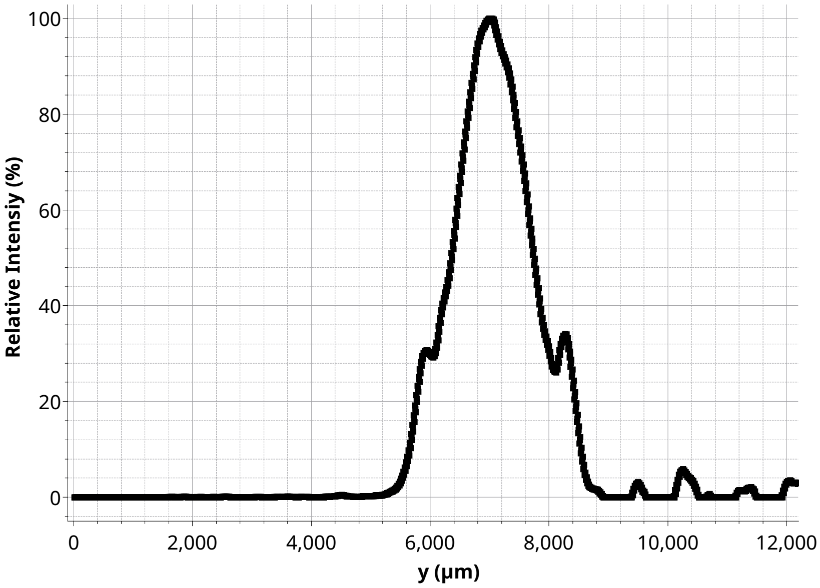

Figure 4.17: Beamprofile of the UV laser along the vertical axis with slit S. The slit cuts off most of the side lobes leaving a profile that is closer to an ideal Gaussian.

4.4.2. Fiber beam profiler

As will become apparent in our theoretical analysis (see section 5.5), it is necessary to know the beam waist of the UV light grating at the location of interaction with the molecules. Since the relevant light-grating interactions (phase shift and number of absorbed photons, see equations (5.28) and (5.30)) scale with $\frac{P}{w_y}$ for Gaussian beams (P laser power, w_y waist radius in vertical direction), it is clear that we need a very small waist w_y to get considerable interaction strengths. To accurately determine this waist radius we measure the vertical profile of the laser beam in situ using a fiber based beam profiler [238]. This fiber also serves a second purpose in facilitating the alignment of the light grating to the molecular beam (see section 4.5.3). In the setup used here the fiber is mounted on a vertical translation stage inside the vacuum chamber. It is glued to a post attached to this stage oriented along the vertical axis. The fiber is a *Thorlabs* high OH UHV fiber with a $100\,\mu\mathrm{m}$ core and 0.22 NA. The end attached to the vertical translation stage has been cut and polished to create scattering centers. The other end is attached to a vacuum feed through and connected to a power meter (*Newport* 818-UV). When the laser beam hits the cut end of the fiber light couples into the fiber. When moving the fiber vertically through the beam the power coupled into the fiber is given by the convolution of the intensity profile of the beam itself and the effective diameter of the fiber core [238]. Since the fiber is cut at a shallow angle and mounted almost vertically this effective diameter is much smaller than the $100\,\mu\mathrm{m}$ core size. A *Heidenhain* linear encoder is used to readout the vertical position of the stage holding the fiber. The power and position measurements are automatically recorded by a custom *LabVIEW* script. The waist radius $w(x)$ of the (approximately) Gaussian beam with the vertical intensity profile [212]

$$I(x,y) = I_0 \left(\frac{w_0}{w(x)}\right)^2 \cdot \exp\left(-\frac{2y^2}{w^2(x)}\right) \tag{4.19}$$

is then extracted by fitting a generic Gaussian function

$$f(y) = \frac{A}{w} \cdot \sqrt{\frac{2}{\pi}} \cdot \exp\left(-2 \cdot \left(\frac{y-y_0}{w}\right)^2\right) \tag{4.20}$$

to the recorded data. In the experimental setup the distance between the grating mirror and the grating lens GL is chosen to locate the focus of the beam at the mirror by assuring that the back propagating beam has the same diameter as the incoming one. The molecular beam passes $0.32\,\mathrm{mm}$ away from the mirror surface. The fiber measures the beam waist at the same location as the molecular beam (see section 4.5.3). For this purpose the grating mirror is moved away from the location along the x-axis at which it sits during the measurements using the translation stage it sits on. It is also rotated by 1° to redirect the reflected beam such that it cannot interfere with the waist measurement. The waist radius is at the order of $w_0 = 15\,\mu\mathrm{m}$ in this experimental setup. The Rayleigh range [212]

$$z_0 = \frac{\pi w_0^2}{\lambda} \tag{4.21}$$

is thus approximately $z_0 \approx 2.7\,\mathrm{mm}$. This is much larger than the distance of the mirror surface to the molecules and the widths of the collimation slits $S_{1,x}$ and $S_{2,x}$. Consequently we can assume the waist radius to be constant $w(x) \approx w_0$ over the interaction region between the light grating and molecules.

In figure 4.18 we show an example of a waist measurement recorded in situ in the experiment. A fit of the form (4.20) is also shown. For this example the extracted waist radius is $w_0 = (16.04 \pm 0.06)\,\mu\mathrm{m}$. To ensure the accuracy of these waist measurements, the results were compared with the profiles recorded by a *Coherent BeamMaster BM-7 (UV)* knife edge beam profiler. Since this profiler could not be placed inside the vacuum chamber, the corresponding profiles were measured by redirecting the $266\,\mathrm{nm}$ laser by a mirror placed in front of the laser window. The profile of the UV laser at measured at the focus is shown in figure 4.19. The waist radius $w_y = (15.51 \pm 0.02)\,\mu\mathrm{m}$ agrees well with the result of figure 4.18. Note that these measurements were not taken together, thus variations in the positions of the lenses could cause the minor difference in the waist radii between the two measurements. A more rigorous comparison between the two beam profilers was conducted with $532\,\mathrm{nm}$ light by recording the waist radii at different positions along the beam path. For more information refer to appendix B

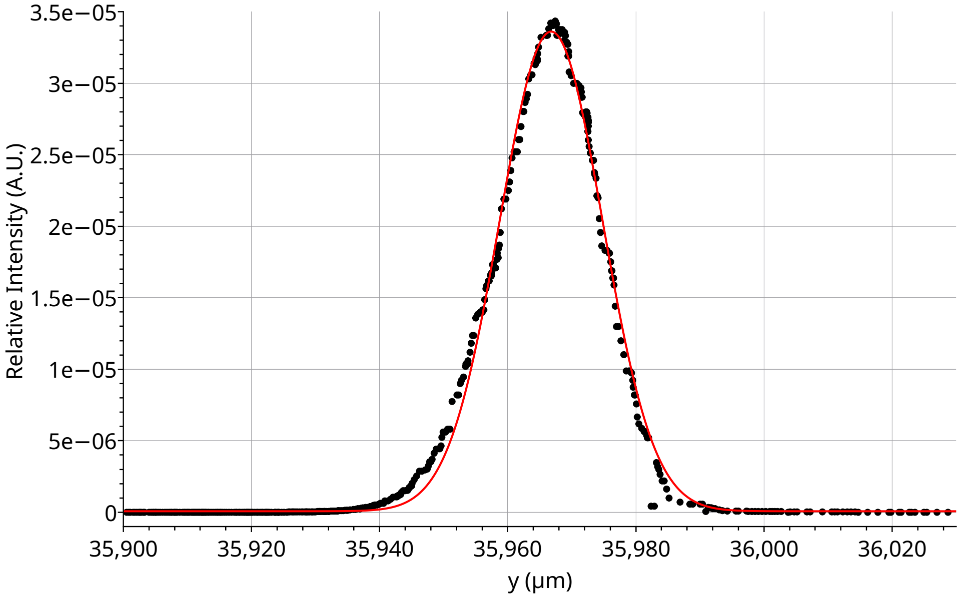

Figure 4.18: Typical waist profile of the grating laser at the focus recorded with the fiber beam profiler. A fit of the form (4.20) is shown in red. The fit gives a waist radius of $w_0 = (16.04 \pm 0.06)\,\mu\mathrm{m}$.

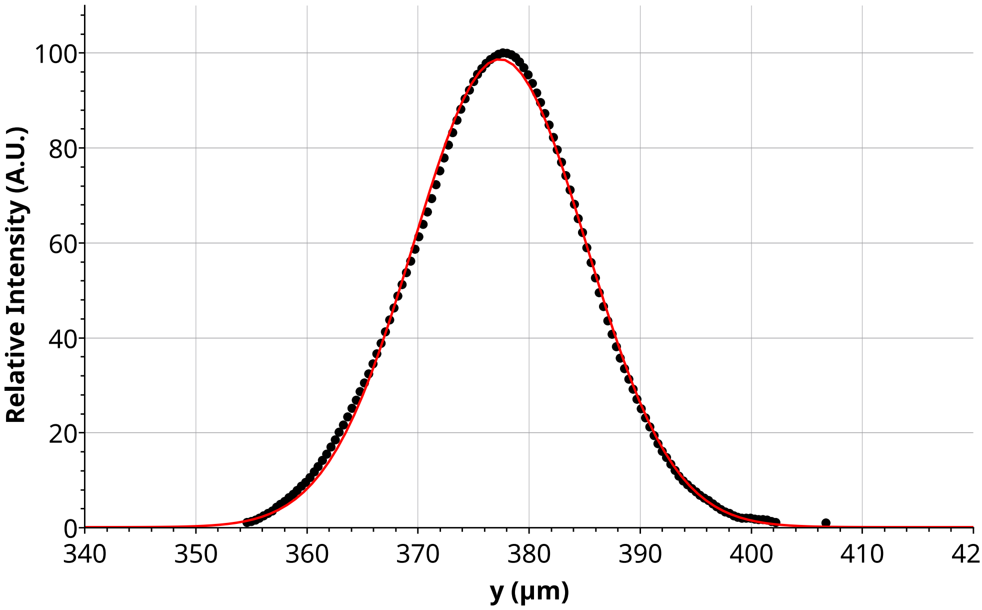

Figure 4.19: Vertical waist profile of the grating laser at the focus recorded with the knife edge beam profiler. A fit (4.20) is shown in red. The computed waist radius is $w_y = (15.51 \pm 0.02)\,\mu\mathrm{m}$.

4.5. Alignment procedures

4.5.1. Pre alignment of the source

As described in the previous sections, the molecules emitted by the source should pass through the collimation slits and eventually hit our detection region. Since the involved widths are all small compared to the overall length of $1.6\,\mathrm{m}$ of the experiment, it is necessary to pre align the components. To this end a $421\,\mathrm{nm}$ laser beam is sent through the experiment along the desired axis of the molecular beam. The laser is centered on the first vacuum flange on which the oven source is otherwise installed (left end of figure 4.2). The laser tilt is adjusted such that it reaches the window at the detection end of the vacuum chamber centered as well. The collimation slits $S_{1,x}$ and $S_{2,x}$ are positioned using to translation stages to allow the laser to pass through them. For the measurements at the light grating these positions will remain fixed. The two points will thereby define the axis of the molecular beam in the horizontal plane fully. Similarly, the velocity selection slit S_y is inserted and vertically positioned such that the $421\,\mathrm{nm}$ alignment laser can pass through it. This position will be taken as a starting point for the exact alignment later. The fiber profiler described in section 4.4.2 is positioned such that its tip hits the alignment laser. The power meter connected to the other end of the fiber can be used to precisely find this location.

After reinstalling the oven source and heating it to the desired temperature, its horizontal position is optimized by maximizing the signal transmitted through the two collimation slits. The oven is mounted on a 2 axis translation stage to allow for these adjustments in the x-y plane. The velocity selector S_y is inserted and its position is initially optimized to get transmission at the detection height. In order to get reproducible alignment of the molecular beam for subsequent measurements the height of the velocity selector S_y is kept fixed from this point on. While the S_y position can be positioned and read out with an accuracy of $40\,\mathrm{nm}$ thanks to the piezo stage it is mounted on, the vertical positioning of the source itself is not easily reproducible. This is due to the limited resolution of the translation stage the oven is mounted on and the fact that the construction of the source itself is prone to deformation due to thermal effects during heating. In order to still position it accurately enough the vertical oven position is adjusted to the transmission at the detection. The detector height is kept fixed and the vertical profile of the transmission is recorded. A Gaussian is fitted to this profile to find the approximate center. The oven height is adjusted to yield the same center position for every measurement run. Since the mean velocities of the molecules are defined by the temperature of the oven, the two fixed points (S_y slit and center at detection) should suffice to fully define the flight parabolas. The center of this Gaussian fit of the transmission through the S_y slit can be found with an accuracy better than $10\,\mathrm{\mu m}$. As sketched in figure 4.20 we can use a simple geometrical consideration to estimate the accuracy of the vertical oven position found this way as $\frac{90\,\mathrm{cm}}{70\,\mathrm{cm}} \cdot 10\,\mathrm{\mu m} \approx 13\,\mathrm{\mu m}$. This position can easily adjusted with the $10\,\mathrm{\mu m}$ resolution of the micrometer screw used to position the oven. A similar geometrical argument lets us estimate how reproducible the height of the molecular beam is at the location of the light grating. We can estimate it as $\frac{9\,\mathrm{cm}}{70\,\mathrm{cm}} \cdot 10\,\mathrm{\mu m} \approx 1.3\,\mathrm{\mu m}$. This is an acceptable variation for the laser beam waist, which is at the order of $15\,\mathrm{\mu m}$.

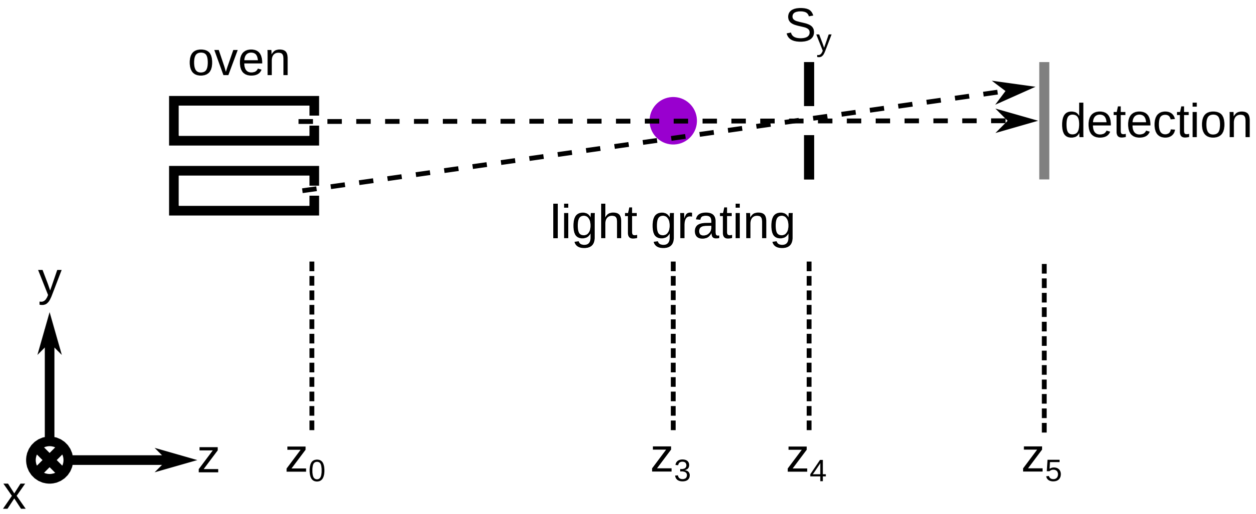

Figure 4.20: Geometrical estimation of the vertical alignment. The sketch shows a side view of the layout of the experiment. For a fixed center position of the velocity selector S_y the reproducibility of the vertical oven position can be estimated from the position of the transmission at the detection by simple geometric considerations. Similarly we can estimate the corresponding reproducibility of the molecular beam height at the position of the light grating.

4.5.2. Grating mirror alignment

There are three critical alignment parameters for the light grating and consequently the grating mirror, which defines the orientation of the standing light wave. As indicated in figure 4.21 two angles, denoted roll (axis along the molecular beam) and yaw (vertical axis), define the orientation of the light grating. Additionally the distance of the mirror surface to the molecular beam needs to be adjusted. To prevent the interference maxima of different velocity classes from mixing the roll angle has to be chosen such that the light grating is horizontal with respect to gravity [119]. The yaw angle has to be adjusted such that the molecular beam is perpendicular to the light grating, i.e. the molecular beam has to be parallel to the mirror surface. If the yaw angle deviates from this orientation interaction with neighbouring antinodes of the grating may average out, decreasing the interference contrast [8]. An imperfect yaw orientation would also change the effective period of the grating. A precise alignment of these angles is also necessary because we assume these orientations to be perfect for our theoretical analysis in section 5.

The roll angle of the grating is adjusted directly after installation of the mirror. To ensure that the mirror surface is as perfectly vertical with respect to gravity as possible the following alignment method is used. An alignment laser beam is sent to a mirror on top of an optical level (*Davidson Optronics* D-626). The mirror "floats" such that it is oriented perpendicular to gravity. The beam is reflected back to the source of the laser with this mirror. The beam pointing is now adjusted such that the back propagating beam overlaps with the incoming one vertically. Because the optical level is vertical with respect to gravity, this ensures that the alignment laser is propagating horizontally. The optical level is then rotated such that it reflects the alignment laser to the grating mirror. The roll angle of the grating mirror can then be set using the adjustment screws of the mirror mount, such that the back reflection from it also has perfect vertical overlap with the incoming beam. This aligns the grating mirror vertically with respect to gravity.

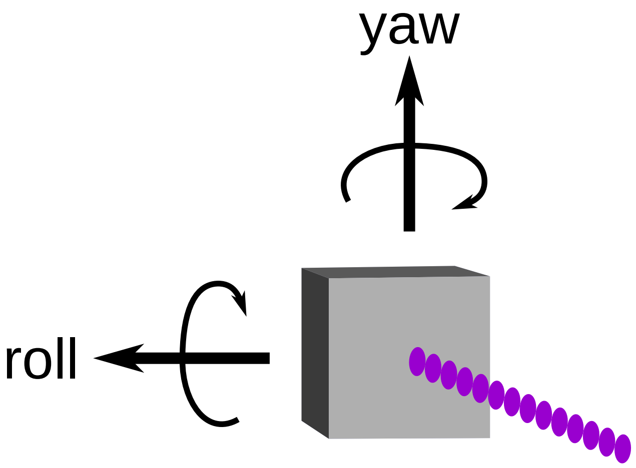

Figure 4.21: Definition of the roll and yaw angles of the grating mirror. Yaw is rotation around the y-axis, roll is rotation of the mirror around the z-axis. The orientation of the mirror also defines the direction of the light grating.

The approximate alignment of the yaw angle of the mirror is first found using the same alignment laser described in section 4.5.1, which propagates along the same axis as the molecules. The mirror is moved using the horizontal translation stage (along the x axis) on which it is sitting (see figure 4.12) until it clips the alignment laser. The angle of the mirror around the vertical axis is then adjusted to make the mirror surface parallel to this laser beam. For this first step this is judged visually by moving the mirror horizontally such that it just starts clipping the laser and comparing if this cut-off is symmetric at both ends of the mirror. The precise alignment of the yaw angle is conducted with the molecular beam itself. For this purpose the beam is collimated less tightly than later for the diffraction measurements. The translation stage is used to move the mirror into the beam as before. By observing the molecular beam at the detector we can determine when the mirror surface blocks part of the beam because the transmission becomes narrower in this case. A spacer ring has been added to the mirror mount to ensure that it sticks out by about $1\,\mathrm{mm}$ from the frame. This ensures that the mirror surface itself blocks the molecular beam and not the mirror mount itself. As sketched in figure 4.22 the amount by which the mirror cuts the molecular beam depends on its yaw angle and is minimized if the mirror surface is parallel to the beam. We can thus find the optimal yaw angle by measuring the width of the molecular beam for different yaw angles and finding the maximum. The yaw angle in the experiment can be reproducibly set using a *SmarAct* SR-5714C rotation stage, on which the mirror sits. It can be reproducibly set with better than $5\,\mathrm{\mu rad}$ accuracy. The values for the angle ϕ given below are with reference to the zero point of the rotation stage.

In practise the grating mirror is moved into the beam, and the yaw angle is changed until the width no longer increases. At this point the mirror has rotated out of the beam. It is then translated closer to the beam until it cuts the beam again. This procedure is repeated until one finds a local maximum of the width as a function of the yaw angle. This width should be smaller than the total width of the beam, measured with the grating mirror moved completely out of the way, to ensure that the mirror actually is clipping the beam. The result for this alignment in our experiment is shown in figure 4.23. The maximum beam width corresponding to parallel alignment of the mirror surface is found at $\phi_0 = 5.08°$. The values shown in figure 4.23 are only the widths recorded for the final step of the alignment. At this point the mirror was no longer moved along the x axis and the angle was scanned in finer steps than for the initial part of the alignment.

Note that this procedure only works as described if the vertical rotation axis is centered on the mirror itself. Otherwise the change in width is not symmetric and the correspondence between minimal width and a parallel mirror surface is broken. Another caveat is the fact that the projection of the circular mirror surface along the propagation axis of the molecules is elliptical. The cut-off is thus not a straight line. Unless the detector images the section of the molecular beam which traverses at the center height of the mirror, one will thus observe a width which is approximately linearly increasing / decreasing with height. In order to compare widths of cut-off beams for different yaw angles it is therefore necessary to always measure the width of the same (small) section of the detected beam.

The yaw angle found by this method is used as a starting point for scanning the diffraction measurements themselves in a small range around this point. This is scan is done after the other alignment steps described below have been completed. Since the effect, i.e. the intensity of the higher order peaks in the diffraction image, is stronger for better yaw alignment, we can find the true optimum by comparing these measurements. In our case this only led to a small correction with a new optimal yaw angle of $\phi_0 = 5.07°$.

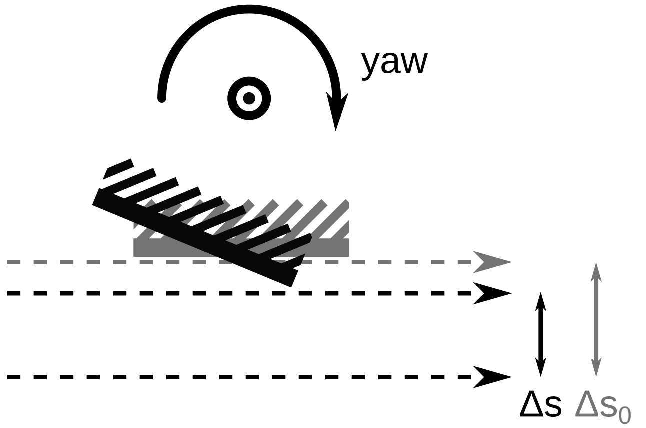

Figure 4.22: Alignment of the grating mirror yaw angle. The figure shows a top view of how the mirror cuts different amounts of the molecular beam depending on how parallel it is to the beam. The width of the transmitted beam takes on its maximum value Δs_0 when the mirror is parallel to the molecular beam (grey). For other angles the width Δs is reduced (black).

The alignment of the horizontal position of the mirror (along the x-axis) follows from the previous alignment steps. As discussed in section 4.4.2 the Rayleigh range of the grating laser is approximately $z_0 \approx 2.7\,\mathrm{mm}$. It is necessary for the molecular beam to pass the light grating close to the focus. This is required because we can only then neglect the wavefront curvature, which might cause the phases imprinted by the grating to be averaged out. Also being close to the focus means that the intensity of the light will be higher, which allows us to observe stronger diffraction effects. The grating laser has to be focused onto the grating mirror surface to ensure maximum overlap of the incoming and outgoing beams, which form the standing light wave. Consequently the distance between the mirror surface and the molecular beam needs to be small compared to the Rayleigh length. The surface however also cannot be to close as the mirror might otherwise (partially) block the molecules. To align this distance we first collimate the molecular beam to the same narrow divergence angle as is used for the actual diffraction measurements. The mirror is now moved along the x-axis until it blocks this beam and moved out in small steps until transmission is observed again. From this closest possible approach of the mirror to the beam of molecules we move away an additional distance of $0.32\,\mathrm{mm} \ll z_0$.

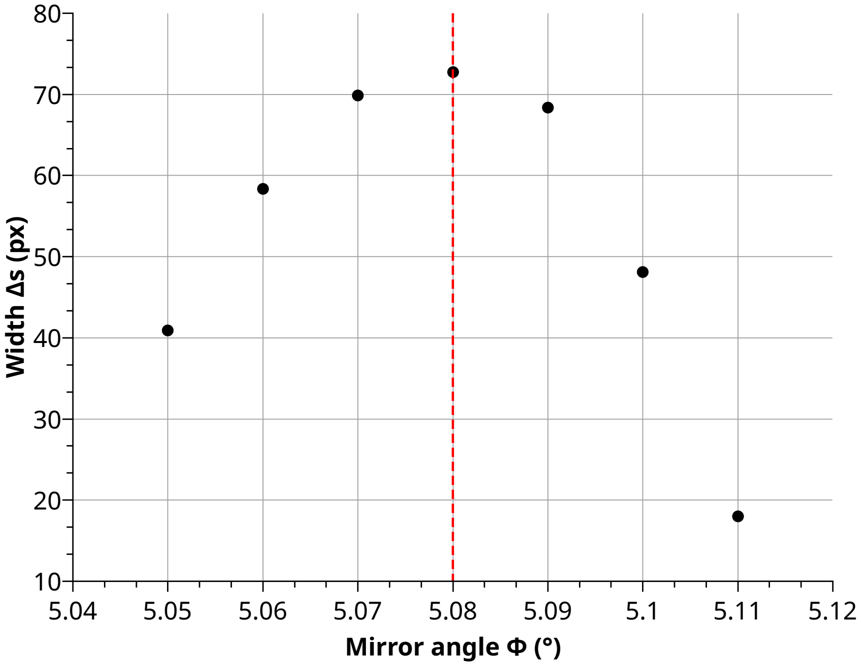

Figure 4.23: Results of the yaw alignment of the grating mirror using the technique illustrated in figure 4.22. The maximum beam width is observed for the yaw angle $\phi_0 = 5.08°$ marked in red.

4.5.3. Alignment of the light grating

As outlined already the UV laser needs to be retro reflected into itself to form the standing light wave. As illustrated in figure 4.24 it is also necessary that the focus is on the grating mirror surface for the incoming and outgoing beam to fully overlap. Otherwise only part of the beam can contribute to the standing light wave. In section 4.4 we briefly described how the final mirror of the periscope (M6 in figure 4.10) can be used to adjust the angle of the UV laser such that it is orthogonal to the grating mirror. The overlap of the incoming and reflected laser beam is checked in front of the slit S. To adjust the focus of the grating laser to the surface of the mirror we utilize the fiber beam profiler described in section 4.4.2. First the fiber is positioned in such a way that its tip blocks the collimated molecular beam. The translating degrees of freedom of the periscope are used to adjust the grating laser to the fiber tip in the y-z-plane. For this purpose the power measured at the other end of the fiber is monitored. From this position the fiber is translated $0.32\,\mathrm{mm}$ along the x-axis away from the grating lens GL. This is the same distance the mirror is moved away from its closest approach to the collimated molecular beam for the measurements. Thus the fiber will be positioned at the location where the mirror will be during measurements. Note that the grating mirror has to be further out to make space for the fiber for this procedure. We can now readjust the positioning of the grating laser and measure its profile using the fiber profiler as outlined in section 4.4.2. The grating lens GL is now translated along the beam axis (x-axis) and the waist is measured for each location. We find the location with the minimal waist, which corresponds to the focus at the mirror surface. Note that we can assume that translating the grating lens corresponds to simply translating the focus of the beam because we are far from the waist of the incoming UV laser and because it is not very divergent. Since the waist of a Gaussian beam focused by a lens only depends on the waist at the lens for a wavefront curvature much larger than the focal length, we get the same waist at the focus after the lens if the diameter of the incoming beam is approximately the same over the distance the lens is translated [212].

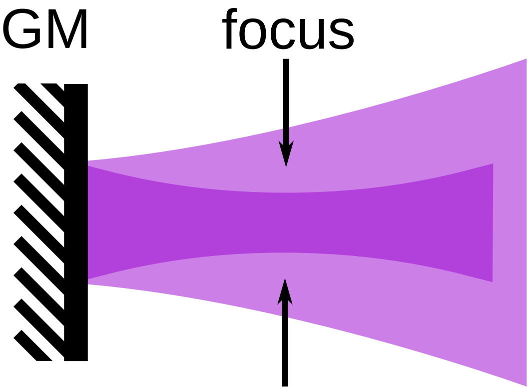

Figure 4.24: If the grating laser is not focused onto the grating mirror surface, the overlap between incoming and outgoing beam is imperfect.

After the angle and focus of the light grating have been aligned its position in the y-z plane needs to be configured such that the trajectories of the molecules overlap with the laser beam. This is sketched in figure 4.25. As mentioned in section 4.4 the periscope can be translated to adjust this position. The z position of the light grating does in fact not need to be aligned in a precise manner as the two beams may intersect at any point along the trajectory of the molecules. Small adjustments of the z position however allow moving the focus of the laser to a fresh spot on the mirror if necessary. This might be required in case the currently used one gets damaged. The y-axis alignment of the light grating is optimized by scanning the vertical position of the laser and recording diffraction measurements. Optimal overlap between the two beam corresponds to the most pronounced diffraction effect. This alignment is conducted for phthalocyanine $C_{32}H_{18}N_8$ (PcH_2). The other molecules listed in table 2 are still be approximately compatible with this alignment since their trajectories are necessarily similar due to the same alignment method being used. The vertical position is reproducibly set by measuring its beam profile along the vertical axis using the fiber beam profiler (see section 4.4.2) and determining the center position of the Gaussian fit to this profile. The center can usually determined with less than $1\,\mu\mathrm{m}$ uncertainty, so the reproducibility of the overlap is mainly limited by the source alignment described in section 4.5.1. Nevertheless this gives a reasonably well defined overlap between the two beams. To find a starting point for the aforementioned overlap scan the fiber beam profiler is used for an initial approximate alignment. For this purpose the fiber is positioned in the molecular beam again, such that it cuts off the beam. The height of this cut-off is compared to the transmission through the S_y silt without the fiber. The height of the fiber is adjusted such that the maximum of this transmission and the midpoint of the cut-off are at approximately the same height. The grating laser position is then adjusted such that the maximum power is couped into the fiber tip. This alignment procedure only gives a rough starting point for the overlap scan, it is by itself not accurate enough for a variety of reasons. The adjustment of the cut-off to the S_y transmission is done "by eye" and is not reproducible on the scale of the laser waist. Additionally the location where the maximum light is coupled into the fiber might not be at the very tip of the fiber depending on how the fiber tip was prepared.

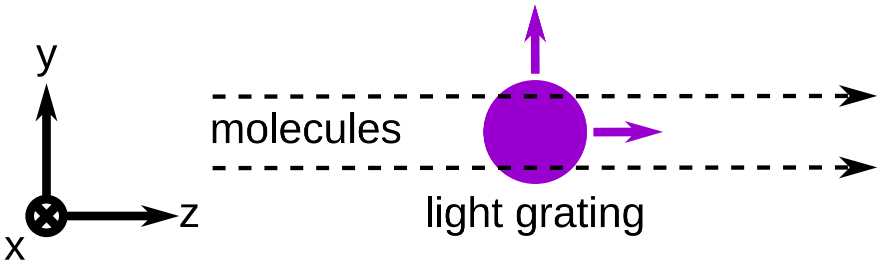

Figure 4.25: Alignment of the laser to the molecular beam in the y-z-plane. The figure shows a side view of the experiment. The light grating must be aligned vertically (along the y-axis) to overlap with the trajectories of the molecules. The alignment along the z-axis is not as critical.

4.6. Fluorescence microscopy detection

The detection end of the interferometer consists of a $160\,\mu\mathrm{m}$ thick quartz window as sketched in figure 4.2. The probability density of finding a molecule at a certain position on this window is defined by the wavefunction according to Borns rule [239]. We thus want to measure the relative distribution of the molecules arriving at the detection window. In this experiment a wide-field fluorescence microscopy setup, introduced in [120] is used to directly image the molecule distribution.

The physical principles of fluorescence have already been reviewed in section 3.2.1. For the imaging setup used in this experiment even phosphorescence lifetimes can be considered "short" due to the long illumination times. Our detection scheme thus does not actually differentiate between fluorescence and phosphorescence. Both phenomena are sometimes collectively termed (photo-)luminescence [174, 177].

4.6.1. Detection setup

To detect the molecules in this experiment we use wide field fluorescence microscopy, i.e. essentially the entire field of view of our microscope is illuminated with light of the excitation wavelength. As illustrated in figure 4.26 the illumination occurs from the side of the quartz window opposite to the camera at a grazing angle. This is dia-illumination like scheme is usually not used in conventional fluorescence microscopes in favor of an epifluorescence setup. The later design reduces the danger of accidentally sending excitation light into the eyes of the experimentators when viewing the samples directly [174, 178]. In our case this is not necessary as the fluorescence signal is not directly observed but instead imaged by a camera. Additionally the grazing angle of the illumination suffices to prevent excitation light from entering the objective. A complete overview of the detection setup is sketched in figure 4.26. The overall setup has been used in several previous experiments already [1, 2, 120, 240]. The excitation light is chosen according to the absorption spectrum of the molecule used in the experiment. Table 4 contains a list of the excitation wavelengths used for the data presented in this work.

Red $661\,\mathrm{nm}$ excitation light is provided by a diode laser and sent through a narrow band filter (filter 1). A spatial light modulator (SLM) is used to generate a flattop profile at the detection region to ensure homogeneous illumination. As shown in figure 4.26 the diode laser passes a mode cleaning stage formed by the pinhole P and lenses L1 ($f = 50\,\mathrm{mm}$) and L2 ($f = 150\,\mathrm{mm}$) before reaching the SLM. A diffuser is added in the beam path to prevent speckles from occurring in the final image. Lenses L3 ($f = 400\,\mathrm{mm}$), L4 ($f = 500\,\mathrm{mm}$) and L5 ($f = 100\,\mathrm{mm}$) image the flattop to the detection window at the end of the detection chamber. The shutter S is controlled directly by the camera software to only illuminate the molecules while taking an image. For the UV $266\,\mathrm{nm}$ illumination the emission from the frequency doubler mentioned in section 4.4 is diverted at PBS 2 in figure 4.10 and sent directly to the detection window instead of to the beamdump BD 2. $421\,\mathrm{nm}$ light is provided by the same laser, which was used for the initial alignment described earlier. A diffuser is also added in these two cases. We do not introduce additional beam shaping for the $266\,\mathrm{nm}$ and $421\,\mathrm{nm}$ illumination as higher powers and spot sizes were available in this case.

The fluorescence light emitted by the molecules is imaged using a 20x EC *Zeiss Plan-Neofluar* objective (NA $= 0.5$). For $266\,\mathrm{nm}$ and $421\,\mathrm{nm}$ illumination a long working distance objective (20x LD Plan-Neofluar, NA $= 0.4$) is used to mitigate background light originating from fluorescence of the objective glass itself in case UV light enters it. As sketched in figure 4.26 the molecules are imaged onto an *IXON DV885KCS-VP CCD camera* using lens L6 ($f = 164\,\mathrm{mm}$). The light passes through a fluorescence filter (filter 2), which removes any light at the excitation wavelength from the picture. The particular choices of filters according to the emission wavelengths of the used molecules can be found in table 4. Information about the detection setup used here is also available in the supplementary materials of [120].

To calibrate the exact magnification of the detection setup a *Thorlabs R1L3S3* calibration grid is imaged. It is found this way that the size of one pixel in the images recorded corresponds to approximately $0.33\,\mu\mathrm{m}$ for both 20x objectives (see (C.1) and (C.3)). More details on this calibration can be found in appendix C. In principle the imaging setup used here can be used to localize individual molecules to $\sim 10\,\mathrm{nm}$ using a technique relying on the same principles as single-molecule high-resolution imaging with photobleaching (SHRIMP) [120, 241]. Since information of individual molecule positions is not relevant here, we do not make use of any further steps to carry out this localization. Nevertheless, the pointspread functions of isolated molecules can be seen on some of the images recorded here demonstrating the effective single-molecule resolution.

In order to remove the molecules from the quartz surface and to prepare it for a new measurement plasma cleaning as described in [120] is used. For this purpose the pressure in the detection chamber is raised to $1 - 4\,\mathrm{mbar}$ by letting a controlled amount of air into the chamber via a needle valve. An electrode formed by a conventional razor blade is brought into close proximity of the outside surface of the quartz window. A voltage of $1.5\,\mathrm{kV}$ AC at $10\,\mathrm{kHz}$ is then applied to the electrode, which ignites the plasma within the chamber. The ground contact is formed by the vacuum chamber itself. After several seconds the plasma has removed the fluorescent molecules from the quartz surface and it is ready for the next measurement.

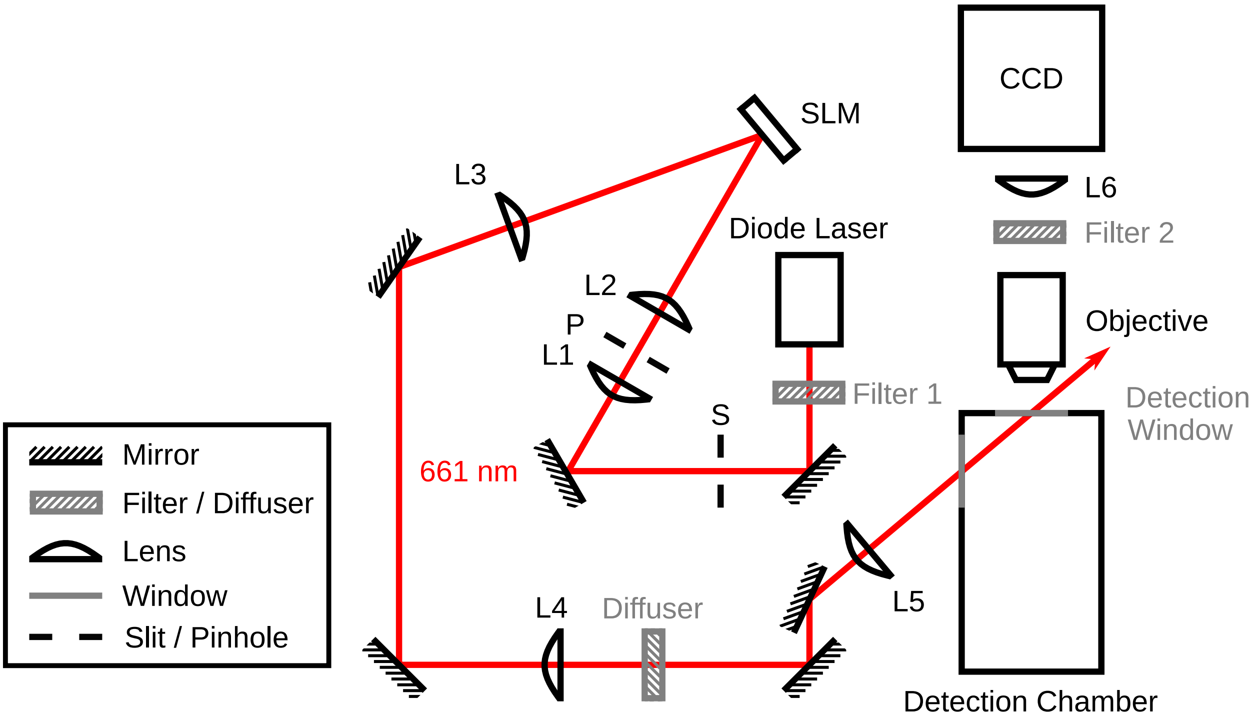

Figure 4.26: Overview of the detection optics for $661\,\mathrm{nm}$ illumination. Light emitted by the diode laser passes the shutter S and goes through a mode cleaning stage formed by lenses L1, L2 and pinhole P. The light is reflected of a SLM creating flattop illumination at the detection window. The fluorescent light emitted by the molecules on the window is imaged through filter 2 onto an CCD camera.

molecule	abs. max. λ_{max} (nm)	emis. max. λ_{em} (nm)	excitation λ_{ex} (nm)	filter trans. (nm)	Ref.
H_2-phthalocyanine	686	690	661	711/25 BP	[242, 243]
meso-tetraphenylporphyrin	403	653, 720	421	650/40 BP	[244, 245]
dihydroxy-naphthacenedione	265^{a}	527, 565, 600^{a}	266	550/88 BP	[243]
photocleavable Zn-phthalocyanine	678^{b}	690^{c}	661	692/40 BP	see sec. 4.7.4

Table 4: Summary of absorption maxima λ_{max}, fluorescence emission maxima λ_{em} and the detection parameters used for the different molecules. When available spectral data taken in the vapor phase is stated for λ_{max} and λ_{em}. The following solvents were used for data taken in solution: ^{a} MeOH, ^{b} Dioxane, ^{c} THF. λ_{ex} is the wavelength used to excite the fluorescence for the detection in our setup. The band pass (BP) filter used in each case is given as well.

4.7. Selection of molecules

The experimental parameters described in the previous sections put some constraints on which molecules can be used in the setup. The molecules are required to be thermally stable enough such that the source leaves them intact (see section 4.2). The detection scheme used here (see section 4.6) also requires them to be fluorescent. The physical dimensions of the apparatus and the period of the grating used restrict the mass of the molecules to be $m \lesssim 1500\,\mathrm{u}$ in order to be able to resolve individual diffraction peaks. In order to study the effects of UV optical gratings it is naturally desirable that the molecules also show some significant interaction with light of this wavelength. In the following we present the selection of molecules which are used in the experiments presented here. These organic molecules fulfill the aforementioned experimental requirements and show combination of different optical behaviours. A summary of the typical velocities and de Broglie wavelenghts of the molecules is also given in table 2. Spectral data relevant to the detection is collected in table 4.

4.7.1. H_2-phthalocyanine

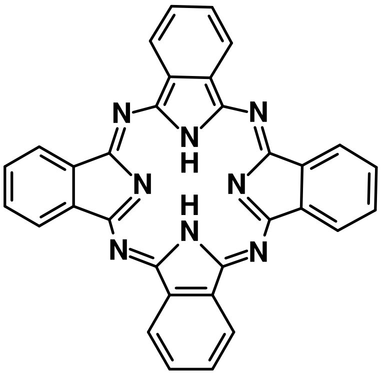

Figure 4.27: Structure of phthalocyanine $C_{32}H_{18}N_8$ (PcH_2)

Phthalocyanine $C_{32}H_{18}N_8$ (PcH_2) is a dye molecule which has established itself as a prototypical molecule to be used in different variants of the far-field setup because of its good compatibility with the source and detection [1, 2, 120]. Its mass is $m = 514.5\,\mathrm{u}$ is also in the ideal range. The structure of PcH_2 is shown in figure 4.27. In the ground state it has D_{2h} symmetry and consequently no electric dipole moment [246]. Phthalocyanine is thermally very stable and can be easily evaporated, which is ideal for the effusive source used here. At a typical oven body temperatures T_B in the range of $400-420\,^{\circ}\mathrm{C}$ the vapor pressure of PcH_2 is at the order of $1-3\,\mathrm{Pa}$ [247].

PcH_2 and its derivatives are known for their intense blue - green coloration. This is due to their strong absorption usually in the spectral region around $660\,\mathrm{nm}$ [248]. The limited solubility of the metal free phthalocyanine PcH_2 in the appropriate solvents makes it challenging to record UV-Vis absorption spectra even in solution. However, vapor phase UV spectra have been reported [242, 243, 249]. While not providing absolute numbers for the absorption cross-section, this data clearly shows that in addition to strong absorption peaks at $623\,\mathrm{nm}$ and $\sim 686\,\mathrm{nm}$ (Q-bands) PcH_2 also shows strong absorption in the UV region from $\sim 340\,\mathrm{nm}$ (Soret-band) to below $200\,\mathrm{nm}$. Moreover, PcH_2 is known to fluoresce both in solution [250, 251] and in the gas phase [243]. In the latter case the fluorescence emission has its maximum also at $\sim 690\,\mathrm{nm}$.

From the vapor phase spectrum in [242] we estimate the absorption at $266\,\mathrm{nm}$ to be ~ 0.46 of the maximum at $690\,\mathrm{nm}$. To find an estimate of the absolute absorption cross-section at this wavelength we compare this with spectra taken in solution (1-Chloronaphthalene). The extinction coefficient at the $698\,\mathrm{nm}$ maximum has been determined as $\epsilon_{698\,\mathrm{nm}} = 1.62 \cdot 10^5\,\mathrm{mol}^{-1}\,\mathrm{cm}^{-1}$ [252]. Note that the Q-band maxima are slightly red shifted in solution compared to vapor measurements [242]. From this extinction coefficient we approximate the absorption cross-section [172] at $266\,\mathrm{nm}$ to be $\sigma_{266\,\mathrm{nm}} \approx 2.8 \cdot 10^{-20}\,\mathrm{m}^2$. This value should only be understood as a rough estimate as it neglects the differences between the absorption in vapor and solution. The solution extinction coefficient at $698\,\mathrm{nm}$ we used might also be modified by the solvent compared to the absolute value in the gas phase. Additionally the spectrum of PcH_2 given in [242] was recorded in two separate runs, which prevents an accurate comparison of the absorption in the UV with the Q-bands. Nevertheless it should give us at least a rough estimate on the order of magnitude for σ.

Measurements of the optical polarizability at $266\,\mathrm{nm}$ are not readily available. Computations reported in [253] give $\bar{\alpha} \approx 4\pi\varepsilon_0 \cdot 101\,\mathrm{\AA}^3$ for the polarizability in the high-frequency limit, which differs only slightly from the static value $\bar{\alpha}_{\mathsf{stat}} \approx 4\pi\varepsilon_0 \cdot 98.6\,\mathrm{\AA}^3$. However, because the spectrum suggests that we are not far from resonances these values might differ significantly from the actual value at $266\,\mathrm{nm}$. For example DFT calculations using the PPBE0 method yielded a dynamic polarizability of $\bar{\alpha}_{266\,\mathrm{nm}} = -8.3\,\mathrm{\AA}^3 \cdot 4\pi\varepsilon_0$ at this wavelength [254], which differs significantly from the previously cited values. However, there is also some dispersion in the results for different computations methods, which is why this number might also have limited applicability.

4.7.2. Meso-tetraphenylporphyrin

PcH_2 discussed in the previous section is structurally very similar to the porphyrins. However, their spectral properties, can differ significantly [249]. The specific porphyrin we are investigating here is metal free tetraphenylporphyrin $C_{44}H_{30}N_4$ (TPP), which has a mass of $m = 614.7\,\mathrm{u}$. Its structure is shown in figure 4.28, like PcH_2 it has D_{2h} symmetry [255]. At the usual temperatures ($T_B \sim 370\,^\circ\mathrm{C}$) the vapor pressure of TPP is of the same order as for PcH_2 ($\sim 2\,\mathrm{Pa}$) [256, 257].

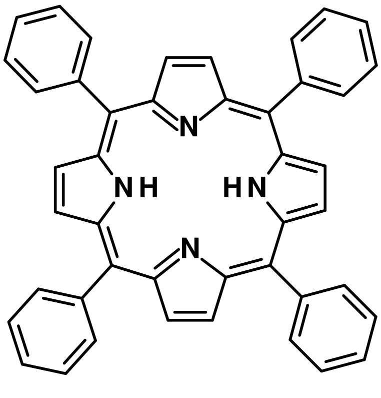

Figure 4.28: Structure of tetraphenylporphyrin $C_{44}H_{30}N_4$ (TPP)

The vapor absorption spectrum of TPP shows a very intense peak (Soret-band) at $403\,\mathrm{nm}$, more than one order of magnitude larger than the absorption at other wavelengths in the UV-Vis retion. In solution this peak is red-shifted by about $20\,\mathrm{nm}$. For a toluene solution the maximum extinction coefficient was measured as $\epsilon_{419\,\mathrm{nm}} = 4.43 \cdot 10^5\,\mathrm{mol}^{-1}\,\mathrm{cm}^{-1}$ (corresponds to $\sigma_{419\,\mathrm{nm}} = 1.7 \cdot 10^{-19}\,\mathrm{m}^2$) [244, 258, 259]. At $266\,\mathrm{nm}$, which is the wavelength relevant for this experiment, the absorption is significantly lower.

We estimate from [244] that in the gas phase it is approximately $12~\%$ of the maximum at $400\,\mathrm{nm}$. This gives us the estimate $\sigma_{266\,\mathrm{nm}} \approx 2 \cdot 10^{-20}\,\mathrm{m}^2$. Again this is only a rough approximation since we are comparing spectra in vapor and solution. TPP also exhibits fluorescence with emission maxima in solution at $653\,\mathrm{nm}$ and $720\,\mathrm{nm}$ [245, 250]. While data for the dynamic porlarizability of TPP is not readily available, there have been measurements for the static polarizability in the gas phase via deflection near-field matter-wave interferometry [260]. This static value $\bar{\alpha}_{\mathsf{stat}} \approx 4\pi\varepsilon_0 \cdot 105\,\text{Å}^3$ is similar to the one of PcH_2. However, again the dynamical polarizability at $266\,\mathrm{nm}$ might differ significantly from this number.

4.7.3. 6,11-dihydroxy-5,12-naphthacenedione

Dihydroxy-naphthacenedione is a derivative of tetracene with a mass of $m = 290.3\,\mathrm{u}$. Similar to the previous molecules, vapor pressures for these dihydroxy-naphthacenedione are at the order of $\sim 3\,\mathrm{Pa}$ for the temperatures relevant in this experiment ($T_\mathsf{B} \approx 220\,^\circ\mathrm{C}$) [261]. The basic structure of dihydroxy-naphthacenedione sketched in figure 4.29 suggests that this molecule has C_{2v} symmetry. However, the formation of intramolecular hydrogen bridges between the neighbouring functional groups may raise the symmetry to D_{2h} [262, 263]. Comparison with spectra of molecules where this hydrogen bonding is blocked reported in [264] indicates that this also has a significant influence on the spectral properties of the molecules. Dihydroxy-naphthacenedione has absorption maxima in the region around $500\,\mathrm{nm}$, which are not present at these wavelengths in the modified molecules. The UV wavelength investigated in the experiment presented here ($266\,\mathrm{nm}$) lies almost exactly at another absorption maximum of dihydroxy-naphthacenedione. Measurements of the extinction coefficient at this peak and also the spectra overall show a strong dependence on the solvent used. Values for the extinction coefficient vary from $\epsilon_{266\,\mathrm{nm}} \approx 4.1 \cdot 10^4\,\mathrm{mol}^{-1}\,\mathrm{cm}^{-1}$ to $\epsilon_{266\,\mathrm{nm}} \approx 1.8 \cdot 10^5\,\mathrm{mol}^{-1}\,\mathrm{cm}^{-1}$ [263]. This gives us an estimate of $1.6 \cdot 10^{-20}\,\mathrm{m}^2 - 7 \cdot 10^{-20}\,\mathrm{m}^2$ for the absorption cross-section $\sigma_{266\,\mathrm{nm}}$ [172], however because of this strong solvent-dependence the applicability of these numbers to our experiment is most likely limited. The reason for the influence of the solvent lies in the formation of hydrogen bonds between dihydroxy-naphthacenedione molecules (formation of dimers) and between the molecules and the solvent itself. Because of this the individual molecules may take on different structures in solution depending on the nature of the solvent [263]. Dihyrdroxy-naphthacenedione also shows fluorescence emission in the region of $560 - 580\,\mathrm{nm}$ when excited with $270\,\mathrm{nm}$ [263, 264]. Polarizability data for dihydroxy-naphthacenedione is not readily available. DFT calculations suggest a dynamic polarizability of $\bar{\alpha}_{266\,\mathrm{nm}} = 4\pi\varepsilon_0 \cdot 43\,\text{Å}^3$ and a slightly smaller static value of $\bar{\alpha}_{\mathsf{stat}} = 4\pi\varepsilon_0 \cdot 34\,\text{Å}^3$ [265].

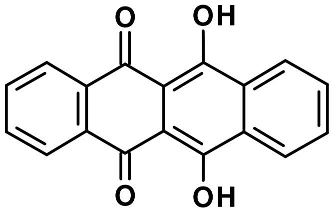

Figure 4.29: Structure of 6,11-dihydroxy-5,12-naphthacenedione

4.7.4. Zn-phthalocyanine with photocleavable tags

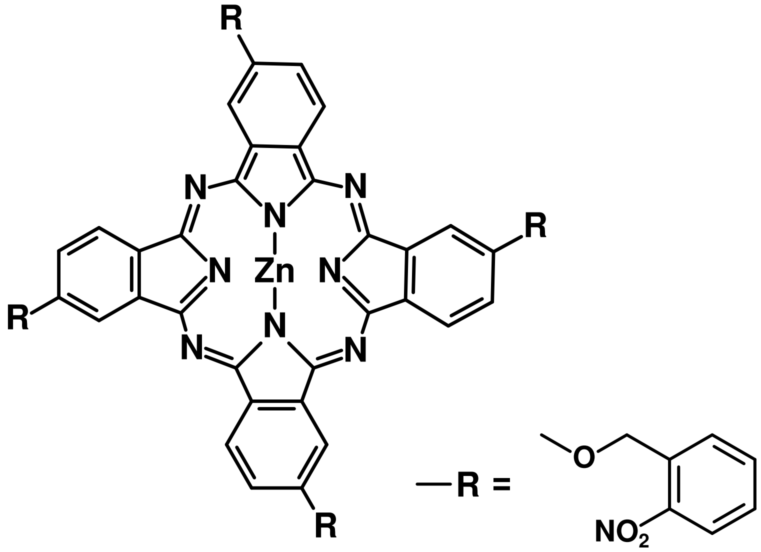

Figure 4.30: Structure of Zn-phthalocyanine with photocleavable tags ($-$R)

The molecules shown in figure 4.30 consist of a Zn-phthalocyanine with four functional groups ($-$R in figure 4.30). As already mentioned in section 3.2.2 these nitrobenzyl groups are designed to cleave off after absroption at our target wavelength of $266\,\mathrm{nm}$. The molecular samples were synthesised by our collaborator Alfredo Di Silvestro (University of Basel) for this purpose. Because of the additional functional groups and the metal ion the mass $m = 1182.4\,\mathrm{u}$ of these photocleavable molecules is more than twice the mass of PcH$_2$. We expect that molecules which undergo photocleavage are effectively lost for the purposes of our experiment. Either because the recoil from the leaving group kicks the rest of the molecule out of the beam far enough to not reach the detection at all, or because the random directions of the recoils yield an even distribution of molecules as a background in the detection. If the cleavage process leaves the remaining part of the molecule as an ion, stray electric fields might also deflect it out of the beam.

Absorption spectra of the photocleavable Zn-phthalocyanines have been recorded in different solvents as shown in figure 4.31 [266]. The basic structure of the spectrum is very similar to the vapor phase spectra recorded for PcH$_2$ and Zn-phthalocyanine [243]. In particular both the Soret-band at $\sim 340\,\mathrm{nm}$ and the Q-bands in the $600 - 700\,\mathrm{nm}$ region are also present. Similar to PcH$_2$ the Zn-phthalocyanines with photocleavable tags also show fluorescence emission with a maximum at $\sim 690\,\mathrm{nm}$. Test the thermal stability of the molecules and the photocleavable tags, they were evaporated directly on a glass slide and subsequently analysed via mass spectrometry. This confirmed that the molecules stay intact during evaporations and that the tags do not already cleave off prematurely [267].

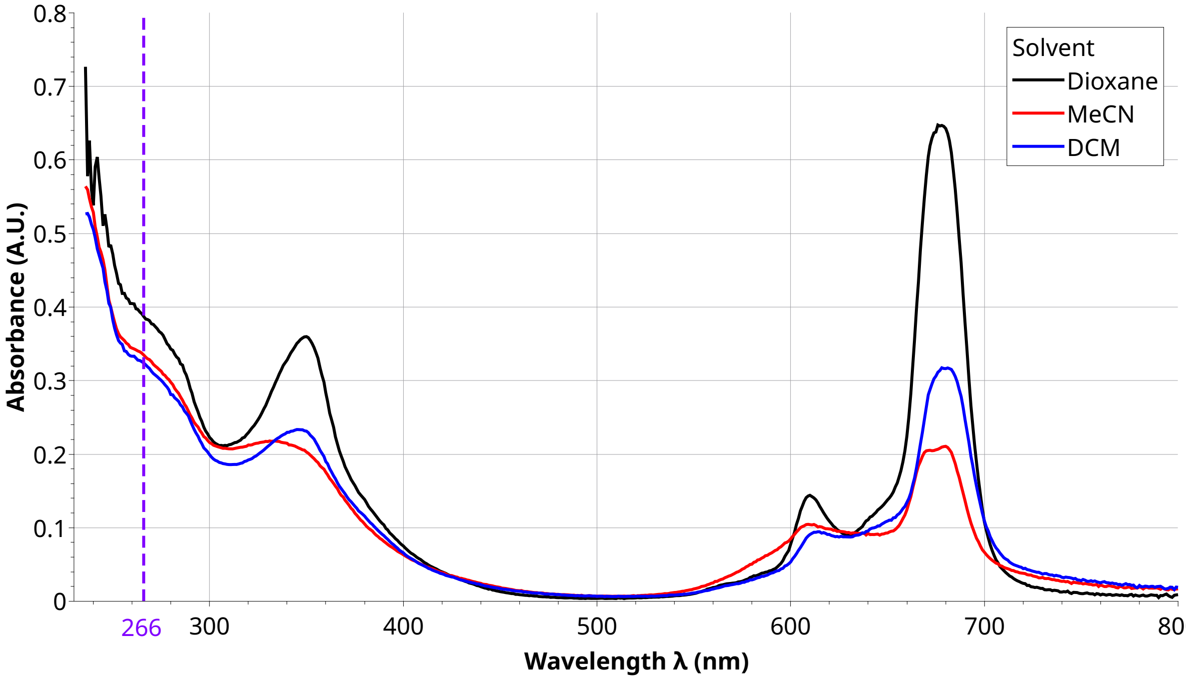

Figure 4.31: UV-Vis absorption spectra of Zn-phthalocyanine with photocleavable tags in different solvents [266].

5. Theoretical description

In the previous section we have extensively discussed the technical realization of the experiment as well as the roles of the various components. In this section we want to model this setup theoretically. Our model used the Wigner formalism, which we will introduce in section 5.1. The following sections will cover the description of the components of the experiment in this formalism. This allows us to write down a slightly simplified model for computing the diffraction patterns we expect to see in the experiment, which is given in section 5.4.

5.1. Wigner formalism

5.1.1. Introduction

For a variety of reasons it is convenient to describe the propagation of the molecular matter waves in our experiment using a phase space formalism. The Wigner quasi-probability distribution in particular has been established as a very useful framework for analyzing matter wave interferometers, predominantly in the near-field. The main advantages lie in the easy comparison to classical phase space distributions as the two coincide for incoherent mixtures. This is useful for the experimental setup used here as we can thus more easily incorporate the initial thermal distribution of the molecules. As we will see shortly the Wigner formalism also has the benefit of a nearly trivial description of free propagation [128, 219, 268].

The Wigner function is a concept commonly used in quantum optics. For a given density matrix $\hat{\rho}$, which in general describes a mixed state, the Wigner function is defined as [269, 270]

$$w(\mathbf{x},\mathbf{p}) = \frac{1}{(2\pi\hbar)^d}\int_{\mathbb{R}^d} \mathrm{d}^d s \;\exp\left\{i\frac{\mathbf{p}\cdot\mathbf{s}}{\hbar}\right\}\left\langle \mathbf{x}-\frac{\mathbf{s}}{2}\right|\hat{\rho}\left|\mathbf{x}+\frac{\mathbf{s}}{2}\right\rangle \tag{5.1}$$

$d = 1, 2, 3$ denotes the number of spatial dimensions. The parameters $\mathbf{x}$ and $\mathbf{p}$ correspond to the classical position and momentum forming the phase space (for light these might be the quadratures). The Wigner function has a number of interesting properties. Most notably it is real and normalized, i.e. its integral over all $\mathbf{x}$ and $\mathbf{p}$ is unity, and it can take on negative values. The latter is what makes it a *quasi*-probability distribution. This is compatible with the fact that the Wigner function gives an alternate way of expressing a quantum state $\hat{\rho}$ and we thus cannot interpret it as a probability distribution directly. The relation to measurable probabilities is given by the marginals of the Wigner function. The probability distribution in position space, which corresponds to the measured intensity in our experiment, is given by the integral over $\mathbf{p}$ [268, 269]:

$$w(x) = \int_{\mathbb{R}^d} \mathrm{d}^d p \; w(\mathbf{x},\mathbf{p}) \tag{5.2}$$

An analogous relation holds for the probability distribution in momentum space. It will be useful to define the characteristic function $\chi(s,q)$ as the two dimensional Fourier transform of the Wigner function [217, 270]:

$$\chi(\mathbf{s},\mathbf{q}) = \iint_{\mathbb{R}^d} \mathrm{d}^d x \; \mathrm{d}^d p \;\exp\left\{i\frac{\mathbf{q}\cdot\mathbf{x}-\mathbf{s}\cdot\mathbf{p}}{\hbar}\right\} w(\mathbf{x},\mathbf{p}) \tag{5.3}$$

The normalization of the Wigner function requires the property $\chi(0,0) = 0$. The probability density in position space (5.2) can be expressed as the Fourier transform of the characteristic function for $s = 0$:

$$w(x) = \frac{1}{(2\pi\hbar)^d}\int_{\mathbb{R}^d} \mathrm{d}^d q \;\exp\left\{-i\frac{\mathbf{q}\cdot\mathbf{x}}{\hbar}\right\}\chi(0,\mathbf{q}) \tag{5.4}$$

5.1.2. Dynamics in the Wigner formalism

Most generally the time evolution of the Wigner function in the presence of an external potential $U(\mathbf{x})$ is governed by the quantum Liouville equation [268, 269]:

$$\left(\frac{\partial}{\partial t}+\frac{\mathbf{p}}{m}\cdot\nabla_{\mathbf{x}}\right) w_t\left(\mathbf{x},\mathbf{p}\right) = \sum_{l=0}^{\infty}\frac{(-1)^l\hbar^{2l}}{2^{2l}(2l+1)!}\left(\nabla_{\mathbf{x}}^{2l+1}U(\mathbf{x})\right)\cdot\left(\nabla_{\mathbf{p}}^{2l+1}w_t\left(\mathbf{x},\mathbf{p}\right)\right) \tag{5.5}$$

A very useful property of (5.5) is that it is identical to the classical Liouville equation for potentials that are at most quadratic in $\mathbf{x}$. As a consequence of that the free evolution subject to the gravitational potential $U(\mathbf{x}) = mgy$ (where $\mathbf{x} = (x,y,z)^\mathsf{T}$ with the axes defined in figure 4.2) can be described entirely classically. The Wigner function is thus simply changed by a shearing transformation [217, 268, 269]

$$w_{t+\Delta t}\left(\mathbf{x},\mathbf{p}\right) = w_t\left(\mathbf{x}-\frac{\mathbf{p}\Delta t}{m}+\frac{\mathbf{g}\Delta t^2}{2},\mathbf{p}-\mathbf{g}m\Delta t\right) \tag{5.6}$$

Here $\mathbf{g} = (0,-g,0)^\mathsf{T}$ is the gravitational acceleration. Note that the negative sign in the $\mathbf{g}$ term in the first argument is a consequence of the fact that $\mathbf{p}$ is the *final* momentum. The coordinate axes are defined as shown in figure 4.2. For the strong collimation present in our experiment, the forward momentum p_z is typically much larger than any deflection in the transverse direction. Because of this we can assume the forward momentum to stay constant throughout the experiment. It is thus convenient to reparametrize $w_t(\mathbf{x},\mathbf{p})$ in terms of the z position instead of time t [205, 217]. We may then write the transformation (5.6) as

$$w_{z+\Delta z}\left(\mathbf{x},\mathbf{p}\right) = w_z\left(\mathbf{x}-\frac{\mathbf{p}\Delta z}{p_z}+\frac{\mathbf{g}m^2\Delta z^2}{2p_z^2},\mathbf{p}-\frac{\mathbf{g}m^2\Delta z}{p_z}\right) \tag{5.7}$$

Here and from now on we write the z position instead of the time dependence in the subscript of the Wigner function. $\mathbf{x}$ and $\mathbf{p}$ in (5.7) are now two dimensional vectors ($d=2$) describing the position and momentum in the transverse x-y-plane. The free evolution of the characteristic function (5.3) is also a shearing transformation, the gravitational potential yields an additional phase factor [217]

$$\chi_{z+\Delta z}\left(\mathbf{s},\mathbf{q}\right) = \exp\left\{i\frac{\mathbf{g}m^2\Delta z}{\hbar p_z}\cdot\left(\frac{\mathbf{q}\Delta z}{2p_z}-\mathbf{s}\right)\right\}\cdot\chi_z\left(\mathbf{s}-\frac{\mathbf{q}\Delta z}{p_z},\mathbf{q}\right) \tag{5.8}$$

To describe the interaction of the Wigner function with some transmissive mask (e.g. a grating or collimator) it is useful to apply the eikonal approximation. Effectively this means that we neglect the transversal shift during the propagation through the interaction potential $U(x)$. In (5.5) the positional derivative of the Wigner function on the left hand side may then be disregarded [217]. The solution for the transformation of the Wigner function is then found to be given by a convolution [205, 219, 270]

$$w_{z'}(\mathbf{x},\mathbf{p}) = \int_{\mathbb{R}^2}\mathrm{d}^2\widetilde{\mathbf{p}}\ w_z(\mathbf{x},\widetilde{\mathbf{p}})T\left(\mathbf{x},\mathbf{p}-\widetilde{\mathbf{p}}\right) \tag{5.9}$$

with the transmission kernel

$$T(\mathbf{x},\mathbf{p}) = \frac{1}{(2\pi\hbar)^2}\int_{\mathbb{R}^2}\mathrm{d}^2s\ \exp\left\{i\frac{\mathbf{p}\cdot\mathbf{s}}{\hbar}\right\}t\left(\mathbf{x}-\frac{\mathbf{s}}{2}\right)t^*\left(\mathbf{x}+\frac{\mathbf{s}}{2}\right) \tag{5.10}$$

The function $t(\mathbf{x})$ appearing in (5.10) is the transmission function. This is the multiplicative factor which would appear in front of the wavefunction $\psi(\mathbf{x})$ for a pure state. In the eikonal approximation the transmission function has the form [217, 268]

$$t(\mathbf{x}) = t_0(\mathbf{x})\cdot e^{i\phi(\mathbf{x})} \tag{5.11}$$

$t_0(\mathbf{x}) = |t(\mathbf{x})|$ describes the absorptive effect of the mask. E.g. it is zero for the parts of a collimator or material grating where the molecules are blocked. Similarly it describes the transmission through a light grating if molecules might be removed via absorption (see section 5.5). $\phi(\mathbf{x})$ is the eikonal phase acquired during transmission through the mask due to the interaction potential $U(x)$. It is given by

$$\begin{aligned}\phi(\mathbf{x}) &= -\frac{1}{\hbar}\int_t^{t+\Delta t}\mathrm{d}t\ U(\mathbf{x}(t))\\ &= -\frac{m}{\hbar p_z}\int_z^{z'}\mathrm{d}z\ U(x,y,z)\end{aligned} \tag{5.12}$$

Here we applied the aforementioned reparametrization $t\to z$. We will discuss in section 5.5 how the potential $U(\mathbf{x})$ looks for light gratings. Note that since (5.11) is in general not unity due to its absorptive part $t_0(\mathbf{x})$, (5.9) does not preserve the normalization of the Wigner function. Since only relative probabilities will be relevant in the end we will disregard the normalization factors for now and only renormalize the Wigner function at the end of our calculations [219].

5.2. Grating transformation

Let us assume that our grating is periodic in the x-coordinate with period d. The same is then true for the transmission function (5.11) and thus also for the transmission kernel (5.10). Both may then written as Fourier series. It is convenient for our calculations to write this Fourier series for the transmission kernel in the form [217, 270]

$$T(\mathbf{x},\mathbf{p}) = \frac{1}{(2\pi\hbar)^2}\sum_{n\in\mathbb{Z}} \exp\left\{i\frac{2\pi x}{d}n\right\}\int_{\mathbb{R}^2} \mathrm{d}^2 s\ \exp\left\{i\frac{\mathbf{p}\cdot\mathbf{s}}{\hbar}\right\} B_n\left(\frac{s_x}{d}, s_y, y\right) \tag{5.13}$$

We only apply the Fourier series to the x-component of $\mathbf{x}$ and keep the y-dependence explicit because we only assume that the grating is periodic along this one axis. Note that $\mathbf{s} = (s_x, s_y)^{\mathsf{T}}$. The coefficients $B_n\left(\frac{s_x}{d}, s_y, y\right)$ are called *Talbot coefficients*. They are in fact just the Fourier transforms in $\mathbf{p}$ space of the Fourier coefficients of $T(\mathbf{x},\mathbf{p})$ in x-space. They are also directly related to the Fourier coefficients of the transmission function $t(\mathbf{x})$. We will discuss how these coefficients look like for a light grating like the one used in the experiment in section 5.5.

For now we will just assume them to be given parameters. To see how to apply this notation we first note that we can write an analogous expression to (5.9) for the characteristic function (5.3) [217]:

$$\chi_{z'}(\mathbf{s},\mathbf{q}) = \int_{\mathbb{R}^2} \mathrm{d}^2\widetilde{\mathbf{q}}\ \chi_z(\mathbf{s},\widetilde{\mathbf{q}}) T_\chi\left(\mathbf{s},\mathbf{q}-\widetilde{\mathbf{q}}\right) \tag{5.14}$$

Here we introduced the function

$$\begin{aligned} T_\chi\left(\mathbf{s},\mathbf{q}\right) &= \frac{1}{(2\pi\hbar)^2}\iint_{\mathbb{R}^2} \mathrm{d}^2 x\ \mathrm{d}^2 p\ \exp\left\{i\frac{\mathbf{q}\cdot\mathbf{x}-\mathbf{s}\cdot\mathbf{p}}{\hbar}\right\} T(\mathbf{x},\mathbf{p}) \\ &= \frac{1}{2\pi\hbar}\sum_{n\in\mathbb{Z}}\int_{\mathbb{R}} \mathrm{d}y\ \exp\left\{i\frac{q_y y}{\hbar}\right\}\cdot\delta\left(q_x + \frac{2\pi\hbar}{d}n\right)\cdot B_n\left(\frac{s_x}{d}, s_y, y\right) \end{aligned} \tag{5.15}$$

in analogy to (5.3). The second line of (5.15) is derived by inserting (5.13). $\delta(x)$ is the Dirac delta distribution and $\mathbf{q} = (q_x, q_y)^{\mathsf{T}}$ was split up into components. If we insert (5.15) into (5.14) we arrive at

$$\chi_{z'}(\mathbf{s},\mathbf{q}) = \frac{1}{2\pi\hbar}\sum_{n\in\mathbb{Z}}\iint_{\mathbb{R}} \mathrm{d}y\ \mathrm{d}\widetilde{q}_y\ \chi_z\left(\mathbf{s}, q_x + \frac{2\pi\hbar}{d}n, \widetilde{q}_y\right)\cdot\exp\left\{i\frac{(q_y-\widetilde{q}_y)\,y}{\hbar}\right\}\cdot B_n\left(\frac{s_x}{d}, s_y, y\right) \tag{5.16}$$

Equation (5.16) simplifies significantly for the case where the Talbot coefficients are independent of y, as would be the case for an infinitely tall grating. In this case we are left with [217]

$$\chi_{z'}(\mathbf{s},\mathbf{q}) = \sum_{n\in\mathbb{Z}} \chi_z\left(\mathbf{s}, q_x + \frac{2\pi\hbar}{d}n, q_y\right)\cdot B_n\left(\frac{s_x}{d}, s_y\right) \tag{5.17}$$

The problem essentially becomes one-dimensional and the Talbot coefficients appear as multiplicative factors. Unfortunately the light grating used in our experiment is collimated very tightly and we will therefore certainly have an explicit y-dependence. We may however under certain conditions neglect the s_y dependence of $B_n\left(\frac{s_x}{d}, s_y, y\right)$. Recall that the characteristic function (5.3) is the Fourier transform of the Wigner function. An incoherent initial state corresponds to a Wigner function which occupies a large area in phase space, in the limit of a complete mixture it is constant over all of phase space [217, 270]. The characteristic function of such an incoherent state will thus only have a small extend around zero, in the limit of a constant Wigner function it is given by a Dirac delta distribution. In our experiment there is no collimation in the y direction in front of the grating. Because of this we will assume that the distribution of the momentum in the y-direction p_y is still sufficiently incoherent at the grating that we can approximate the s_y dependence of $\chi_{z'}(\mathbf{s},\mathbf{q})$ as

$$\chi_{z'}(\mathbf{s},\mathbf{q}) \propto \delta(s_y) \tag{5.18}$$

Then only the value $s_y = 0$ is relevant for the Talbot coefficients in (5.17). I.e. we approximate that the s_y width of $\chi_{z'}(\mathbf{s},\mathbf{q})$ is narrow enough that only values of the Talbot coefficients where $s_y \approx 0$ contribute. In essence this approximation means that we neglect diffraction in the y-direction and only consider its effect in the x-direction. The Talbot coefficients $B_n\left(\frac{s_x}{d},0,y\right) \equiv B_n\left(\frac{s_x}{d},y\right)$ are simply the coefficients for a one-dimensional grating with y as an additional parameter. For a transmission function of the form (5.11) we can write them as

$$B_n(\xi,y) = \frac{1}{d}\int_{-\frac{d}{2}}^{\frac{d}{2}} \mathrm{d}x\, t_0\left(x - d\frac{\xi}{2}, y\right) t_0\left(x + d\frac{\xi}{2}, y\right) \cdot \exp\left\{-i\frac{2\pi x}{d}n + i\phi\left(x - d\frac{\xi}{2}\right) - i\phi\left(x + d\frac{\xi}{2}\right)\right\} \tag{5.19}$$

As we will see in section 5.5 this becomes more involved when we consider additional contributions from multiple photon absorptions.

5.3. Collimator transformation

A collimator can be described by a transmission function [217, 268]

$$t(\mathbf{x}) = \theta\left(\frac{D}{2} - |x|\right) \tag{5.20}$$

Here D is the full width of the collimator opening and

$$\theta(x) = \begin{cases} 1 & x \geq 0 \\ 0 & x < 0 \end{cases} \tag{5.21}$$

is the Heaviside step function. (5.20) describes a collimator in the horizontal direction, like $S_{1,x}$ and $S_{2,x}$ in this experiment. Since the generalization to other orientations is trivial we will only treat this case. Using (5.10) we can compute the transmission kernel for a collimation slit [268]:

$$T(\mathbf{x},\mathbf{p}) = \delta(p_y) \cdot \theta\left(\frac{D}{2} - |x|\right) \frac{D - 2|x|}{\pi\hbar} \operatorname{sinc}\left(\frac{p_x(D - 2|x|)}{\hbar}\right) \tag{5.22}$$

The corresponding transmission kernel for the characteristic function is found via (5.15):

$$T_\chi(\mathbf{s},\mathbf{q}) = \delta(q_y) \cdot \theta(D - |s_x|) \frac{D - |s_x|}{2\pi\hbar} \operatorname{sinc}\left(\frac{q_x(D - |s_x|)}{2\hbar}\right) \tag{5.23}$$

The sinc term in (5.22) describes the diffraction effect originating from the slit. This effect vanishes when the slit width becomes much larger than the spatial localization of the initial state, i.e. if the initial state is more incoherent. This is particularly the case if the initial state is completely incoherent and is thus described by a constant Winger function. In this case the effect of the slit can be described classically as [268]

$$w_{z'}(\mathbf{x},\mathbf{p}) = |t(\mathbf{x})|^2 \cdot w_z(\mathbf{x},\mathbf{p}) = t(\mathbf{x}) \cdot w_z(\mathbf{x},\mathbf{p}) \tag{5.24}$$

The second equality is true for the collimator transmission function (5.20). We will apply this approximation for the first collimator along each axis in our experiment, as the source will be practically incoherent before that.

Note that all transformations discussed in this section do naturally not keep the normalization of the Wigner function. As already mentioned we will ignore that for our computation and just renormalize the final result.

5.4. Wigner function description of the Far-field setup

Having introduced the necessary formalism for describing our diffraction experiment in the previous section we want to consider the explicit Wigner description here. We will start by considering an initial classical phase space distribution and sequentially apply the transformations described in section 5.2 and 5.3. In between we will freely evolve the Wigner function as outlined in section 5.1.2. The computation steps thus follow the propagation sketched in figure 4.2. We treat the problem as two-dimensional. I.e. we only include the x and y coordinates in our Wigner description and take the z coordinate as the parameter for the evolution of the Wigner function instead of time as explained in section 5.1.2. The computation is carried out for a fixed $p_z = mv_z$. We include the thermal distribution of molecules with a particular velocity per unit time by integrating the final intensity pattern over (4.3) at the end. In order to obtain an analytical result some additional approximations are necessary:

- The first collimators along each axis ($S_{1,x}$ and S_y) are treated classically according to (5.24) as their is no significance coherence before collimation.

- We approximate the initial transversal momentum distribution $\mu_x(p_x)$ as constant. This is justified by the fact that parts of the beam which deviate far enough from straight trajectories such that the angle dependence of the source becomes relevant are cut off by e.g. the skimmers between the vacuum chambers anyway.

- As discussed in section 5.2 we will neglect any dependence of the Talbot coefficients on the parameter s_y but will explicitly keep the y dependence.

Carrying out the computation yields the following result for the flux at the detector [271]:

$$\begin{aligned}
j\left(\mathbf{x}\right) = \sum_{n\in\mathbb{Z}} \int_{\mathbb{R}^+} \mathrm{d}p_z \iint_{\mathbb{R}} \mathrm{d}q_x\ \mathrm{d}p_y\ \Bigg[& \exp\left\{-i\frac{q_x x}{\hbar}\right\} \cdot \mu_z\left(p_z\right) \\
& \cdot \chi^{(x)}_{z_2'}\left(-\frac{\frac{2\pi\hbar}{d} n\Delta z_{32}}{p_z} - \frac{q_x \Delta z_{52}}{p_z}, q_x + \frac{2\pi\hbar}{d} n\right) \\
& \cdot \theta\left(\frac{D_S}{2} - \left| y - p_y \frac{\Delta z_{50}}{p_z} - \frac{g m^2 \Delta z_{50}^2}{2p_z^2} \right|\right) \cdot \mu_y\left(p_y + \frac{g m^2 \Delta z_{50}}{p_z}\right) \cdot \\
& \cdot B_n\left(-\frac{q_x \Delta z_{53}}{p_z d}, y - \frac{p_y \Delta z_{53}}{p_z} - \frac{g m^2 \Delta z_{53}^2}{2p_z^2}\right) \cdot \\
& \cdot \theta\left(\frac{S_y}{2} - \left| y - y_{S_y} - \frac{p_y \Delta z_{54}}{p_z} - \frac{g m^2 \Delta z_{54}^2}{2p_z^2} \right|\right) \Bigg]
\end{aligned} \tag{5.25}$$

A full calculation, which leads to this result, is given in appendix D.1. Because our detection scheme is integrating the flux over time, this result is directly proportional to our measured signal. The functions $\mu_z\left(p_z\right)$ and $\chi^{(x)}_{z_2'}\left(s_x, q_x\right)$ appearing in (5.25) are defined in (D.17) and (D.8) respectively. To simplify the computation further we may also assume that the distribution $\mu_y\left(p_y\right)$ is approximately constant, by the same argument as for $\mu_x\left(p_x\right)$.

5.5. Interactions in the light grating

The derivation of (5.25) did not make any specific assumptions about the Talbot coefficients $B_n(\xi, y)$. As outlined in section 5.2 these coefficients describe the interaction of the molecules with the grating. They does define which grating mechanisms our model describes. In the case of our experiment part of the interaction is given by the effective potential the polarizable molecules sees in the light grating, as described in section 3.1.3. This gives rise to the standing light wave acting as a phase grating (see figure 1.1a). Additionally molecules can absorb photons as discussed in section 3.2. We can find different models describing giving approximate descriptions of some of the effects connected to absorption.

The dipole potential (3.14) in the standing light wave gives rise to an eikonal phase (5.12) acquired by the molecule during its transmission through the grating. We model the intensity profile of the standing light wave by a Gaussian beam [212, 240]

$$I(x,y,z) = \frac{8P}{\pi w_y w_z} \cdot \cos^2(kx) \cdot \exp\left(-\frac{2\left(y-y_0\right)^2}{w_y^2} - \frac{2z^2}{w_z^2}\right) \tag{5.26}$$

This includes the assumption that the waist radii are constant for the relevant values for x, which is justified by the large Rayleigh range in the experiment as discussed in section 4.4. P is the power of the laser forming the standing light wave, w_y and w_z are the waist radii along the corresponding axis. $k = \frac{2\pi}{\lambda}$ is the wavenumber of the laser. We also introduced the vertical position y_0 of the grating as a parameter. Inserting the intensity (5.26) into the relation for the potential (3.14) and integrating to compute the eikonal phase (5.12) yields [217]

$$\phi(x,y) = \phi_0(y) \cdot \cos^2(kx) \tag{5.27}$$

where the y-dependent maximum phase shift is given by

$$\phi_0(y) = \sqrt{\frac{8}{\pi}} \frac{\bar{\alpha} m P}{\hbar \varepsilon_0 c w_y p_z} \cdot \exp\left(-\frac{2\left(y-y_0\right)^2}{w_y^2}\right) \tag{5.28}$$

To describe absorption we first compute the mean number of absorbed photons by integrating (3.19) over t for a molecule passing through the intensity profile (5.26) [217]

$$\bar{n}(x,y) = \bar{n}_0(y) \cdot \cos^2(kx) \tag{5.29}$$

with the maximum mean number of absorbed photons

$$\bar{n}_0(y) = \frac{8\sigma m P}{\sqrt{2\pi}\hbar\omega w_y p_z} \cdot \exp\left(-\frac{2\left(y-y_0\right)^2}{w_y^2}\right) \tag{5.30}$$

Let us for a moment disregard molecules which have absorbed one or more photons, for example because they are almost certainly destroyed via a photocleavage process (see section 3.2.2). We can find the factor $t_0(\mathbf{x})$ in the transmission function (5.11) by requiring $|t_0(\mathbf{x})|^2$ to equal the probability for absorbing zero photons at $\mathbf{x}$. For a Poissonian distribution of absorption events this yields in combination with the eikonal phase (5.27)

$$t(x,y) = \exp\left\{\left(-\frac{\bar{n}_0(y)}{2} + i\phi_0(y)\right) \cdot \cos^2(kx)\right\} \tag{5.31}$$

Notice how the contribution from the absorption can also be recovered by inserting a complex polarizability into (5.28) and relating its imaginary part to the absorption cross section (3.3). For clarity we will however only denote the real part of the polarizability by α and write absorption cross section explicitly.

Expression (5.31) describes the transmission function for molecules which do not absorb photons and subsequently undergo changes in their state. However, as described in section 3.2 molecules can also redistribute the energy of an absorbed photon without immediately remitting it or undergoing major changes in structure. Such molecules may still be visible in our detection and in fact not be directly distinguishable from the ones which have not absorbed any photons. Since the process of absorption still changes the internal states there will not be a coherent superposition of different numbers of photon absorptions for a particular molecule. Instead we observe an incoherent sum of the different contributions. The absorption of a photon results in a change of the molecular momentum by $\pm\hbar k$ along the x-axis. Since the standing light wave itself is a superposition of two counter-propagating waves the molecules are in fact in a coherent superposition of the two possible "kicked" momentum states. $1\hbar k$ momentum transfers result in a additional peaks which can be observed in the experiments. These peaks lie in-between the usual maxima one expects in far-field diffractions, which correspond to multiples of the grating kick $\hbar\frac{2\pi}{d} = 2\hbar k$ ($d = \lambda/2$ is the grating period). This realizes the mechanism denoted absorption & heating in figure 1.1b [9, 272].

An effective description of a molecule which can undergo potentially multiple photon absorptions is given by the ladder model presented in [217, 272]. In this model photon absorptions are described by generalized measurements. The number of absorbed photons l would in principle be encoded in the thermal state of the molecule. If the molecules stay intact the imaging in our experiment is in general insensitive to the thermal state of the detected molecules. In this case our results are described by the *unconditional Talbot coefficients*

$$B_n(\xi, y) = e^{-\zeta'_{\mathsf{abs}}} \left(\frac{\zeta_{\mathsf{coh}} + \zeta'_{\mathsf{abs}}}{\zeta_{\mathsf{coh}} - \zeta'_{\mathsf{abs}}}\right)^{\frac{n}{2}} \cdot J_n\left(\operatorname{sgn}\left(\zeta_{\mathsf{coh}} - \zeta'_{\mathsf{abs}}\right)\sqrt{\zeta_{\mathsf{coh}}^2 - \zeta'^2_{\mathsf{abs}}}\right) \tag{5.32}$$

Here $J_n(x)$ is the Bessel function of the first kind. The two new expressions in (5.32), whose functional dependence we did not write explicitly, are defined as

$$\zeta_{\mathsf{coh}}(\xi, y) = \phi_0(y)\sin(\pi\xi) \tag{5.33}$$

and

$$\zeta'_{\mathsf{abs}}(\xi, y) = \bar{n}_0(y)\sin^2\left(\frac{\pi\xi}{2}\right) \tag{5.34}$$

The y-dependence in our expressions enters through the definitions (5.28) and (5.30).

For the case of photodepletion gratings (figure 1.1c and d) only the case of $l = 0$ absorptions contributes to the interference pattern, if we assume that this process happens with $100\ \%$ efficiency. In this case we need the *conditional Talbot coefficients*. They are given by

$$B_n(\xi, y; l = 0) = e^{-\frac{\bar{n}_0}{2}} \left(\frac{\zeta_{\mathsf{coh}} - \zeta_{\mathsf{abs}}}{\zeta_{\mathsf{coh}} + \zeta_{\mathsf{abs}}}\right)^{\frac{n}{2}} \cdot J_n\left(\operatorname{sgn}\left(\zeta_{\mathsf{coh}} + \zeta_{\mathsf{abs}}\right)\sqrt{\zeta_{\mathsf{coh}}^2 - \zeta_{\mathsf{abs}}^2}\right) \tag{5.35}$$

Here we introduced

$$\zeta_{\mathsf{abs}}(\xi, y) = \frac{\bar{n}_0(y)}{2}\cos(\pi\xi) \tag{5.36}$$

Conditional Talbot coefficients corresponding to higher numbers l of absorbed photons can be computed iteratively starting from (5.35):

$$B_n(\xi, y; l) = \sum_{k=0}^{l}\sum_{m=0}^{k}\left(\frac{\bar{n}_0}{4}\right)^k \cdot \frac{(l-m)!\,\zeta_{\mathsf{abs}}^{l-k}}{l!\,(l-k)!\,(k-m)!} \cdot B_{n-k+2m}(\xi, y; l = 0) \tag{5.37}$$

Derivations of (5.32), (5.35) and (5.37) are given in [217]. These particular models do not incorporate the effects of fluorescence and also assume that the polarizability and absorption cross-section are the same for all molecular states in the "ladder". As already mentioned, modelling a photodepletion grating with (5.35) also implicitly assumes that the process leading to the removal of molecules from the signal happens with $100~\%$ efficiency after absorption of a photon.

6. Data evaluation

6.1. Overview

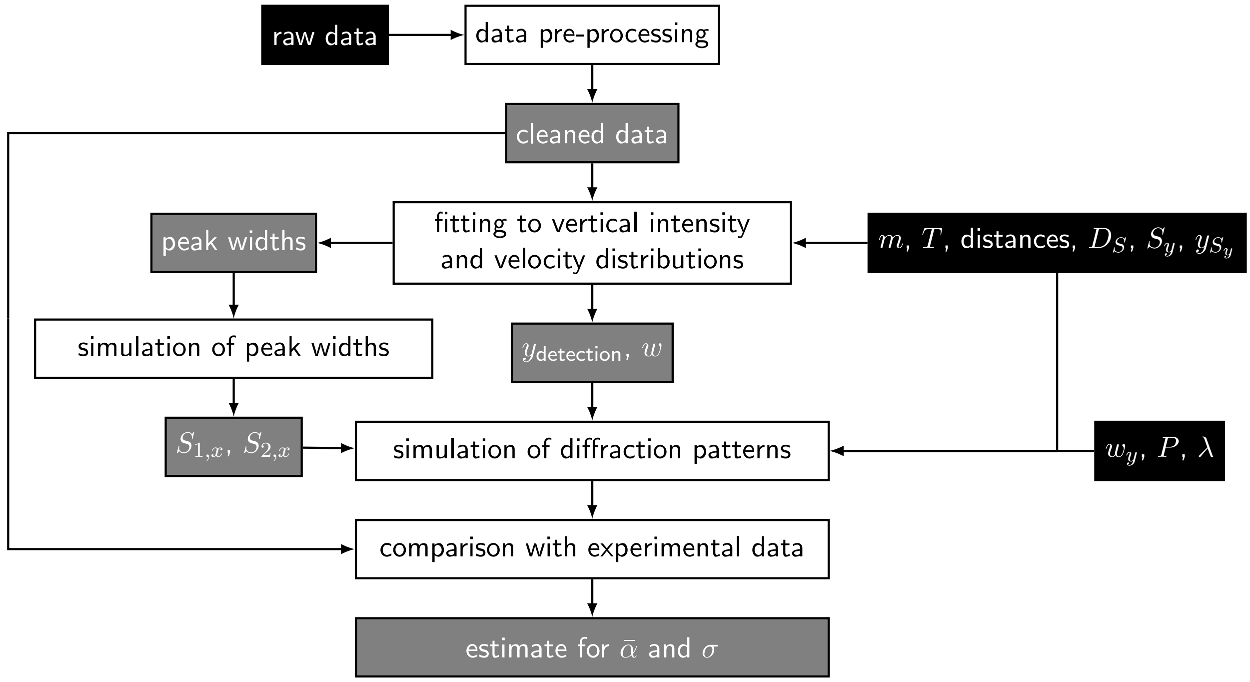

Figure 6.1: Schematic overview of the data evaluation procedure. Experimentally determined parameters are represented by black rectangles, parameters extracted from the data are shown in gray. The white boxes represent the individual steps in the evaluation.

In the previous section we gave an outline of how the diffraction pattern corresponding to our experiment can be computed for an optical light grating. For a given velocity distribution and fixed geometrical parameters, the observed flux (5.25) is determined by the Talbot coefficients $B_n(\xi, y)$. In section 5.5 we have seen that these coefficients encode optical properties of the molecules. In the particular model considered here, these are the (scalar) mean dipole polarizability $\bar{\alpha}$ and the optical absorption cross section σ at the frequency of the laser used in the experiment. The model also differs depending on whether molecules which have undergone absorption contribute to the signal (unconditional Talbot coefficients (5.32)) or if we consider a photodepletion grating (conditional Talbot coefficients (5.35)).

The extraction of the optical parameters from the experimental signal is hindered by the lack of precise knowledge of all geometrical parameters appearing in (5.25). Concretely, the absolute heights of the light grating y_0. the velocity selector y_{S_y} and the detection region relative to the source are not known. As mentioned in section 4.3.4 the absolute widths of the collimation slits $S_{1,x}$ and $S_{2,x}$ could also not be precisely determined from the experiment. Finally the velocity shift w appearing in the description of the free-jet expansion (4.3) is also an unknown parameter. Because of this we first apply separate fitting procedures for the geometrical parameters of the collimation slits and the velocity shift w. These can be determined without modelling the diffraction, we describe the procedure in section 6.3. This allows us to reduce the number of free parameters to y_0, $\bar{\alpha}$ and σ. We can then simulate the diffraction according to (5.25) on a grid of values $\bar{\alpha}$ and σ for. We use this parameter sweep to find the combination of parameters that best fits the experimental data in order to find an estimate for that actual values. This is also done for different values of y_0 to treat this remaining degree of freedom and find the best fitting grating height y_0. Beforehand we however need to apply some cleaning and pre-processing to our raw data. This is summarized in section 6.2. Figure 6.1 shows a schematic of the steps in the data evaluation and the origin of the parameters used.

6.2. Data pre-processing

The diffraction patterns recorded using the imaging setup described in section 4.6.1 are 1003×1003 pixels large images of brightness values (counts). An initial background subtraction is done in software directly when recoding the images. For this purpose background data with the illumination laser blocked is taken. Nevertheless we apply two additional steps of background correction. An additional background image is recorded before depositing the molecules with the illumination laser open. This accounts e.g. for additional signal originating from the fluorescence filter (filter 2 in figure 4.26) not perfectly blocking the illumination laser. The background image can be aligned with the actual data by comparing the location of small dust spots which are visible in some regions of most images. In the next step of data cleaning regions of the image containing such contaminations are manually removed. Singular spikes in the experimental data are removed by excluding the top and bottom $0.001\ \%$ of the data. In the final step of background subtraction we fit a linear model $f(x, y) = p_{00} + p_{10} \cdot x + p_{01} \cdot y$ to the remaining background and subtract it. The actual fluorescence signal is manually excluded from this fit. This step ensures that slight variations in ambient light between the recording of the diffraction pattern and the background without the molecules do not introduce an additional offset. Finally the data is normalized to the mean of the top $0.01\ \%$ of data points. For the purposes of plotting the images are additionally cropped and centered.

6.3. Estimation of source and slit parameters

To determine the velocity shift w in (4.3) and the vertical offset $y_{\text{detection}}$ of the detection region with respect to the source we compare the vertical intensity distributions in the experiment and the simulation. It turns out that with appropriate shifts of y_0 and $y_{\text{detection}}$ the results are for all intends and purposes independent of the height y_{S_y}. It is therefore arbitrarily set to $y_{S_y} = -150\,\mu\mathrm{m}$, which is approximately the distance expected from free fall over the distance Δz_{40} for a typical velocity of $v_z \approx 180\,\mathrm{m\,s^{-1}}$. Integrating our theoretical model (5.25) over x yields

$$\begin{aligned}\int_{\mathbb{R}} \mathrm{d}x\; j(\mathbf{x}) \propto \int_{\mathbb{R}^+} \mathrm{d}p_z \int_{\mathbb{R}} \mathrm{d}p_y \; \Bigg[& p_z \cdot \mu_z(p_z) \cdot \; \theta\left(\frac{D_S}{2} - \left| y - p_y \frac{\Delta z_{50}}{p_z} - \frac{g m^2 \Delta z_{50}^2}{2 p_z^2} \right| \right) \cdot \\ & \cdot \theta\left(\frac{S_y}{2} - \left| y - y_{S_y} - \frac{p_y \Delta z_{54}}{p_z} - \frac{g m^2 \Delta z_{54}^2}{2 p_z^2} \right| \right) \Bigg]\end{aligned} \tag{6.1}$$

This follows from $B_n(0, y) = \delta_{n,0}$ and $\chi^{(x)}_{z_2'}(0, 0) \propto p_z$ [271]. The former is strictly speaking only true for the unconditional Talbot coefficients (5.32). For the moment however we will restrict ourselves to this model. The slit and source sizes D_S and S_y, the mass m of the molecules and the distances between the components (see table 1) are known experimental parameters. The temperature T appearing in $\mu_z(p_z)$ (D.17) is estimated as the nozzle temperature T_N measured by the thermocouple in the experiment (see section 4.2). We can then fit the normalized model (6.1) to the normalized horizontally integrated experimental data to determine the remaining free parameter w (appearing in (D.17)) and the offset $y_{\text{detection}}$.

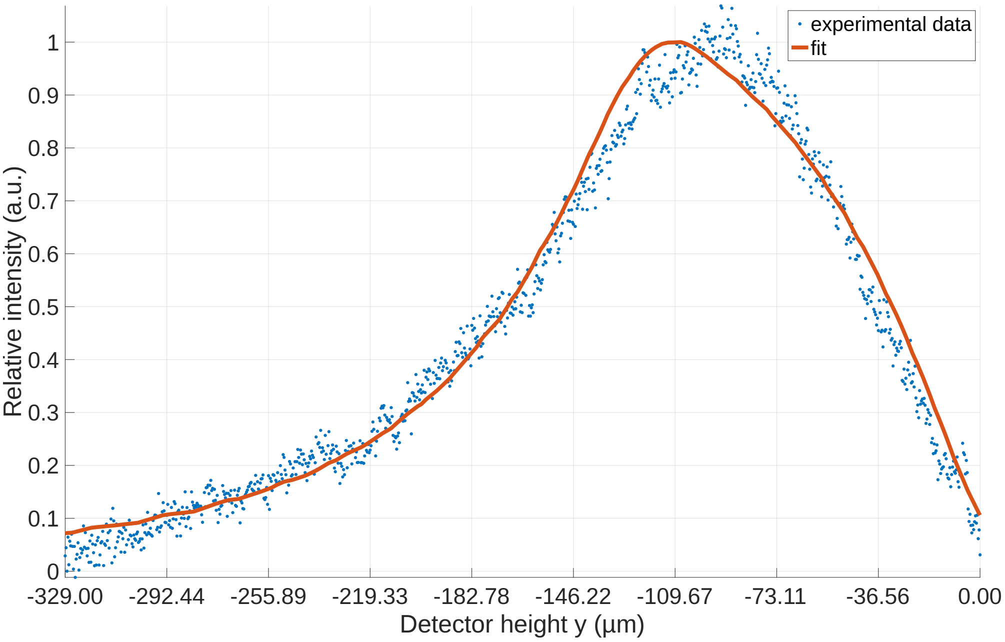

Figure 6.2: Horizontally integrated intensity as a function of y-position at the detector for PcH$_2$. The red curve shows the same quantity extracted from the theoretical model fitted to this data. Here $y_{S_y} = -150\,\mu\text{m}$ was chosen. The fit gave the results $w = 74.3\,\text{m}\,\text{s}^{-1}$, $y_{\text{detection}} = -226\,\mu\text{m}$. The heights y shown in the graph are given relative to $y_{\text{detection}}$.

An example for such a fit is shown in figure 6.2 for PcH$_2$. The good agreement with the experimental data also demonstrates that the free-jet expansion (4.3) seems to be an appropriate model here. To further validate these results we also compare the vertical distribution of velocities v_z with the model. We compute the relative distribution of the velocities v_z at each height in analogy to (6.1) via

$$\begin{aligned}\Phi_z(v_z, y)\,\mathrm{d}v_z \propto \int_{\mathbb{R}} \mathrm{d}p_y \Bigg[v_z \cdot \mu_z(p_z) \cdot \theta\left(\frac{D_S}{2} - \left| y - p_y \frac{\Delta z_{50}}{p_z} - \frac{g m^2 \Delta z_{50}^2}{2p_z^2} \right|\right) \cdot \\ \cdot\, \theta\left(\frac{S_y}{2} - \left| y - y_{S_y} - \frac{p_y \Delta z_{54}}{p_z} - \frac{g m^2 \Delta z_{54}^2}{2p_z^2} \right|\right) \mathrm{d}v_z \Bigg]\end{aligned} \tag{6.2}$$

where $p_z = m \cdot v_z$. To estimate the velocities from the experimental data we separate the data into $10-20$ horizontal slices over each of which the data is vertically integrated. To each slice a symmetrically spaced Gaussian functions are fitted to determine the average separation between the diffraction peaks. From this we can estimate the diffraction angle θ and thus the de Broglie wavelength λ_{dB}. (2.1) then allows the calculation of v_z. Care needs to be taken if there are additional diffraction peaks originating from absorption (see section 5.5), which is the case for our example of PcH$_2$. In general we can give a reasonable estimate of the velocity from the thermal distribution in the source via (4.5) or (4.6) (see table 2), which allows to determine whether the first order peaks correspond to a $1\hbar k$ or $2\hbar k$ momentum recoil. Exemplary results for the comparison of the velocity distributions are shown in figure 6.3. The plot shows a heatmap of the velocity distribution (6.2) parametrized by y and v_z. The experimentally determined velocities are shown for 10 slices in blue. The plot shows a good agreement between the fitted velocities and the regions with the highest probability at each height. For the top most values of

y this agreement becomes less good, however the quantity of the fits to the slices becomes worse as well because the separation of the peaks is no longer large enough for high velocities to accurately fit them.

The Gaussian fits to the diffraction peaks used to extract the velocities from the slices is also used to gain an estimate for the width of the diffraction peaks. We use this information to fix the absolute widths of the collimation slits $S_{1,x}$ and $S_{2,x}$, which could not be determined with accurately enough from the experiment as outlined in section 4.3.4. The 2σ widths of the Gaussian functions fitted to the peaks are extracted for each slice. This is shown for the example of PcH$_2$ in figure 6.4. The average width is marked in red. The parameters $S_{1,x}$ and $S_{2,x}$ are now optimized such that this width is matched. We expect the width of an undiffracted beam to be approximately the same as the with of the diffraction peaks. This can be understood from the fact that (for each n) (5.25) is given by a convolution with the Fourier transform $\chi^{(x)}_{z_2'}(s_x, \tilde{q}_x)$, which also describes the undiffracted beam since the shift introduced by the n is not expected to change the width significantly. We thus extract the 2σ width from the model by computing

$$j(x) \propto \int_{\mathbb{R}} \mathrm{d}p_z \int_{\mathbb{R}} \mathrm{d}q_x \; \exp\left\{-i\frac{q_x x}{\hbar}\right\} p_z \cdot \mu_z(p_z) \cdot \chi\left(-\frac{q_x \Delta z_{52}}{p_z}, q_x\right) \tag{6.3}$$

and fitting a Gaussian function

$$f(x) = C \cdot \exp\left\{-\frac{(x-x_0)^2}{2\sigma^2}\right\} \tag{6.4}$$

to it. Note that we also removed the y-dependence in (6.3) and instead integrated over all p_z without the restriction introduced by the theta functions in (5.25). However, since the averaging over all heights in the experimental data also corresponds to an averaging over velocities this should still give an appropriate estimate.

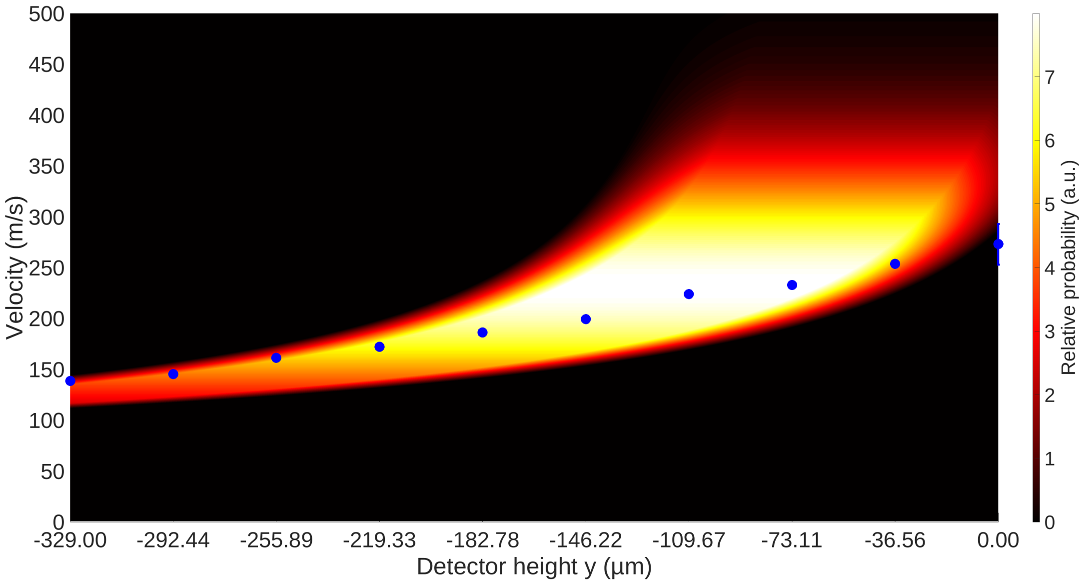

Figure 6.3: Heatmap of the v_z velocity distribution at different detection heights y with experimentally determined velocities (blue). Heights are given relative to $y_{\text{detection}}$. For all but the last datapoint the error bars are smaller than the visible size of the marker.

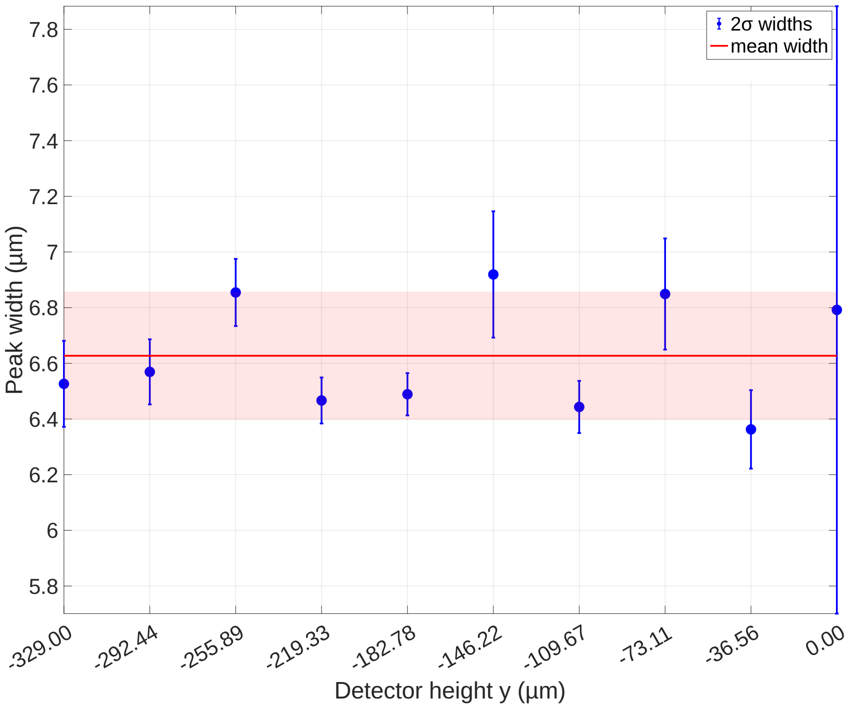

Figure 6.4: 2σ widths fitted to slices of experimental data for PcH$_2$. The red line shows the average width ($(6.6 \pm 0.3)\,\mathrm{\mu m}$), the shaded red area indicates the associated uncertainty. Because of the larger velocities at the top of the screen accurate fitting was not possible for the hightest point.

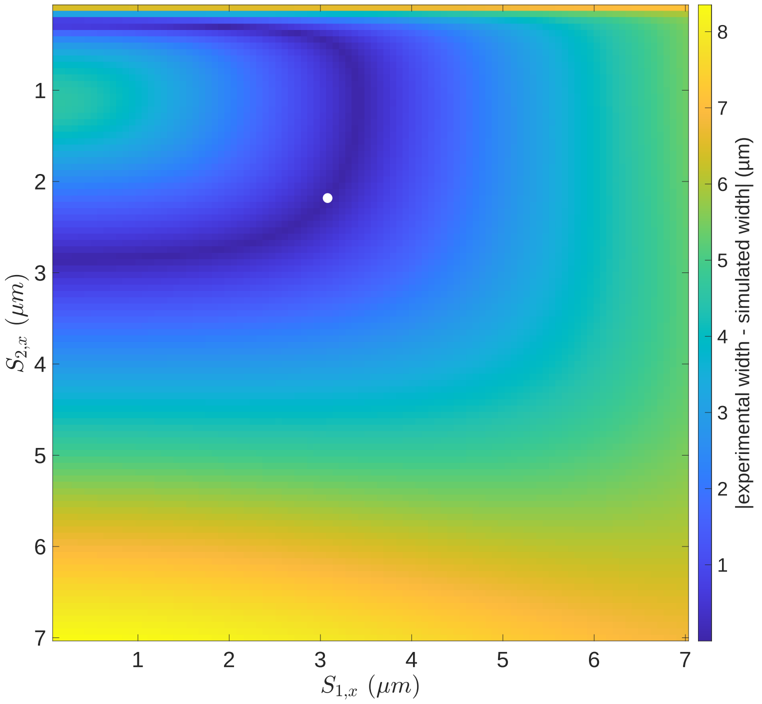

Figure 6.5: Parametric plot of the absolute difference between the width extracted from the simulation and the one determined from the fits in figure 6.4 as a function of $S_{1,x}$ and $S_{2,x}$. The white circle marks the combination of slit widths chosen for the further evaluation of the PcH$_2$ data.

Finally we compute the absolute difference of the simulated width and the experimentally determined one for a range of values for $S_{1,x}$ and $S_{2,x}$. Figure 6.5 shows a parametric plot of this absolute difference for the case of PcH_2. As can be seen from this plot, there is a range of possible combinations for the two slit widths which yield a good agreement with the stripe width extracted from the fit to the experimental data. For the further evaluation we choose a combination where $S_{1,x}$ and $S_{2,x}$ have a similar size. The influence of the silt sizes beyond determining the width of the diffraction peaks should only become relevant if the single slit diffraction at $S_{2,x}$ makes a noticeable contribution. Since the diffraction effects from the light grating are dominant, the precise choice of the values is not expected to matter too much.

6.4. Simulation of diffraction patterns and parameter sweep

The procedures described in section 6.3 allow for a reasonable estimation of most unknown experimental parameters. The only free parameters left in the computation of (5.25) are the mean polarizability $\bar{\alpha}$ (strictly speaking this is the real part of the polarizability), the photon absorption cross-section σ and the vertical position of the light-grating y_0. In order to gain an estimate for the former two parameters, which are properties of the molecule itself, we will numerically evaluate (5.25) for a large number of combinations of both values on appropriate intervals. The theoretical model is compared to the (cleaned) experimental data to gain an estimate for the best match. y_0 is held fixed for this purpose, however we repeat the evaluation for several values of y_0 to also find the best agreement here.

The numerical simulation is written in *Matlab* and *Julia*. Computation of (5.25) is slightly simplified to reduce the computational cost. As mentioned at the end of section 5.4 we approximate $\mu_y(p_y)$ as constant. We further first only need to compute the inverse Fourier transform of (5.25), which is a function of q_x and y. As discussed in appendix D.2 we only need to carry out this evaluation for positive q_x because the inverse Fourier transform will be symmetric around zero. For the purposes of calculation we can also integrate the theta-function dependence in (5.25) into the integration limits for p_y. We can then evaluate the inverse Fourier transform of the flux (5.25) at every point (q_x, y). To keep the computational cost low this is done at a resolution of 500×10 pixels. The higher resolution for q_x is necessary to properly resolve the diffraction effects, while we can be more lenient with averaging along the y-axis. For the comparison to the experimental data we then apply the Fourier transform along the x-axis in equation (5.25). If the diffraction pattern was already centered in the pre-processing step. We also correct a small rotational misalignment of the experimental images at this step if necessary.

For each combination of $\bar{\alpha}$ and σ the sum of the squared differences of all pixels in the simulated and experimental images is computed. These values are collected in a parametric plot to find the regions of best agreement between the two images, which allows us to estimate the optical parameters. For large differences of $\bar{\alpha}$ and σ to the optimal values qualitative differences in the diffraction images become apparent (e.g. higher order peaks). We use this to set limits on the regions over which the parameters are sampled. After the regions with good agreement between the experiment and simulation are found, a more restricted array of values is investigated. This analysis may be carried out with any of the models for the Tablot coefficients discussed in section 5.5. If the destruction of the molecules can be neglected the unconditional Talbot coefficients (5.32) are expected to be the most appropriate. For photodepletion gratings (e.g. via photocleavage) we can use the $l = 0$ absorptions conditional Talbot coefficients (5.35) as a model if we assume that the depletion process happens with $100\ \%$ efficiency after absorption of a single photon. To account for the more general case where this is not necessarily the case the model needs to be further adapted, which will however not be covered here [217, 271]. When not using the unconditional Talbot coefficients, our assumptions which allowed us to write the intensity distribution as (6.1) are no longer true. When running the simulation with the conditional Talbot coefficients we therefore use an adapted version of this relation which includes these Talbot coefficients. In this case we need to start with an initial guess for the absorption cross-section and grating height. After fitting with this adapted intensity distribution we can proceed as usual. Intuitively one can understand that such a modification is necessary because in the cases using the conditional Talbot coefficients absorption events lead to a loss of molecules. The overall intensity distribution is thus modified depending on how likely such an absorption event is for a molecule landing at a certain height.

7. Results

7.1. H_2-phthalocyanine

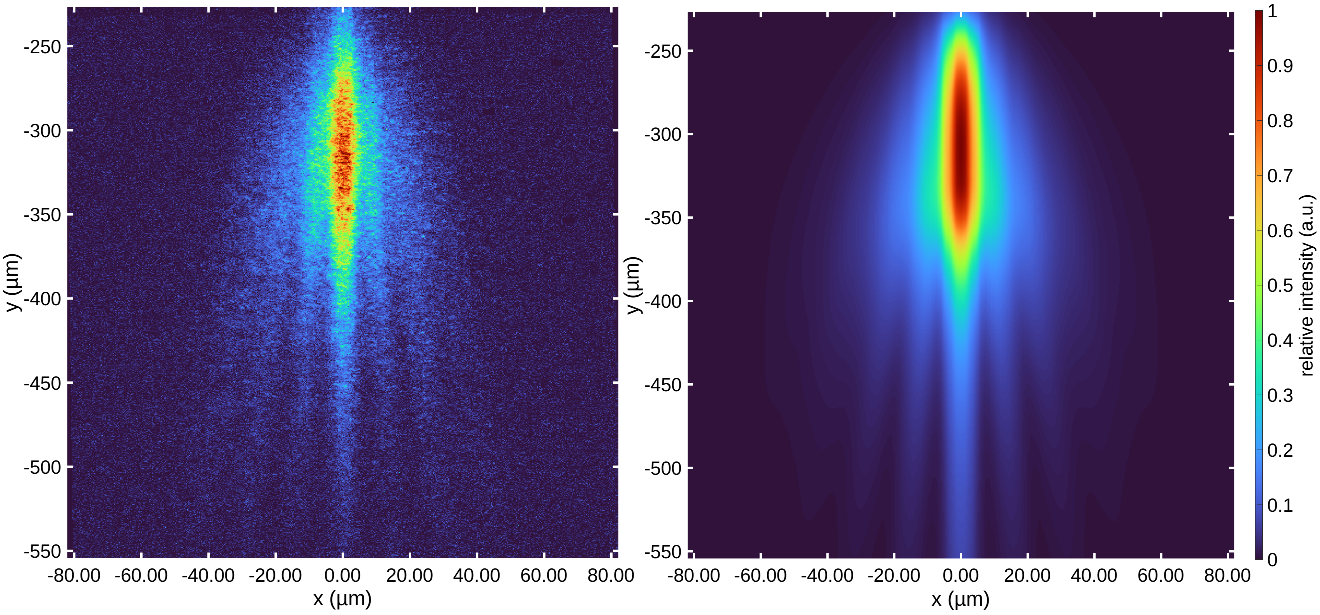

(a) Background subtracted experimental data for PcH_2. **(b)** Simulated data for PcH_2 with optimal parameters.

Figure 7.1: Comparison between experimental data with the simulation results for PcH_2. The joint colorbar of both images on the right shows the normalized intensity. Note that the horizontal axes of both images are stretched by a factor of two compared to the vertical axis.

A typical diffraction image recorded for PcH_2 is shown in figure 7.1a. The data shown in the figure has already underwent the pre-processing described in section 6.2 and is stretched by a factor of two along the horizontal axis to better show the individual diffraction peaks. We can recognize up to three diffraction peaks to each side of the zeroth order in figure 7.1a. This can be seen a bit more easily in figure 7.2, which shows the vertically integrated data of the bottom 150 pixels ($49\,\mu\mathrm{m}$) of the image. Using the velocity estimates from table 2 we can deduce that these peaks effectively correspond to momentum recoils $n\hbar k$, which are multiples of the photon momenta $\hbar k$ of the light grating. The first and third diffraction peaks thus correspond to odd multiples of this photon momentum. As discussed in section 5.5 they can therefore be attributed to absorption of photons (without photocleavage or other loss mechanisms).

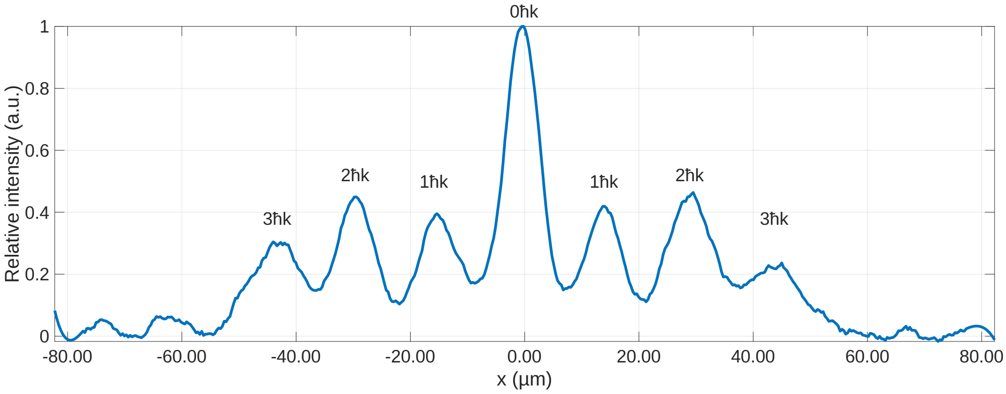

Figure 7.2: Experimental data integrated over the bottom 150 pixels in figure 7.1a. Savitzky-Golay-filtering [273] was applied to smooth the data. The photon momentum recoils $n\hbar k$ associated with the peaks are marked in the figure.

Results of the fitting to the velocity distribution of this data was already shown in section 6.3. For the simulation of the experiment the unconditional Talbot coefficients (5.32) were used. The absolute height of the light grating y_0 was also still a free parameter in this simulation. The data shown here corresponds to the height, which showed the best agreement with the experiment. This also coincides with the height for which the diffraction effect appears the most intense visually in the simulation.

Figure 7.3 shows the comparison of the simulation with the experimental data for a range of $\bar{\alpha}$ and σ values. For each combination of parameters the squared difference of the experimental data and the simulation is shown summed over all pixels. A larger parameter space was also investigated, figure 7.3 shows the region with the best match between experiment and simulation in detail. As is apparent from figure 7.3 there two regions for which the value pairs $(\bar{\alpha}, \sigma)$ give a similarly good agreement with the experiment. In figure 7.3 the dark blue to black regions have the minimum discrepancy between experiment and simulation. Since the experimental data is always subject to noise and other factors not included in the simulation, this minimum is always still clearly larger than zero. Even though the parametric plot does not determine an unambiguous set of optimal vales for $\bar{\alpha}$ and σ, we can still use it to infer reasonable restrictions for the parameters:

$$5 \cdot 10^{-21}\,\mathrm{m}^2 \lesssim \sigma_{266\,\mathrm{nm}} \lesssim 7 \cdot 10^{-21}\,\mathrm{m}^2 \tag{7.1}$$

and

$$7\,\mathrm{\AA}^3 \cdot 4\pi\varepsilon_0 \lesssim |\bar{\alpha}_{266\,\mathrm{nm}}| \lesssim 15\,\mathrm{\AA}^3 \cdot 4\pi\varepsilon_0 \tag{7.2}$$

As expected this only gives us a broad estimate of the optical parameters. However, if one of the parameters would be measured more accurately via other means, we would already be able to conclude more concrete information about the other parameter from the correlation between the two in figure 7.3. Also note that for the parameters of our experiment the results are almost perfectly symmetric for positive and negative values of $\bar{\alpha}$. We can therefore not make any conclusions about the sign of the dynamic polarizability here. Nevertheless we see that the approximate value (7.1) we determined does more or less agree with the order of magnitude of the estimate we presented in section 4.7.1. In fact, our results suggest that we overestimated the cross-section by at least a factor of two in section 4.7.1, which is not unreasonable considering that the comparison with solution measurements we used there was only an estimate for the order of magnitude of σ. The limits for the dynamic polarizability (7.2) extracted from our measurements are clearly significantly smaller than the static values of PcH_2 cited in section 4.7.1, demonstrating the relevance of analysing a specific frequency. Our results are indeed much better in line with the DFT calculations mentioned at the end of section 4.7.1 and might give insight into determining the best computation method.

Note that the further evaluation of the results in figure 7.3 and also the following sections must also consider the uncertainties in some of the experimental parameters. The numbers given in (7.1) and (7.2) do not yet take this additional uncertainty factors into account. Most importantly, the mean laser power in the standing light wave during the measurement was only known as $P = (0.96 \pm 0.04)\,\mathrm{W}$ for the data presented here. The relevant parameters in (5.28) and (5.30) are actually the products $\bar{\alpha} \cdot P$ and $\sigma \cdot P$. This means that the polarizability and absorption cross-section extracted from the simulation, which assumed the mean value for the laser power P, necessarily have at least the same relative uncertainty of $\sim 5\ \%$. In this case the spread of values if reasonable agreement in figure 7.3 is clearly the more limiting factor, however the uncertainty of the laser power, which has its origin in the limited stability of the laser remains as the fundamental limit for the accuracy of the values extracted. Additionally there will also be an indirect influence of e.g. the geometric parameters which went into the simulation.

The minimum of the difference measure plotted in figure 7.3 is found for the value pair $\bar{\alpha} = 10.3\,\mathrm{\mathring{A}}^3 \cdot 4\pi\varepsilon_0$, $\sigma = 6.3 \cdot 10^{-21}\,\mathrm{m}^2$. However, the other dark blue areas in figure 7.3 show only minor differences compared to this value set. These differences are more likely attributed to the numerics of the computation. In particular we have more or less the same optimal agreement for $\bar{\alpha} = -10.3\,\mathrm{\mathring{A}}^3 \cdot 4\pi\varepsilon_0$ because of the aforementioned high symmetry of the results. We still use the previously stated optimal value pair as an example to highlight the agreement between experiment and simulation. The simulated diffraction pattern for these parameters is plotted in figure 7.1b next to the experimental data. Both datasets are normalized and plotted with the same color scale for easy comparison. Evidently the simulation matches the data well for these parameters. However, the agreement is not perfect.

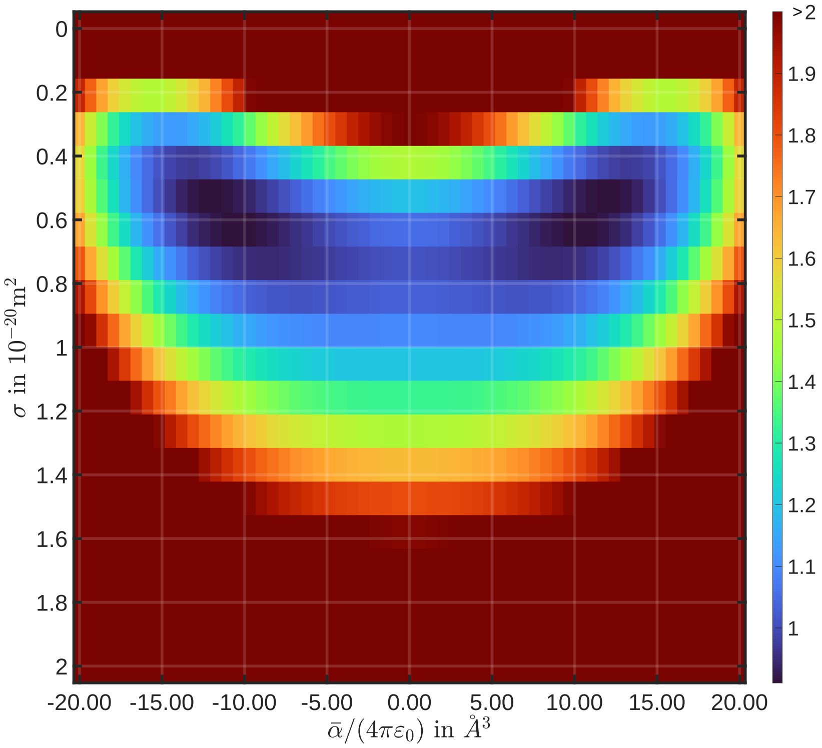

Figure 7.3: $(\bar{\alpha}, \sigma)$ parameter sweep for PcH_2. The plot shows the squared differences of the experimental and simulated data summed over all pixels. As indicated by the colorbar on the right dark blue values correspond to the best agreement.

The model presented so far assumed the unconditional Talbot coefficients (5.32), i.e. that the molecules stay intact after an arbitrary number of absorptions. This might not necessarily be realistic as photoionisation after absorption of multiple photons might occur. We also compared the experiment so simulation data for a model, which only included the $l = 0$ and $l = 1$ conditional Talbot coefficients given by (5.35) and (5.37). In this description absorption of two photons in the light grating leads to loss of the molecules e.g. by ionization with $100\ \%$ efficiency. Meanwhile molecules, which only absorb a single photon, remain unaffected. Even though this model is also describing a very idealized case, it might indicate if such multi-photon ionization processes have to be considered, if it gives a better or at least similarly good match for the experimental data with appropriate parameters. However, the agreement of our simulation with the data was significantly worse in this case over a wide range of $(\bar{\alpha}, \sigma)$ values. Our first model was thus more fitting in this case. However, a more refined model including efficiencies different than unity might be necessary for a better fitting description. We can also see qualitatively by comparing the experimental data and the simulation shown in figure 7.1 that the model using the unconditional Talbot coefficients (5.32) gives already a good description of the experiment.

7.2. Meso-tetraphenylporphyrin

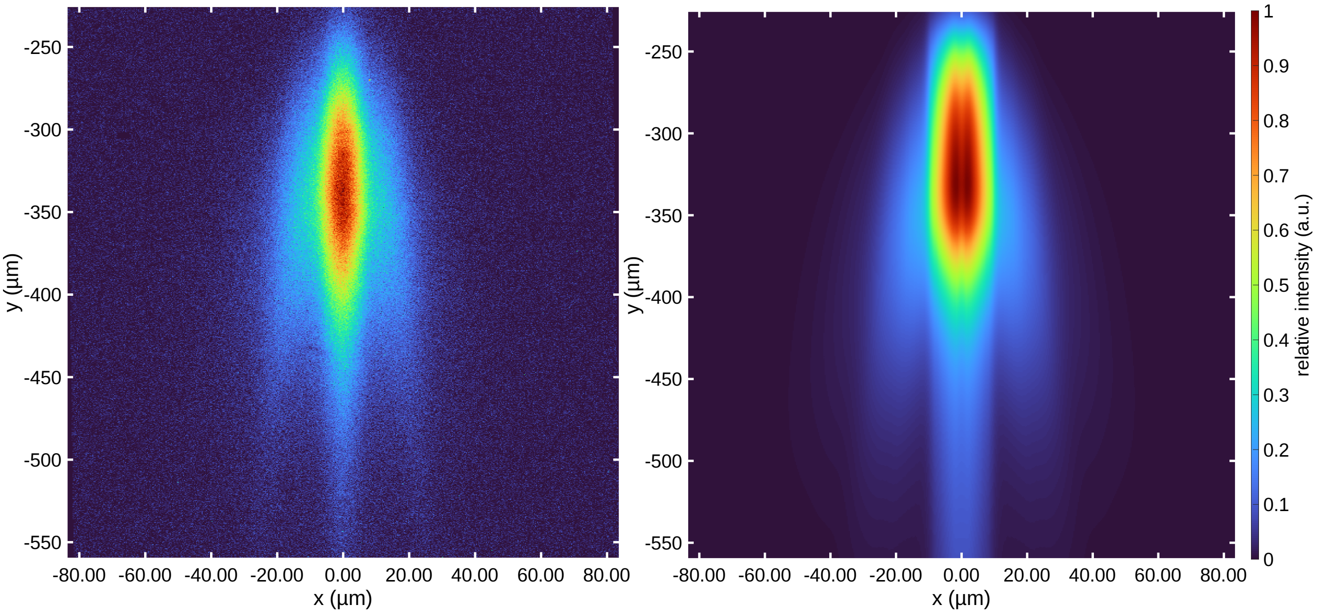

(a) Background subtracted experimental data for TPP **(b)** Simulated data for TPP with optimal parameters using the unconditional Talbot coefficients.

Figure 7.4: Comparison between experimental data with the simulation results for TPP. The joint colorbar of both images on the right shows the normalized intensity. Note that the horizontal axes of both images are stretched by a factor of two compared to the vertical axis.

The fits to the intensity and velocity distributions of TPP showed a similarly good agreement to the ones for PcH_2 shown in section 6.3 and also yielded similar numerical values for $y_{\text{detection}}$ and w. For $y_{\text{detection}}$ in particular this was expected, as the alignment procedure described in section 4.5.1 was designed to make the geometrical parameters as reproducible as possible. We thus already see a level of consistency from this. In figure 7.4 the comparison between the experimental data (left) and the simulated diffraction pattern (right) for the optimal values $(\bar{\alpha}, \sigma)$ is shown. The results of the parameter sweep for the model using the unconditional Talbot coefficients (5.32) are collected in figure 7.5. As for

PcH_2 we cannot extract definitive values for the parameters but are able to give estimates, which show acceptable agreement between the simulation and the experiment. We can give the approximate values

$$\sigma_{266\,\mathrm{nm}} \approx 1 \cdot 10^{-21}\,\mathrm{m}^2 \tag{7.3}$$

and

$$13\,\mathrm{\mathring{A}}^3 \cdot 4\pi\varepsilon_0 \lesssim |\bar{\alpha}_{266\,\mathrm{nm}}| \lesssim 17\,\mathrm{\mathring{A}}^3 \cdot 4\pi\varepsilon_0 \tag{7.4}$$

Similarly to PcH_2 we also seem to have overestimated the absorption cross-section in section 4.7.2. Our estimate for the polarizability (7.4) is also again clearly much smaller than the static value reported in section 4.7.2. However, again the numbers given here are effectively only an order of magnitude estimate as the same additional experimental uncertainties exist as in the case of PcH_2. The optimal values in figure 7.5 are $\bar{\alpha} = -14.5\,\mathrm{\mathring{A}}^3 \cdot 4\pi\varepsilon_0$, $\sigma = 1.1 \cdot 10^{-21}\,\mathrm{m}^2$. Also in this case the simulation results do not allow us to draw any decisive conclusion about the sign of $\bar{\alpha}$. The numbers found for the optimum are used to compute the simulated diffraction pattern shown in figure 7.4b. Also in this case we see a decent agreement between simulation and experiment. In particular both images lack a $1\hbar k$ recoil peak, which was present in the case of PcH_2. Our results suggest that this is explained by a lower absorption cross-section of TPP at this wavelength.

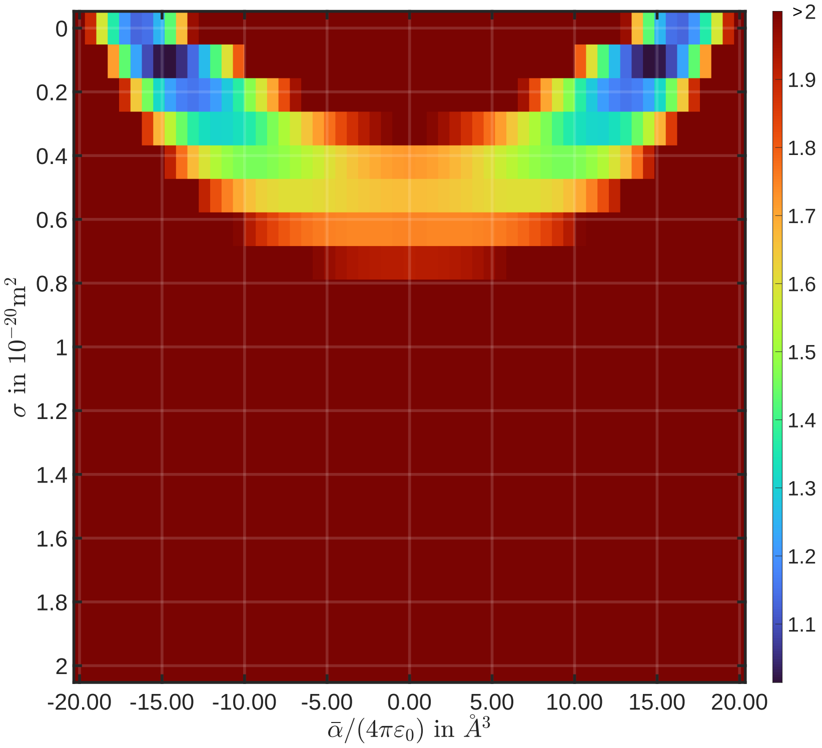

Figure 7.5: $(\bar{\alpha}, \sigma)$ parameter sweep for TPP with unconditional Talbot coefficients (5.32). The plot shows the squared differences of the experimental and simulated data summed over all pixels. As indicated by the colorbar on the right dark blue values correspond to the best agreement.

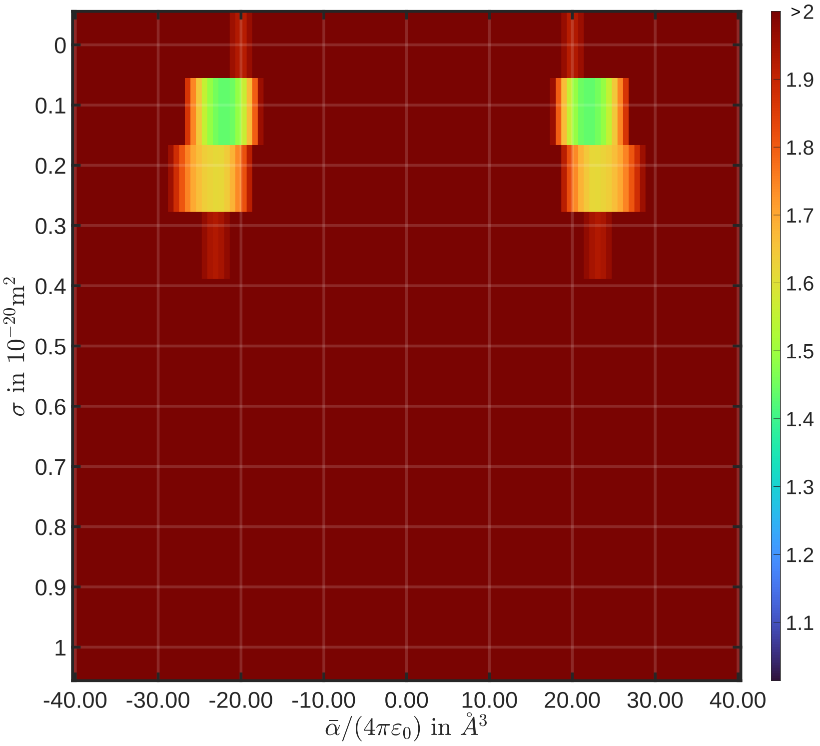

Figure 7.6: $(\bar{\alpha}, \sigma)$ parameter sweep for TPP with conditional Talbot coefficients for $l = 0$ (5.35). The plot shows the squared differences of the experimental and simulated data summed over all pixels. For better comparison the colorbar uses the same scale as in figure 7.5.

Despite the good agreement observed so far, we also want to consider another model besides the one using the unconditional Talbot coefficients (5.32), which we used for computing the data in figure 7.5. To treat the possibility that one of the phenyl rings (see figure 4.28) of the TPP molecule is cleaved off after absorption of a UV photon we additionally run the simulation with the conditional Talbot coefficients for the case of $l = 0$ (5.35). This corresponds to a model where such a cleavage (or another depletion mechanism) occurs with $100\ \%$ efficiency after absorption of a single photon. The results for the parameter sweep with this model are shown in figure 7.6. The same color scale as in figure 7.5 was used to facilitate easy comparison. Clearly the agreement is better for the model using the unconditional Talbot coefficients we discussed previously. Nevertheless, we see that even if the other model was more fitting for other reasons, the predictions for the absorption cross-sections would not be significantly different. Meanwhile the polarizabilities would need to be higher to give a better agreement in. In any case we cannot exclude the possibility of photocleavage from our results since our model assumed perfect efficiency, which is possibly not realistic.

7.3. Zn-phthalocyanine with photocleavable tags

The main goal of our analysis of the results for Zn-phthalocyanine with photocleacable tags is to see the effects of the photocleavage and confirm that this is indeed a realization of a photodepletion grating. A diffraction pattern recorded for these particles is shown in figure 7.7a. The results are visually very similar to those of PcH$_2$ (see figure 7.1a). This becomes also apparent when comparing the data integrated over the bottom 150 pixels ($49\,\mu\mathrm{m}$) shown in figure 7.9 with the corresponding data for PcH$_2$ in figure 7.2. However, because the photocleavable molecules are slightly more than two times as massive as

PcH_2 we assign even numbers of photon momentum recoils to these peaks (the velocities are similar in both cases because of the geometric constraints). The contrast in figures 7.9 and 7.2 is also comparable, indicating that figure 7.9 does not exhibit significant contributions from absorption (odd multiples of $\hbar k$). This already suggests that molecules might be lost after absorption instead of contributing to the signal as for PcH_2.

To analyse this data in more detail using our theoretical model, we compare the agreement with both the computation using the unconditional Talbot coefficients (5.32) and the conditional Talbot coefficients (5.35) for $l = 0$ absorptions. The latter case should correspond to a photodepletion grating with $100\ \%$ efficiency as it only considers the contributions of molecules, which have not experienced an absorption event. As mentioned at the end of section 6.4 we need to adapt our intensity distribution model in this case. For this purpose we use an initial estimate of $\sigma \approx 1 \cdot 10^{-20}\,\mathrm{m}^2$ for the absorption cross-section. This is the order of magnitude we found for PcH_2. Since the spectral properties of the photocleavable Zn-phthalocyanines are apparently similar to those of PcH_2 (see section 4.7.4) this should give us a reasonable initial estimate. The influence of including the depletion on the fit of the y distribution of the intensity is only small, giving similar values for $y_{\text{detection}}$ and w. Nevertheless this effect should be included in order to not bias the parameter sweep to the better fitting intensity distribution.

Figures 7.9 and 7.10 show the results of the parameter sweep using the conditional and unconditional Talbot coefficients respectively. For better comparability the same color scale was used for both plots. We find that for the model based on the conditional Talbot coefficient a better agreement with the experimental data is possible. In this case the parameters are also restricted to a more defined region. In contrast to this figure 7.10 shows a relatively large region in which our quantitative measure for comparing the data gives a similar level of agreement. However, it never quite reaches the values of the other model. The better description of the data given by the conditional Talbot coefficients ($l = 0$) becomes even more apparent if we directly compare the simulation data. Figure 7.7b shows a simulated diffraction pattern using this model for the optimal parameters found in figure 7.9. These optimal parameters are $\bar{\alpha} = -82.7\,\text{Å}^3 \cdot 4\pi\varepsilon_0$ and $\sigma = 2.1 \cdot 10^{-21}\,\mathrm{m}^2$. The direct interpretation of these values is however somewhat limited as it based on an idealized model assuming perfectly efficient photocleavage. As we can see from the simulation in figure 7.7b there is a good qualitative agreement with the experimental data shown in figure 7.7a. Figures 7.7c and 7.7d on the other hand show simulations results computed with the model based on the unconditional Talbot coefficients. Since the optimum is less well defined in this case we chose two exemplary parameter combinations marked in figure 7.10. We can see from these simulation results that the unconditional Talbot coefficients do not yield the peak structure we see in the experiment (figure 7.7a). In fact the diffraction pattern is practically completely washed out in this case. This agrees with our expectations since the collimation (width of the diffraction peaks) would be too broad to resolve $1\hbar k$ photon momentum recoils as was the case for the half as massive PcH_2. The fact that we still observe good contrast in the experiments gives a better match with the simulation results for the unconditional Talbot coefficients ($l = 0$). We can interpret these results as a strong indication that these molecules do indeed undergo photocleavage after absorption of $266\,\mathrm{nm}$ photons with high efficiency. We do observe that the model corresponding to a photodepletion grating gives a better explanation of our results.

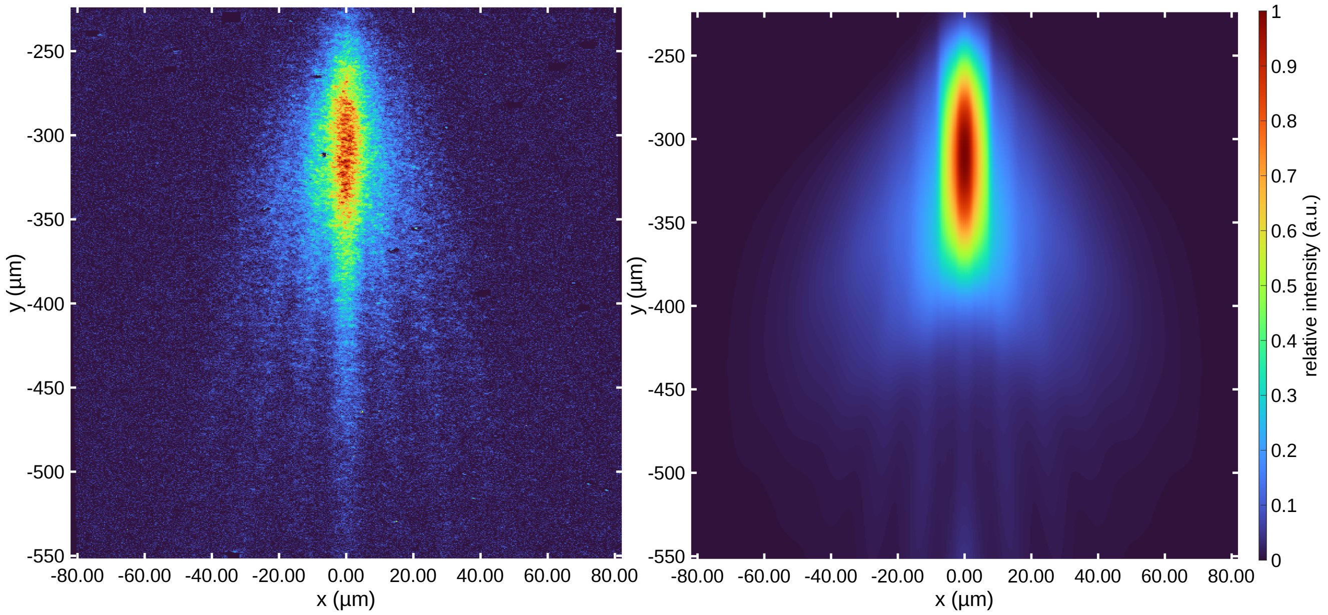

(a) Background subtracted experimental data.

(b) Simulated data with the best fitting parameters for the model using the conditional Talbot coefficients $(l = 0)$.

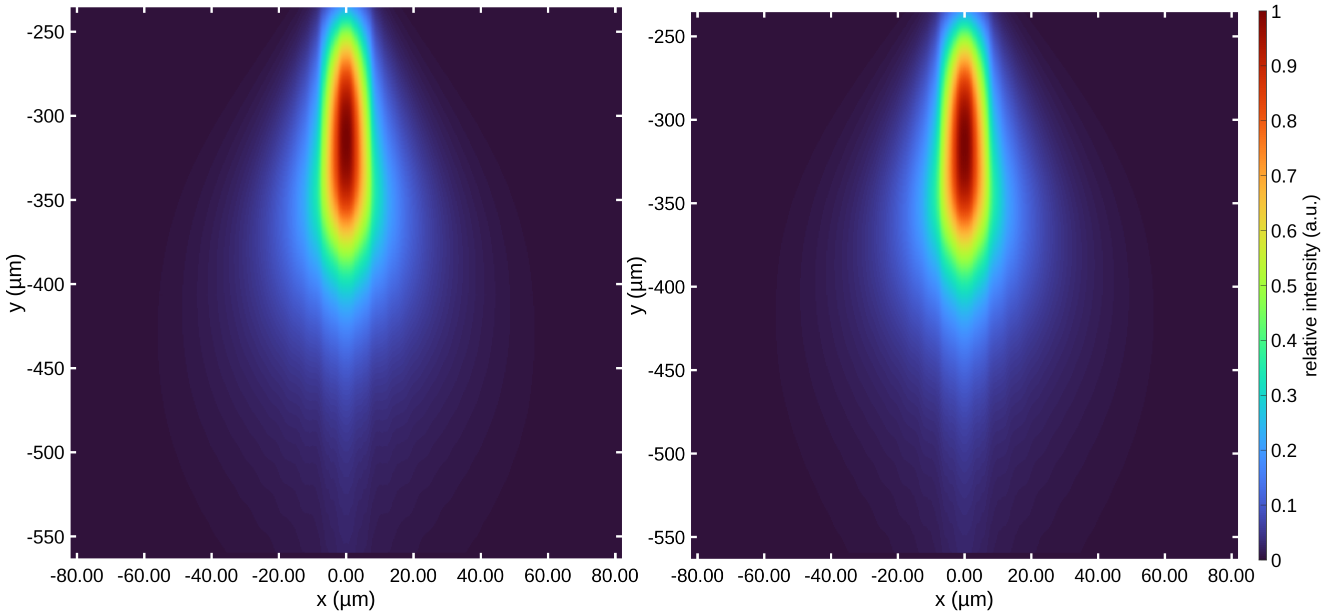

(c) Simulated data using the unconditional Talbot coefficients for point 1 in figure 7.10

(d) Simulated data using the unconditional Talbot coefficients for point 2 in figure 7.10

Figure 7.7: Comparison between experimental data with different simulation results for Zn-phthalocyanine with photocleavable tags. The joint colorbar of both images on the right shows the normalized intensity. Note that the horizontal axes of both images are stretched by a factor of two compared to the vertical axis. Only the model using the conditional Talbot coefficients shown in b can reproduce the fringes observed in the experiment.

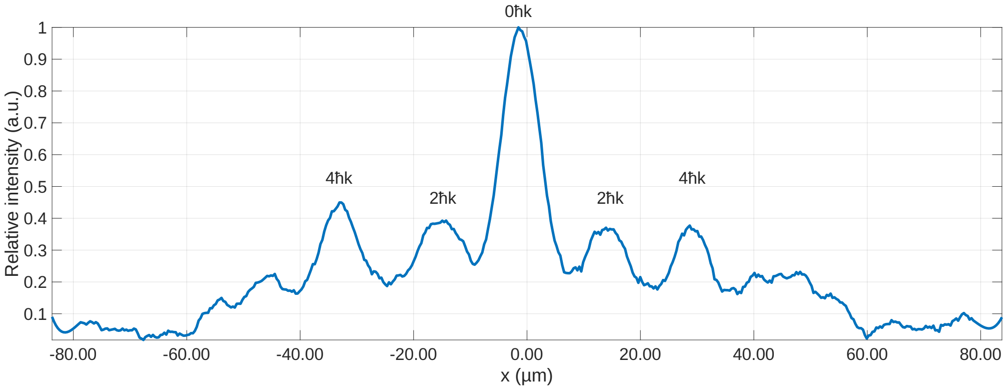

Figure 7.8: Experimental data integrated over the bottom 150 pixels in figure 7.7a. Savitzky-Golay-filtering [273] was applied to smooth the data. The photon momentum recoils $n\hbar k$ associated with the peaks are marked in the figure.

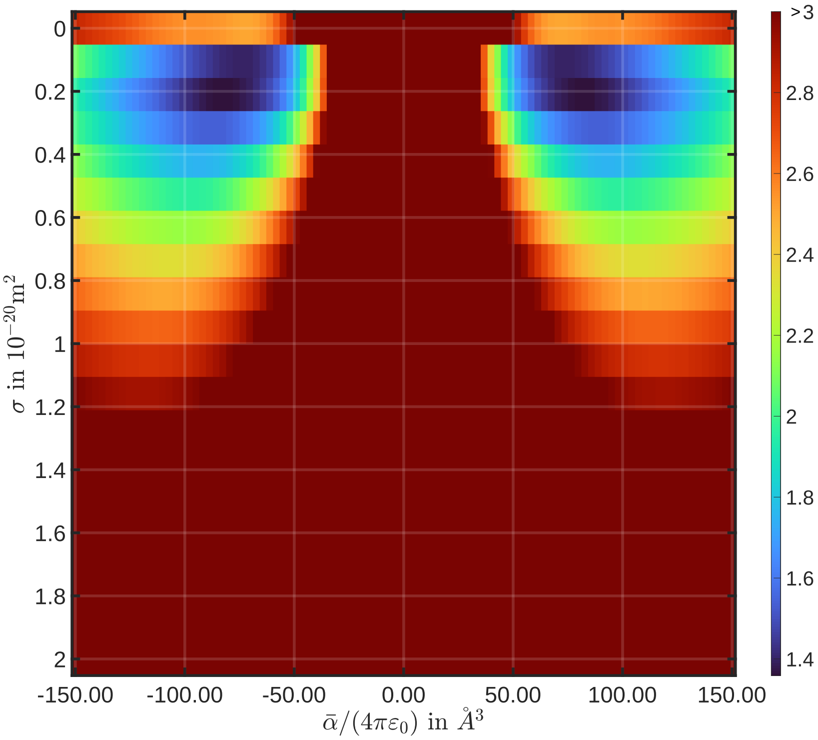

Figure 7.9: $(\bar{\alpha}, \sigma)$ parameter sweep for photocleavable Zn-phthalocyanine with conditional Talbot coefficients for $l = 0$ (5.35). The plot shows the squared differences of the experimental and simulated data summed over all pixels. The dark blue regions show the best agreement with the experimental data.

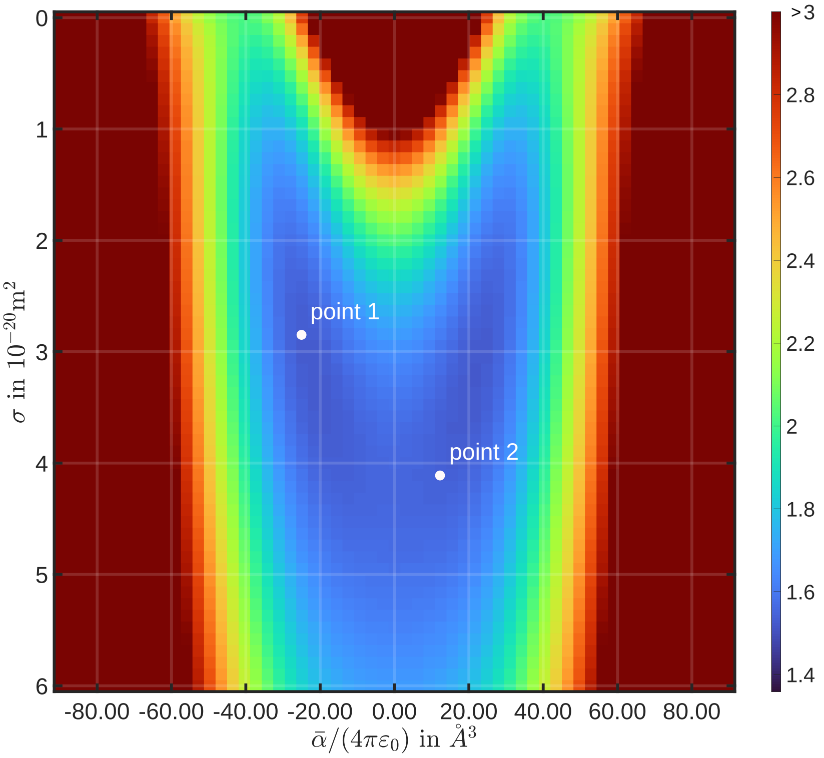

Figure 7.10: $(\bar{\alpha}, \sigma)$ parameter sweep for photocleavable Zn-phthalocyanine with unconditional Talbot coefficients (5.32). The plot shows the squared differences of the experimental and simulated data summed over all pixels. For better comparability the same color scale as in figure 7.9 is used. The two markers indicate the parameters used for the simulations shown in figures 7.7c (point 1) and 7.7d (point 2).

7.4. 6,11-dihydroxy-5,12-naphthacenedione

The data set for dihydroxy-naphthacenedione, shown in figure 7.11, is unfortunately not available with the same quality as the other molecules. We are thus somewhat limited in the knowledge oft some of the experimental constraints such as the exact laser power and heights. We can still check the consistency of our models and attempt to interpret the effects occurring for this molecules but will not be able to draw any firm conclusions about the values of the optical parameters.

In contrast to the previously described cases it was not possible to find a decent fit for w and $y_{\text{detection}}$ such that the y distribution of the intensities matches the experimental data. The most likely explanation is that the $266\,\mathrm{nm}$ laser used for fluorescence excitation in this case did not illuminate the detection region homogeneously. This would result in a bias at some heights where the intensity of the excitation laser is higher. Such an imperfect illumination is unfortunately likely in this case because of the suboptimal beam profile of the laser (see section 4.4.1) and because no SLM was available for this wavelength, which could have been used to generate a flattop profile like for the $661\,\mathrm{nm}$ detection (see section 4.6). The analysis is further complicated by the fact that because dihydroxy-naphthacenedione fluoresces after absorption of UV light at the wavelength of the grating, we would need to include this effect in the model. Fluorescence events lead to decoherence, which is not included in the Talbot coefficients presented in section 5.5. The model can be extended to treat this case, however we can then no longer write the Talbot coefficients in the relatively simple closed analytic form presented in section 5.5. The main effect of fluorescence is a reduction in contrast, caused by a background of molecules, which have undergone fluorescence events before reaching the detector [217].

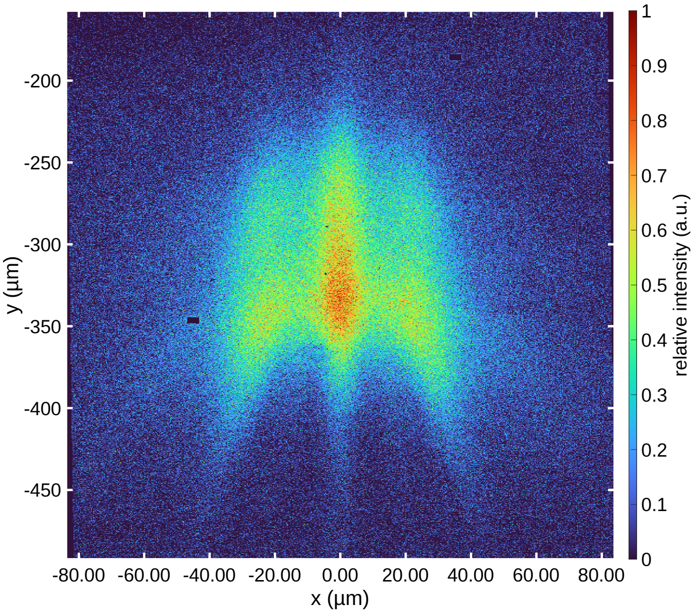

Figure 7.11: Background subtracted experimental data for dihydroxy-naphthacenedione. The colorbar shows the normalized intensity. Note that the horizontal axis is stretched by a factor of two compared to the vertical axis.

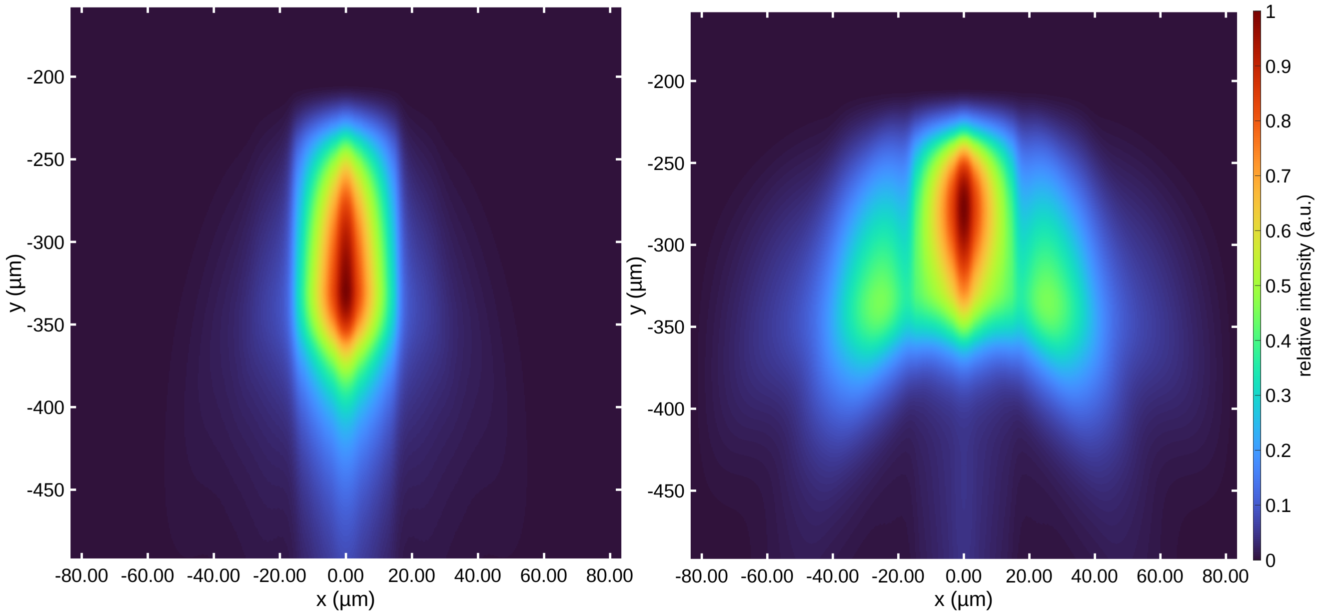

(a) $\bar{\alpha} = -10\,\mathrm{\AA}^3 \cdot 4\pi\varepsilon_0$, $\sigma = 0.1 \cdot 10^{-20}\,\mathrm{m}^2$.

(b) $\bar{\alpha} = -50\,\mathrm{\AA}^3 \cdot 4\pi\varepsilon_0$, $\sigma = 0.1 \cdot 10^{-20}\,\mathrm{m}^2$.

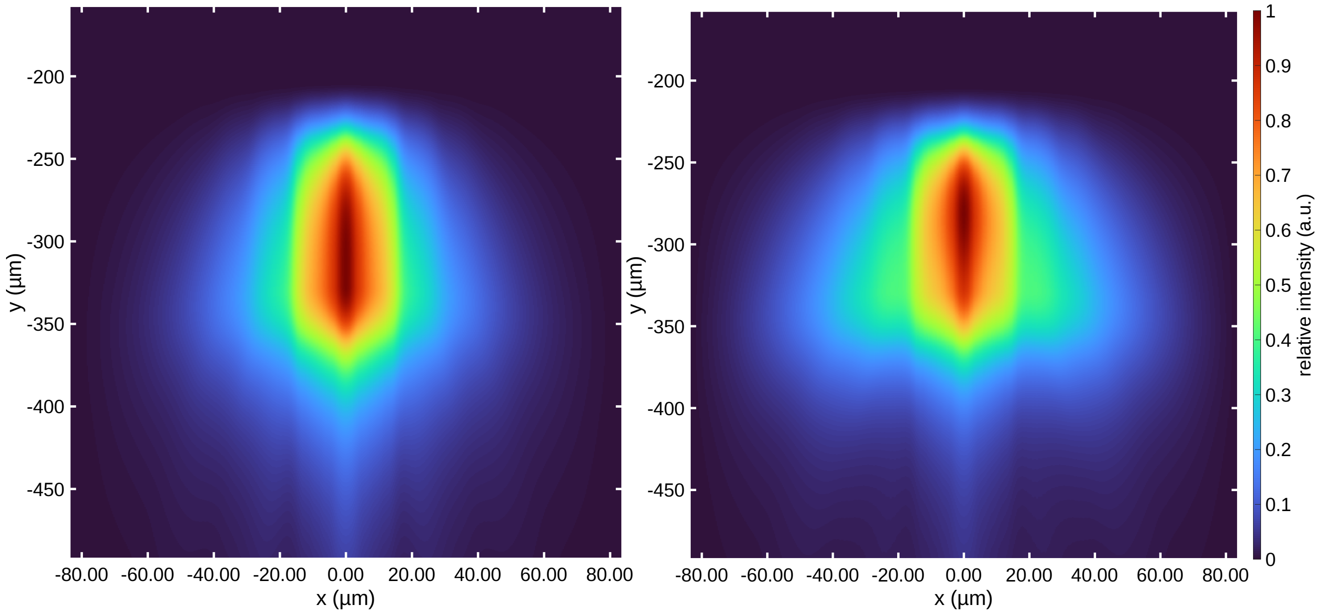

(c) $\bar{\alpha} = -10\,\mathrm{\AA}^3 \cdot 4\pi\varepsilon_0$, $\sigma = 2.0 \cdot 10^{-20}\,\mathrm{m}^2$.

(d) $\bar{\alpha} = -50\,\mathrm{\AA}^3 \cdot 4\pi\varepsilon_0$, $\sigma = 2.0 \cdot 10^{-20}\,\mathrm{m}^2$.

Figure 7.12: Comparison between simulation results for dihydroxy-naphthacenedione for a selection of parameter combinations. All simulations where run with the model based on the unconditional Talbot coefficients. The joint colorbar of both images on the right shows the normalized intensity. Note that the horizontal axes of both images are stretched by a factor of two compared to the vertical axis.

A full modelling of fluorescence by numerically evaluating the Talbot coefficients as described in [217] is beyond the scope of this thesis. Also it will most likely not improve our analysis by much in this case because of the aforementioned issues regarding the quality of this dataset. We can partially account for the loss of contrast by fluorescence by modelling it as a broadening of the diffraction peaks. This is in fact already accounted for by our procedure used to fit the slit widths $S_{1,x}$ and $S_{2,x}$ (see section 6.3). Because of the limited ability of the model to match the recorded data we restrict ourselves to a more qualitative analysis for dihydroxy-naphthacenedione. We compute diffraction patterns for a selection of combinations of $\bar{\alpha}$ and σ to study the influence of high / low contributions from phase and absorption. We use the unconditional Talbot coefficients for this simulation. Even thought we cannot find a good quantitative match with the data shown in figure 7.11, this will allow us to learn something about which effects are most relevant for the diffraction of this molecule.

We present such a selection of simulation results in figure 7.12. While none of them give an exact match for the experimental data, we can see that the distinct shape of the diffraction pattern in figure 7.11 can still be reproduced. This rather simple qualitative comparison suggests that our experimental data may be explained by dihydroxy-naphthacenedione having a comparatively low absorption cross-section and a larger polarizability. The values we used for the qualitatively best fitting simulation out of our small selection (figure 7.11 are $\bar{\alpha} = -50\,\text{Å}^3 \cdot 4\pi\varepsilon_0$ and $\sigma = 1 \cdot 10^{-21}\,\mathrm{m}^2$. Similar to TPP we could explain the lack of $1\hbar k$ peaks for this molecule with a small absorption cross-section. The polarizability being slightly larger in this case appears to be consistent with the fact that we can still observe a strong diffraction effect. Still we cannot draw any further conclusions as we cannot quantitatively match the data.

8. Conclusions & Outlook

8.1. Discussion of results

The results presented in section 7 showcase how a variety of grating effects can be relevant for diffraction of molecules. As described in section 1.1 the most relevant mechanisms here are the phase shift introduced by the dipole potential (3.14) and the effects of absorption. Our results suggest that PcH$_2$ is a molecule for which both this phase effect and photon absorption resulting in a heating of the molecule are the dominant mechanisms (a and b in figure 1.1). Both contributions are in fact of a similar order of magnitude in this case. We can estimate the relative contributions by using (5.28) and (5.30) to compute the ratio

$$R = \left| \frac{2\phi\left(x,y\right)}{\bar{n}\left(x,y\right)} \right| = \left| \frac{\bar{\alpha}}{\sigma} \cdot \frac{\omega}{\varepsilon_0 c} \right| \tag{8.1}$$

The transmission function (5.31) makes clear why this ratio allows us to judge the relative importance of the phase grating and absorption effects. Importantly the dependence on the parameters P, w_y and p_z drop out of the ratio (8.1). This means that even though our estimates for $\bar{\alpha}$ and σ given in section 7 are subject to additional uncertainties because of the variance in laser power P, this does not directly influence the quantity defined in equation (8.1). In figure 8.1 the ratio R is plotted for our selection of molecules together with the mass m. The ratios are computed from the parameters which gave the best fits to the experimental data. For dihydroxy-naphthacenedione the parameters from the simulation in figure 7.12, which gave the best qualitative agreement, are used instead. For PcH$_2$ we have $R \approx 0.5$ indicating that both phase shift and absorption are approximately equally important as already mentioned, with the absorption effect being slightly more relevant. For TPP on the other hand the standing light wave acts mainly as a phase grating as indicated by the value $R \approx 3.9$. Even though our analysis of dihydroxy-naphthacenedione was limited as described in section 7.4, we can still estimate $R \approx 15$ from the qualitative comparisons presented there. This would suggests that the effect of the polarizability is far more dominant for these molecules. However, as we also discussed in section 7.4 fluorescence is another effect which likely influences the experimental results for this molecule. While we did not include this in our model, it is possible that additional effects like this are also part of the cause for the disagreement between the simulation and the experiment in this case. We also only used a qualitative comparison to arrive at this value for dihydroxy-naphthacenedione, so our value for R given here might not fully represent the properties of the molecule. Our results for the tailored Zn-phthalocyanine indicate a different mechanisms being relevant compared to the other molecules. In this case we see a strong indication that the light-grating acts as a photocleavage grating (d in figure 1.1). For the ratio (8.1) we estimate $R \approx 11.7$ for this molecule. However, even if the influence of polarizability is larger in this sense, the cleavage process is still clearly very relevant to fully explain our results. Therefore absorption very important for the diffraction of this molecule despite the apparently large polarizability.

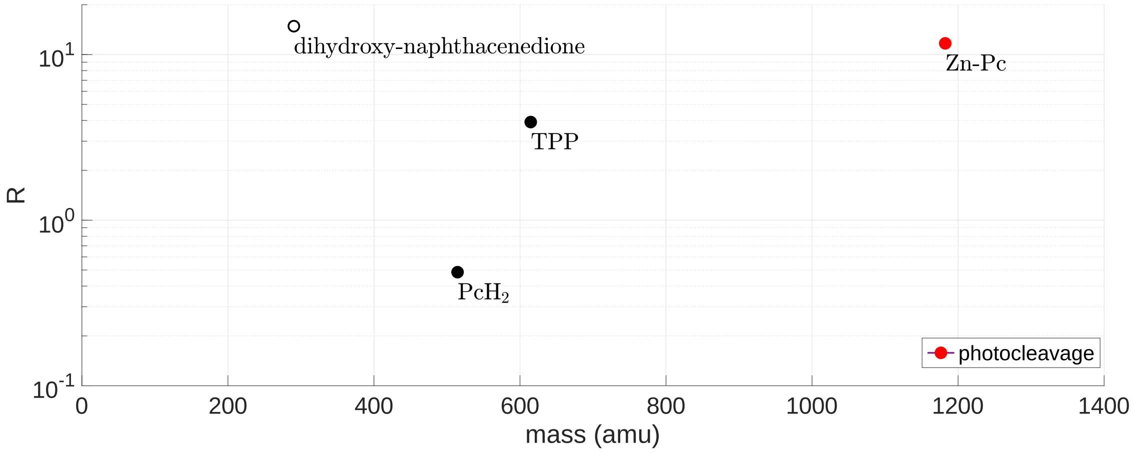

Figure 8.1: Overview of the ration R (8.1) for the molecules investigated in this work. Dihydroxy-naphthacendione is only a qualitative estimate. Zn-phthalocyanine also showed strong indication that photocleavage is a relevant effect.

8.2. Limitations & Potential improvements

While our results allows us to make some estimates about the polarizabilities and cross-sections of the molecules we tested, we can unfortunately not give concrete numerical values. The main limitation, which prevents this, is the fact that there still remain several experimental parameters which are not known with enough certainty. In particular the absolute heights of the grating and other components as well as the precise velocity distribution could only be approximated based on the experimental data. Additionally, the values of the laser power and waist radius directly influence our results for $\bar{\alpha}$ and σ. While we can give a reasonable accurate value for the waist radius, the power is not well defined because of the lack of stability of the laser. As described in section 4.4.1 the laser power drops significantly during a single measurement run, allowing us to only observe an averaged effect. The problems related to the vertical alignment can in fact also be partly attributed to the limitation of the laser. Our analysis and also our results would simplify significantly if the waist w_y of the laser could be chosen much larger, such that the y dependence of the Talbot coefficients could be neglected. This would also suppress the influence of the precise grating height y_0, which is also an unknown in the experiment. However, simply increasing the waist is not possible as the limited available laser power means that this will mean a significant reduction of the intensity in the standing light wave. As can be seen from (5.28) and (5.30) the ratio P/w_y defines the strength of the effects relevant for the diffraction. A reduction of this quantity would mean that only much weaker diffraction could be observed, which would also hinder our analysis. Nevertheless, future technological improvements might make more powerful UV lasers available in the coming years. This could solve many of the issues related to the laser in this experiment and make more accurate results possible.

Besides the issues we just discussed, we should also mention the limits introduced by the theoretical models we used. Comparison of the experimental results with the simulated diffraction patterns we covered in section 7 indicates that even for the optimal parameters we found there is still some disagreement between the two data sets. In our analysis we optimized the parameters such that the overall agreement for the whole diffraction pattern is as good as possible. However, we can see that this does not give a perfect match at all heights y. It turns out that for the given model different parameter combinations are required to give a better match at each detector height [271]. This most likely indicates some limitations in the theoretical model. Indeed there are a number of effects which might become relevant in the experiment, which the simplified model we applied here did not include.

Most importantly we did not take into account the possible change in optical properties for the excited state. If the molecule is transferred to the triple state after absorption, the polarizability and absorption cross-section might differ from the ground state values. If multiple absorption processes are relevant for the experimental results this might explain some of the discrepancies we are seeing. The ladder model we used here assumed that these values do not change in the higher states of the "ladder" [217]. Certain phthalocyanines and porphyrins are in fact known to have a much higher absorption cross-section in the triplet state. They have applications as so called optical limiters [274]. In a similar manner our model did also not include the effects of fluorescence we briefly discussed in section 7.4.

For the photocleavable Zn-phthalocyanines our model is also simplified because it implicitly assumes that the cleavage process happens with $100\ \%$ efficiency. While this still gave a good match for these molecules in our case, it might be necessary to assume an efficiency different from unity to find a better agreement with the experimental data at all detection heights. This would however also introduce another free parameter into our analysis, which is why it might still not be easy to find a much better match. However, the prospect of cleavage with a limited efficiency might shed some light onto our results for $\mathrm{PcH_2}$ and TPP. In both cases we saw that the model neglecting cleavage gave a better match with the data than the one based on the conditional Talbot coefficients. This however only tells us that $100\ \%$ efficient cleavage is no good model for the experimental data. But it is possible that we could reproduce the experimental results better if we use a model where cleavage occurs with a small non-zero probability after absorption. While it is possible that this would also result in different optimal values for $\bar{\alpha}$ and σ, it would most likely not change our order of magnitude estimate to much as the already good agreement with our existing model suggests a smaller influence of such additional effects.

Despite the shortcomings of our model we can still use our model to explain most of our results. We see both from qualitative comparisons and from our parameter estimates how the properties of the molecules result in different grating mechanisms contributing to a varying degree. Even though we are not able to give confident predictions for the numerical values of these parameters, we have still learned their order of magnitude. Importantly the limitations preventing us from giving narrower bound on these values may be resolved by advancements in technology in the future and by extending the existing theoretical model. Our results are still a proof of concept as we can clearly see that the we can tie our experimental results to certain combinations of parameters. We have also demonstrated that a photodepletion grating best explains our results for the Zn-phthalocyanines with photocleavable tags we investigated. This affirms that we have realized a photocleavage grating with these molecules.

8.3. Outlook: Photoisomerization gratings with thioindigo molecules

So far we have extensively discussed the effects of phase gratings, photon absorption leading to an increased internal temperature and photocleavage we introduced section 1.1. In this section we give a brief outlook on a specific molecule that could be used to implement another new grating mechanism: photoisomerization gratings. As discussed in section 3.2.3 the process of photoisomerization involves a molecule changing from one isomer to another after absorption of a photon. Photochromic molecules in particular then also exhibit a significant change in their spectra, which could be used to distinguish the two isomers. In an optical light grating the "switching" of one isomer to another would act like a depletion grating for the original isomer. It would be interesting to see whether the other isomer, which is formed in the grating, also exhibits interference effects and how they are realized. This would potentially give rise to interesting new phenomena. Additionally there might also be a more pronounced interplay with other effects, such as additional phase shifts from the dipole potential and multiple successive switching processes. Photochromic molecules would be useful for such applications as they could potentially be distinguished directly in fluorescence detection.

The molecule proposed here for a first set of such experiments is *thioindigo* $C_{16}H_8O_2S_2$. Thioindigo can undergo photoisomerization by rotation around its central double bond [275]. The two isomers of thioindigo are shown in figure 8.2. Successful tests with both the source and fluorescence detection used in the experimental setup have already been carried out for this molecule. Note that here a micro-focus laser evaporation source [1, 240] was used instead of the oven described in section 4.2. The mass of thioindigo $m = 296.36\,\mathrm{u}$ is also in a suitable range for the far-field setup.

The absorption spectrum of the cis-isomer is shifted by $\sim 70\,\mathrm{nm}$ to shorter wavelengths. However, both isomers show reasonable strong absorption for green visible light around $\sim 500\,\mathrm{nm}$. The thermally more stable trans-isomer has its maximum at $\sim 540\,\mathrm{nm}$ and also absorbs strongly at $532\,\mathrm{nm}$ [276–278]. This wavelength is readily available at high powers from commercial lasers, which makes the trans-cis isomerization process of thioindigo attractive for photoisomerization gratings. Particularly this would be an advantage considering the drawbacks of the limited performance of UV lasers we encountered. Photoisomerization is possible both from trans to cis and cis to trans. Measurements of the quantum yields for trans to cis isomerization are usually at the order of $0.05 - 0.1$, while the quantum yield for the reverse process is up to an order of magnitude larger. However, measurements of both show a relatively strong solvent and temperature dependence [277–279]. Besides the photochromism due to differences in the absorption spectra, thioindigo also displays different fluorescence for the two isomers. Trans-thioindigo fluoresces with an emission maximum at $\sim 585\,\mathrm{nm}$. In contrast to this cis-thioindigo has not been observed to fluoresce [280–282]. In particular the on-off switching of the fluorescence may be used to easily distinguish the isomers in the experiment as only one of them will be visible in the detection. The two isomers also differ in their electric dipole moment, which vanishes for trans-thioindigo and has been determined to be $3.44\,\mathrm{Debye}$ for cis-thioindigo [283].

Preliminary experiments have shown that exposure of thioindigo to $532\,\mathrm{nm}$ light both in flight and after deposition on the quartz detection window result in a notable loss of fluorescence signal. This may be attributed to the isomerization process, which turns the fluorescent trans-thioindigo into its non-fluorescent cis counterpart. However, several experimental challenges remain before a photoisomerization grating can be implemented. While the fact that cis-thioindigo is not directly detectable with fluorescence microscopy allows to distinguish the two isomers, it might still be necessary to record signal for both isomers in order to study the full effect of a photoisomerization grating. A possible approach might be to isomerize cis-thioindigo back into the trans-isomer. An increase in fluorescence singal would then indicate the presence of cis-thioindigo. However, so far it was not possible to succesfully do this after deposition on the quartz window. A possible reason for this might be that the cis-trans isomerization

Figure 8.2: Photoisomerization of thioindigo $C_{16}H_8O_2S_2$. The absorption of green light can change trans-thioindigo into the cis-isomer and vice versa. Both isomers absorb photons at $\lambda \sim 532\,\mathrm{nm}$. While the trans-isomer is fluorescent, the cis-isomer is not [278, 280].

process is geometrically inhibited when the molecule is adsorbed to the surface. Such effects have been observed for thioindigo on alumina surfaces [284, 285]. An alternative approach for indirectly detecting cis-thioindigo with fluorescence microscopy might be to induce a back-photoisomerization process in-flight. Because the absorption of cis-thioindigo is approximately on order of magnitude weaker at $532\,\mathrm{nm}$ than for trans-thioindigo [278] this might require a laser with a shorter wavelength.

Other complications when studying a photoisomerization grating with thioindigo might arise from the fact that even though trans-thioindigo is the more stable isomer, it is to be expected that the molecular sample used in the source contains some mixture of both isomers. Additionally it will be necessary to account for the finite quantum efficiencies of the isomerization process. While thioindigo is also attractive for such experiments because of its easy commercial availability, there are also a large number of thioindigo derivatives which have been studied for their photochromic properties [286–289]. The compatibility of thioindigo with the constraints imposed of the experiments might also suggest that some of these molecules are suitable as well, some of which might have more favorable properties.

9. Acknowledgements

Like any project, the work presented here could not have been possible without a whole team of people behind it. I want to sincerely thank everyone who supported me, worked with me and lent me advice, both during my time working on this project but also outside of it. First and foremost I want to thank my friends of collogues from the Quantumnano group in Vienna. In particular Ksenija Simonović for working on the experiment with me, teaching me how it works and how it often also does not work. Out of the current and former members of the group I also want to especially thank Christian Brand, Yaakov Fein, Stefan Gerlich and Armin Shayeghi for their helpful discussions and advice. Most importantly, however, I want to thank my supervisor, Markus Arndt, for giving me the chance to join his lab and for his support during my time there. My gratitude also goes to all our collaborators, who are involved in this project. Our chemist friends from the University of Basel, Alfredo Di Silvestro and Marcel Mayor, who made the photocleavable compound for our experiment and aided us in its analysis. I also want to thank our theory collaborators, Benjamin Stickler and Klaus Hornberger and most importantly Lukas Martinetz, who helped with the formulation of the theoretical model and are working on extending it beyond what is presented here. Finally I have to thank my family, my parents, my sister, my grandparents, for always supporting me in my studies and enabling me to take the path in life I want to choose.

Richard Ferstl

Appendices

A. Velocity selection

Consider the velocity at a fixed height y_5 given by (4.10). The physical dimensions of the source and the velocity selection slit set the restrictions $y_{0,\mathsf{max}} - \Delta y_0 \leq y_0 \leq y_{0,\mathsf{max}}$ and $y_{4,\mathsf{min}} \leq y_4 \leq y_{4,\mathsf{min}} + \Delta y_4$. The maximum and minimum velocities v_z compatible with these bounds are then

$$\begin{aligned} v_{\mathsf{max}} &= \sqrt{\frac{g}{2} \cdot \frac{z_4 z_5 \cdot (z_5 - z_4)}{y_{4,\mathsf{min}} \cdot z_5 - y_{0,\mathsf{max}} \cdot (z_5 - z_4) - y_5 \cdot z_4}} \\ v_{\mathsf{min}} &= \sqrt{\frac{g}{2} \cdot \frac{z_4 z_5 \cdot (z_5 - z_4)}{(y_{4,\mathsf{min}} + \Delta y_4) \cdot z_5 - (y_{0,\mathsf{max}} - \Delta y_0) \cdot (z_5 - z_4) - y_5 \cdot z_4}} \end{aligned} \tag{A.1}$$

Note that we assume here that the radicand appearing in (4.10) is positive for all heights in the chosen ranges. Otherwise no real velocity would be compatible with the chosen heights, i.e. it would not contribute to the final transmission. We now estimate the velocity spread as $\Delta v_z = v_{\mathsf{max}} - v_{\mathsf{min}}$. This is an approximation because the relative probability for all velocities in this range, which can be transmitted, is not equal. The two main factors contributing to this are the velocity distribution (4.2) of the source itself and the number of possible flight parabolas compatible with a particular velocity. The latter can be understood by considering that for a given y_5 different combinations of y_0 and y_4 yield the same v_z when evaluating (4.10) as long as $y_4 \cdot z_5 - y_0 \cdot (z_5 - z_4)$ remains constant. Thus velocities originating from a height interval of the width $\widetilde{\Delta y_0} = \Delta y_4 \cdot \left(\frac{z_5}{z_5 - z_4}\right)$ on the source can contribute to a particular velocity at a given detection height h_2. Under the assumption that the emission of the source is independent of y_0, this will not give different weights to different velocities in general. However, this argument is no longer true when y_0 is close to its bounds such that not the full width $\widetilde{\Delta y_0}$ can actually emit velocities. When can conclude that the relative intensities of the different velocities will fall of when approaching the limits (A.1), independently of the velocity distribution given by the source itself. This could potentially be accounted for by considering a source with the reduced size $\Delta y_0 - \widetilde{\Delta y_0}$. Another effect one might have to consider is that the horizontal collimation (see section 4.3.4) might only allow molecules emitted from a particular (relatively narrow) horizontal position to be transmitted. If this position if off-center from the circular orifice, the effective height of the source might be further reduced, as it has only its full height at the center. All these effects will however at most make the velocity spread narrower than estimated via $\Delta v_z = v_{\mathsf{max}} - v_{\mathsf{min}}$. Therefore we will continue with these approximations, thus effectively calculating a lower bound for the longitudinal coherence. Using (A.1) we compute

$$\begin{aligned} \frac{\Delta v_z}{v_{\mathsf{max}}} &= 1 - \frac{v_{\mathsf{min}}}{v_{\mathsf{max}}} \\ &= 1 - \sqrt{\frac{y_{4,\mathsf{min}} \cdot z_5 - y_{0,\mathsf{max}} \cdot (z_5 - z_4) - y_5 \cdot z_4}{(y_{4,\mathsf{min}} + \Delta y_4) \cdot z_5 - (y_{0,\mathsf{max}} - \Delta y_0) \cdot (z_5 - z_4) - y_5 \cdot z_4}} \\ &= 1 - \left(1 + \frac{\Delta y_4 \cdot z_5 + \Delta y_0 \cdot (z_5 - z_4)}{y_{4,\mathsf{min}} \cdot z_5 - y_{0,\mathsf{max}} \cdot (z_5 - z_4) - y_5 \cdot z_4}\right)^{-\frac{1}{2}} \\ &= 1 - \left(1 + \frac{2 v_{\mathsf{max}}^2}{g} \cdot \frac{\Delta y_4 \cdot z_5 + \Delta y_0 \cdot (z_5 - z_4)}{z_4 z_5 \cdot (z_5 - z_4)}\right)^{-\frac{1}{2}} \end{aligned} \tag{A.2}$$

To calculate the velocity spread relative to the mean velocity $\overline{v_z} = \frac{v_{\text{max}}+v_{\text{min}}}{2} = v_{\text{max}} - \frac{\Delta v_z}{2}$ (assuming that the distribution is approximately symmetrical) we use

$$\frac{\Delta v_z}{\overline{v_z}} = \frac{1}{\frac{v_{\text{max}}}{\Delta v_z} - \frac{1}{2}} \tag{A.3}$$

Inserting (A.2) yields

$$\begin{aligned} \frac{\Delta v_z}{\overline{v_z}} &= \left(\frac{\sqrt{r}}{\sqrt{r}-1} - \frac{1}{2}\right)^{-1} \\ &= \left(\frac{1}{2} \cdot \frac{\sqrt{r}+1}{\sqrt{r}-1}\right)^{-1} \\ &= 2 \cdot \frac{\sqrt{r}-1}{\sqrt{r}+1} \\ &= 2 \cdot \left(1 - \frac{2}{\sqrt{r}+1}\right) \end{aligned} \tag{A.4}$$

For simplicity the expression under the root in (A.2) was abbreviated as r in (A.4). After reinserting it we get equation (4.11).

B. Fiber beam profiler calibration

To further verify the accuracy of the fiber beam profiler described in section 4.4.2 the beam waist was measured at multiple positions along the beam path of a $532\,\mathrm{nm}$ laser. This was compared to measurements conducted with a *Coherent BeamMaster BM-7 (UV)* knife edge beam profiler. For this purpose the green $532\,\mathrm{nm}$ laser was redirected around the frequency doubler in figure 4.10 such that it follows the path of the $266\,\mathrm{nm}$ laser to the grating mirror GM. The green laser was used instead of the usual UV one because its better stability and beam quality should allow for a more accurate comparison between the two beam profiling methods. Instead of changing the measurement position of the beam profilers we actually translated the grating lens GL, which focuses the laser, since this turned out to be more reproducible. The divergence of the laser low enough at the location of this lens, that this should effectively be equivalent to measuring the waist at different positions along the beam propagation.

Since the knife edge beam profiler could not be placed inside the vacuum chamber in front of the grating mirror GM, where the fiber beam profiler is located, the laser was redirected using an additional mirror directly after the grating lens GL. The knife edge profiler was placed at a total distance, which was approximately the same as the distance of the fiber profiler to the grating lens. Figure B.1 shows the waist radii for different grating lens positions. The red curve is a fit of the theoretical waist radius for Gaussian beams as a function of the position z along the beam [212]:

$$w(z) = w_0 \cdot \sqrt{1 + \left(\frac{z - z_{\text{focus}}}{z_0}\right)^2} \tag{B.1}$$

z_0 is the Rayleigh range given by (4.21), which also depends on w_0. Clearly the fit matches the experimental data well. We find a minimum waist radius of

$$w_0 = (41.0 \pm 0.4)\,\mu\mathrm{m} \tag{B.2}$$

The same measurement of waist radii was repeated with the fiber beam profiler. The results are plotted in figure B.2. The figure again contains a fit (B.1) which yields a minimum waist radius

$$w_0 = (40.9 \pm 0.4)\,\mu\mathrm{m} \tag{B.3}$$

(B.2) and (B.3) clearly are in very good agreement with each other.

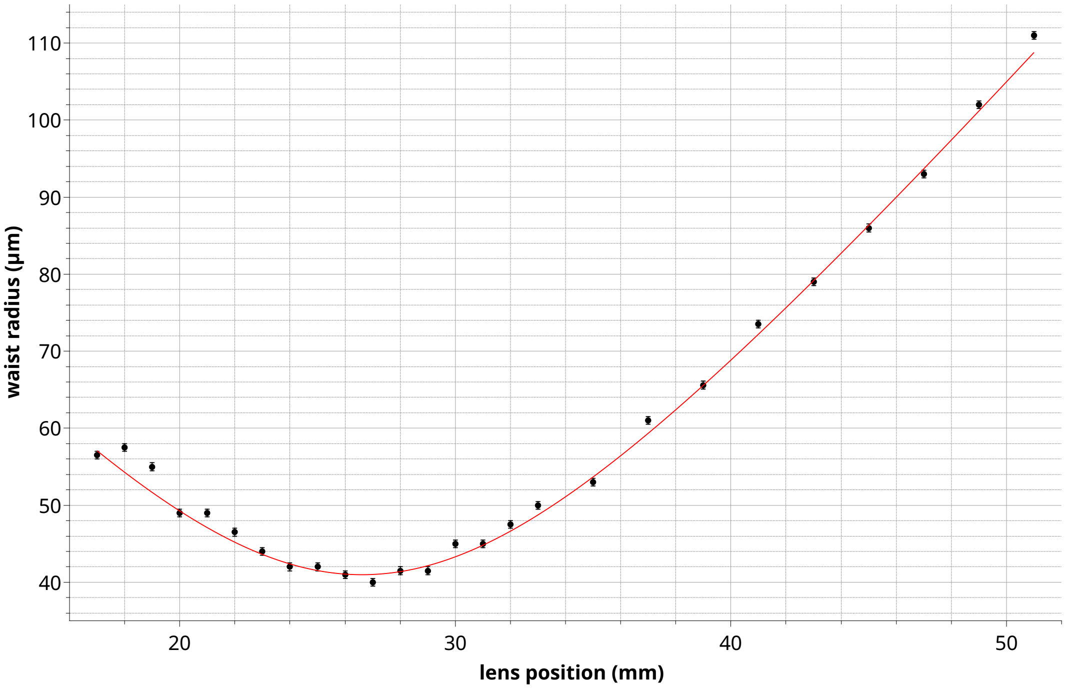

Figure B.1: Waist radius of the $532\,\mathrm{nm}$ laser for different lens positions recorded with the knife edge beam profiler. The red curve shows a fit of the form (B.1).

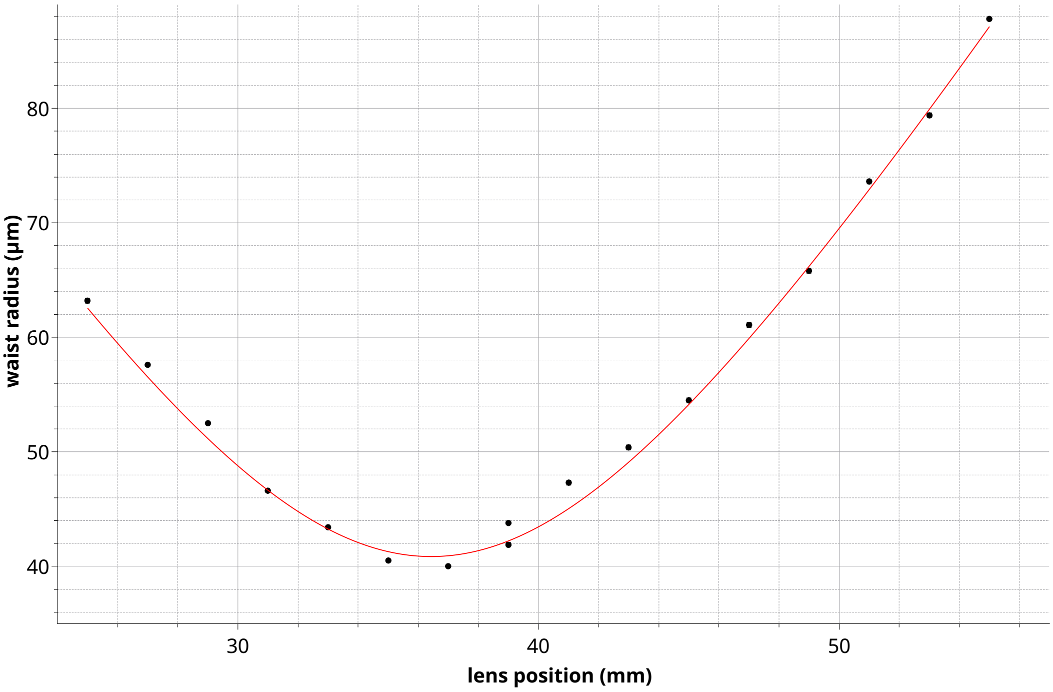

Figure B.2: Waist radius of the $532\,\mathrm{nm}$ laser for different lens positions recorded with the fiber beam profiler. The red curve shows a fit of the form (B.1).

C. Detector pixel size calibration

The physical width on the detection window corresponding to 1 pixel in the recorded images is calibrated using a *Thorlabs* R1L3S3 calibration grid. For the 20x/0.5 objective a grid width a period of $50\,\mu\mathrm{m}$ is used. We read out a distance of (760 ± 2) pixels between two edges of the grid squares $250\,\mu\mathrm{m}$ apart (see figure C.1). Therefore we can calculate that

$$1 \text{ pixel} \mathrel{\hat{=}} (0.329 \pm 0.001)\,\mu\mathrm{m} \tag{C.1}$$

The grid shown in figure C.1 is slightly rotated. We estimate the rotation to be smaller than $\theta \lesssim 10\,\mathrm{mrad}$. The correction factor introduced by this is $\cos\theta \gtrsim 1 - 5e \cdot 10^{-5}$. Which is much smaller than the uncertainty in (C.1) originating from the readout of the pixels.

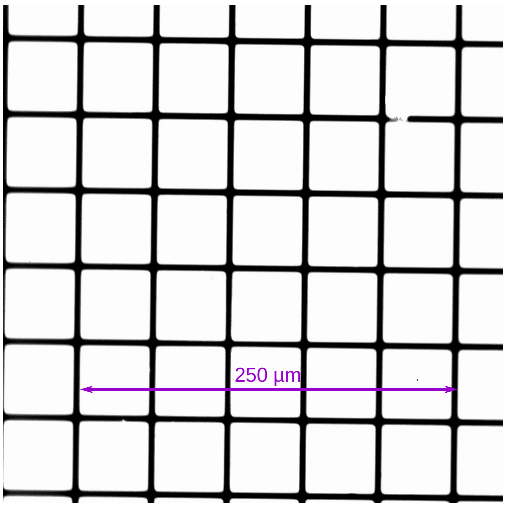

Figure C.1: $50\,\mu\mathrm{m}$ grid for the calibration of the 20x/0.5 objective. The marked distance of $250\,\mu\mathrm{m}$ is used to reference the size of a single pixel.

The image of the $50\,\mu\mathrm{m}$ grid used to calibrate the long working distance 20x/0.4 objective is shown in figure C.2. Here we read off (745 ± 2) pixels for the $250\,\mu\mathrm{m}$ distance marked in the figure. For this objective we then have

$$1 \text{ pixel} \mathrel{\hat{=}} (0.336 \pm 0.001)\,\mu\mathrm{m} \tag{C.2}$$

We estimate the rotation of the grid in figure C.2 as $\theta \approx (0.09 \pm 0.01)\,\mathrm{rad}$ giving a correction factor of $\cos\theta \approx 0.996 \pm 0.001$ in this case. The corrected pixel calibration for the long working distance objective is then

$$1 \text{ pixel} \mathrel{\hat{=}} (0.335 \pm 0.001)\,\mu\mathrm{m} \tag{C.3}$$

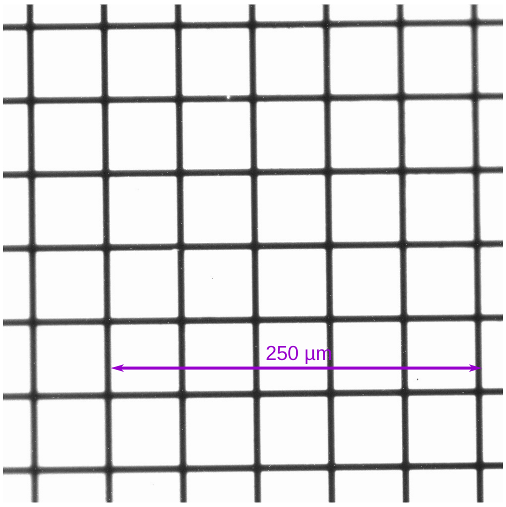

Figure C.2: $50\,\mu\mathrm{m}$ grid for the calibration of the 20x$/0.4$ long working distance objective. The marked distance of $250\,\mu\mathrm{m}$ is used to reference the size of a single pixel.

D. Supplementary information about the theoretical model

D.1. Derivation of the Wigner function description of the Far-field setup

Here we give a derivation of (5.25) based on the properties and transformations of the Wigner function discussed in section 5.1. This evaluation is based on the results of a collaboration with Lukas Martinez [271]. For notation in this section we will use the subscript of w_z and χ_z to denote the Wigner function and characteristic function at beam position z respectively. As described in section 5.1.2 we parametrize the time evolution with the longitudinal position here. To differentiate the function immediately in front of and after a slit of the grating we will use z for in front of the slit (grating) and z' for immediately after the slit (grating). We will also leave out any normalization constants in the following calculation.

We start at the source with a Wigner function

$$w_{z_0}(\mathbf{x}, \mathbf{p}) = \theta\left(\frac{D_S}{2} - |x|\right) \cdot \theta\left(\frac{D_S}{2} - |y|\right) \cdot \mu_y(p_y) \tag{D.1}$$

This approximates the source as rectangular instead of circular. However, this should not be a problem as the collimation slits $S_{1,x}$ and $S_{2,x}$ strongly restrict the relevant x coordinates, so we can assume the y extension of the source to be independent of x. Also as mentioned in section 5.4 we assume a constant momentum (velocity) distribution in x direction. We leave the corresponding distribution $\mu_y(p_y)$ unspecified for now.

Free evolution to the first slit $S_{1,x}$ via (5.7) yields

$$w_{z_1}(\mathbf{x}, \mathbf{p}) = \theta\left(\frac{D_S}{2} - \left|x - p_x \frac{\Delta z_{10}}{p_z}\right|\right) \cdot \theta\left(\frac{D_S}{2} - \left|y - p_y \frac{\Delta z_{10}}{p_z} - \frac{g m^2 \Delta z_{10}^2}{2 p_z^2}\right|\right) \cdot \mu_y\left(p_y + \frac{g m^2 \Delta z_{10}}{p_z}\right) \tag{D.2}$$

We now consider the effect of the collimator $S_{1,x}$ classically by the means of (5.24). We further assume that both the slit width $S_{1,x}$ and $p_x \frac{\Delta z_{10}}{p_z}$ (for relevant p_x) are much smaller than D_S. Then

$$w_{z_1'}\left(\mathbf{x},\mathbf{p}\right) = \theta\left(\frac{S_{1,x}}{2} - |x|\right) \cdot \theta\left(\frac{D_S}{2} - \left| y - p_y \frac{\Delta z_{10}}{p_z} - \frac{g m^2 \Delta z_{10}^2}{2 p_z^2} \right|\right) \cdot \mu_y\left(p_y + \frac{g m^2 \Delta z_{10}}{p_z}\right) \tag{D.3}$$

It is convenient to now go to a characteristic function picture using (5.3). We write

$$\chi_{z_1'}\left(\mathbf{s},\mathbf{q}\right) = \delta\left(s_x\right) \cdot \operatorname{sinc}\left(\frac{q_x S_{1,x}}{2\hbar}\right) \cdot \chi^{(y)}_{z_1'}\left(s_y, q_y\right) \tag{D.4}$$

Here we introduced the shorthand notation

$$\begin{aligned} \chi^{(y)}_{z_1'}\left(s_y, q_y\right) = & \iint_{\mathbb{R}} \mathrm{d}y \ \left[\mathrm{d}p_y \ \exp\left\{i \frac{q_y y - s_y p_y}{\hbar}\right\} \cdot \theta\left(\frac{D_S}{2} - \left| y - p_y \frac{\Delta z_{10}}{p_z} - \frac{g m^2 \Delta z_{10}^2}{2 p_z^2} \right|\right) \cdot \right. \\ & \left. \cdot \ \mu_y\left(p_y + \frac{g m^2 \Delta z_{10}}{p_z}\right)\right] \\ = & \iint_{\mathbb{R}} \mathrm{d}y \ \mathrm{d}p_y \ \exp\left\{i \frac{q_y y - s_y p_y}{\hbar}\right\} \cdot w^{(y)}_{z_1'}\left(y, p_y\right) \end{aligned} \tag{D.5}$$

This corresponds to the characteristic function of just the y part of the Wigner function. In this case both degrees of freedom are still decoupled. We evolve (D.4) to the next slit $S_{2,x}$ via (5.8):

$$\begin{aligned} \chi_{z_2}\left(\mathbf{s},\mathbf{q}\right) = & \delta\left(s_x - \frac{q_x \Delta z_{21}}{p_z}\right) \cdot \operatorname{sinc}\left(\frac{q_x S_{1,x}}{2\hbar}\right) \cdot \chi^{(y)}_{z_1'}\left(s_y - \frac{q_y \Delta z_{21}}{p_z}, q_y\right) \cdot \\ & \cdot \exp\left\{-i \frac{g m^2 \Delta z_{21}}{\hbar p_z} \cdot \left(\frac{q_y \Delta z_{21}}{2 p_z} - s_y\right)\right\} \end{aligned} \tag{D.6}$$

The second slit $S_{2,x}$ is now treated without the classical approximation. We convolve (D.6) with the corresponding transmission kernel for the characteristic function (5.23). The result is

$$\begin{aligned} \chi_{z_2'}\left(\mathbf{s},\mathbf{q}\right) = & \frac{p_z}{\Delta z_{21}} \cdot \theta\left(S_{2,x} - |s_x|\right) \cdot \left(S_{2,x} - |s_x|\right) \cdot \operatorname{sinc}\left(\frac{s_x S_{1,x} p_z}{2\hbar \Delta z_{21}}\right) \cdot \operatorname{sinc}\left(\frac{\left(S_{2,x} - |s_x|\right) \cdot \left(q_x - \frac{s_x p_z}{\Delta z_{21}}\right)}{2\hbar}\right) \cdot \\ & \cdot \chi^{(y)}_{z_1'}\left(s_y - \frac{q_y \Delta z_{21}}{p_z}, q_y\right) \cdot \exp\left\{-i \frac{g m^2 \Delta z_{21}}{\hbar p_z} \cdot \left(\frac{q_y \Delta z_{21}}{2 p_z} - s_y\right)\right\} \\ = & \chi^{(x)}_{z_2'}\left(s_x, q_x\right) \cdot \chi^{(y)}_{z_1'}\left(s_y - \frac{q_y \Delta z_{21}}{p_z}, q_y\right) \cdot \exp\left\{-i \frac{g m^2 \Delta z_{21}}{\hbar p_z} \cdot \left(\frac{q_y \Delta z_{21}}{2 p_z} - s_y\right)\right\} \end{aligned} \tag{D.7}$$

In the last line we introduced another shorthand notation

$$\chi^{(x)}_{z_2'}\left(s_x, q_x\right) = \frac{p_z}{\Delta z_{21}} \cdot \theta\left(S_{2,x} - |s_x|\right) \cdot \left(S_{2,x} - |s_x|\right) \cdot \operatorname{sinc}\left(\frac{s_x S_{1,x} p_z}{2\hbar \Delta z_{21}}\right) \cdot \operatorname{sinc}\left(\frac{\left(S_{2,x} - |s_x|\right) \cdot \left(q_x - \frac{s_x p_z}{\Delta z_{21}}\right)}{2\hbar}\right) \tag{D.8}$$

We freely evolve (D.8) further to z_3, the location of the grating.

$$\chi_{z_3}\left(\mathbf{s},\mathbf{q}\right) = \chi^{(x)}_{z_2'}\left(s_x - \frac{q_x \Delta z_{32}}{p_z}, q_x\right) \cdot \chi^{(y)}_{z_1'}\left(s_y - \frac{q_y \Delta z_{31}}{p_z}, q_y\right) \cdot \exp\left\{-i \frac{g m^2 \Delta z_{31}}{\hbar p_z} \cdot \left(\frac{q_y \Delta z_{31}}{2 p_z} - s_y\right)\right\} \tag{D.9}$$

As discussed in section 5.2 the effect of the grating is described by (5.16) with the aid of the Talbot coefficients $B_n\left(\frac{s_x}{d}, y\right)$. Thus (D.9) transforms to

$$\begin{aligned}\chi_{z_3'}\left(\mathbf{s},\mathbf{q}\right) = \sum_{n\in\mathbb{Z}} &\chi^{(x)}_{z_2'}\left(s_x - \frac{\left(q_x + \frac{2\pi\hbar}{d}n\right)\Delta z_{32}}{p_z}, q_x + \frac{2\pi\hbar}{d}n\right)\cdot \\ &\cdot \iint_{\mathbb{R}} \mathrm{d}y\ \mathrm{d}\widetilde{q}_y\ \left[\exp\left\{i\frac{\left(q_y - \widetilde{q}_y\right)y}{\hbar}\right\}\chi^{(y)}_{z_1'}\left(s_y - \frac{q_y\Delta z_{31}}{p_z}, q_y\right)\cdot\right. \\ &\left.\cdot\exp\left\{-i\frac{gm^2\Delta z_{31}}{\hbar p_z}\cdot\left(\frac{q_y\Delta z_{31}}{2p_z} - s_y\right)\right\}\cdot B_n\left(\frac{s_x}{d}, y\right)\right]\end{aligned} \tag{D.10}$$

As discussed in section 5.2 already the s_y dependence of the Talbot coefficients is neglected. We now return to the Wigner function by transforming the characteristic function back. This is achieved by simply applying the inverse Fourier transforms from (5.3). The result is

$$\begin{aligned}w_{z_3'}\left(\mathbf{x},\mathbf{p}\right) = \sum_{n\in\mathbb{Z}}\iint_{\mathbb{R}} \mathrm{d}q_x\ \mathrm{d}s_x\ &\left[\exp\left\{i\frac{p_x s_x - q_x x}{\hbar}\right\}\cdot\chi^{(x)}_{z_2'}\left(s_x - \frac{\left(q_x + \frac{2\pi\hbar}{d}n\right)\Delta z_{32}}{p_z}, q_x + \frac{2\pi\hbar}{d}n\right)\right. \\ &\left.\cdot\ w^{(y)}_{z_3}\left(y, p_y\right)\cdot B_n\left(\frac{s_x}{d}, y\right)\right]\end{aligned} \tag{D.11}$$

Here we introduced the function

$$w^{(y)}_{z_3}\left(y, p_y\right) = \theta\left(\frac{D_S}{2} - \left|y - p_y\frac{\Delta z_{30}}{p_z} - \frac{gm^2\Delta z_{30}^2}{2p_z^2}\right|\right)\cdot\mu_y\left(p_y + \frac{gm^2\Delta z_{30}}{p_z}\right) \tag{D.12}$$

To see this simply note that the expression at the end of the second line in (D.10) is simply the free evolution (5.8) of the characteristic function (D.5). The next step is the free evolution of (D.11) to the location of the velocity selector S_y at z_4.

$$\begin{aligned}w_{z_4}\left(\mathbf{x},\mathbf{p}\right) = \sum_{n\in\mathbb{Z}}\iint_{\mathbb{R}} \mathrm{d}q_x\ \mathrm{d}s_x\ &\left[\exp\left\{i\frac{p_x s_x - q_x x}{\hbar}\right\}\cdot\right. \\ &\cdot\ \chi^{(x)}_{z_2'}\left(s_x - \frac{\left(q_x + \frac{2\pi\hbar}{d}n\right)\Delta z_{32}}{p_z} - \frac{q_x\Delta z_{43}}{p_z}, q_x + \frac{2\pi\hbar}{d}n\right) \\ &\cdot\ w^{(y)}_{z_3}\left(y - \frac{p_y\Delta z_{43}}{p_z} - \frac{gm^2\Delta z_{43}^2}{2p_z^2}, p_y + \frac{gm^2\Delta z_{43}}{p_z}\right)\cdot \\ &\left.\cdot\ B_n\left(\frac{s_x - \frac{q_x\Delta z_{43}}{p_z}}{d}, y - \frac{p_y\Delta z_{43}}{p_z} - \frac{gm^2\Delta z_{43}^2}{2p_z^2}\right)\right]\end{aligned} \tag{D.13}$$

Since there has been no collimation in the y direction so far we assume sufficient incoherence in that direction to justify also approximating this slit with the classical transformation (5.24). We also introduce the vertical position y_{S_y} of the slit as a free parameter.

$$\begin{aligned}w_{z_4'}\left(\mathbf{x},\mathbf{p}\right) = \sum_{n\in\mathbb{Z}}\iint_{\mathbb{R}} \mathrm{d}q_x\ \mathrm{d}s_x\ &\left[\exp\left\{i\frac{p_x s_x - q_x x}{\hbar}\right\}\cdot\right. \\ &\cdot\ \chi^{(x)}_{z_2'}\left(s_x - \frac{\left(q_x + \frac{2\pi\hbar}{d}n\right)\Delta z_{32}}{p_z} - \frac{q_x\Delta z_{43}}{p_z}, q_x + \frac{2\pi\hbar}{d}n\right) \\ &\cdot\ w^{(y)}_{z_3}\left(y - \frac{p_y\Delta z_{43}}{p_z} - \frac{gm^2\Delta z_{43}^2}{2p_z^2}, p_y + \frac{gm^2\Delta z_{43}}{p_z}\right)\cdot \\ &\left.\cdot\ B_n\left(\frac{s_x - \frac{q_x\Delta z_{43}}{p_z}}{d}, y - \frac{p_y\Delta z_{43}}{p_z} - \frac{gm^2\Delta z_{43}^2}{2p_z^2}\right)\cdot\theta\left(\frac{S_y}{2} - \left|y - y_{S_y}\right|\right)\right]\end{aligned} \tag{D.14}$$

Finally we apply another free evolution to our detector at z_5.

$$\begin{aligned}
w_{z_5}(\mathbf{x},\mathbf{p}) = \sum_{n\in\mathbb{Z}} \iint_{\mathbb{R}} \mathrm{d}q_x \ \mathrm{d}s_x \ \Bigg[& \exp\left\{ i\frac{p_x s_x - q_x x}{\hbar} \right\} \cdot \\
& \cdot \chi^{(x)}_{z_2'}\left(s_x - \frac{\left(q_x + \frac{2\pi\hbar}{d} n\right)\Delta z_{32}}{p_z} - \frac{q_x \Delta z_{53}}{p_z}, q_x + \frac{2\pi\hbar}{d} n \right) \\
& \cdot w^{(y)}_{z_3}\left(y - \frac{p_y \Delta z_{53}}{p_z} - \frac{g m^2 \Delta z_{53}^2}{2p_z^2}, p_y + \frac{g m^2 \Delta z_{53}}{p_z} \right) \cdot \\
& \cdot B_n\left(\frac{s_x - \frac{q_x \Delta z_{53}}{p_z}}{d}, y - \frac{p_y \Delta z_{53}}{p_z} - \frac{g m^2 \Delta z_{53}^2}{2p_z^2} \right) \cdot \\
& \cdot \theta\left(\frac{S_y}{2} - \left| y - y_{S_y} - \frac{p_y \Delta z_{54}}{p_z} - \frac{g m^2 \Delta z_{54}^2}{2p_z^2} \right| \right) \Bigg]
\end{aligned} \tag{D.15}$$

The compute the flux at the detector we must first compute the marginal distributions by integrating (D.15) over p_x and p_y according to (5.2). We must also integrate over the distribution of the forward velocities (4.3). The result is

$$\begin{aligned}
j(\mathbf{x}) = \sum_{n\in\mathbb{Z}} \int_{\mathbb{R}^+} \mathrm{d}p_z \iint_{\mathbb{R}} \mathrm{d}q_x \ \mathrm{d}p_y \ \Bigg[& \exp\left\{ -i\frac{q_x x}{\hbar} \right\} \cdot \mu_z(p_z) \\
& \cdot \chi^{(x)}_{z_2'}\left(-\frac{\frac{2\pi\hbar}{d} n \Delta z_{32}}{p_z} - \frac{q_x \Delta z_{52}}{p_z}, q_x + \frac{2\pi\hbar}{d} n \right) \\
& \cdot \theta\left(\frac{D_S}{2} - \left| y - p_y \frac{\Delta z_{50}}{p_z} - \frac{g m^2 \Delta z_{50}^2}{2p_z^2} \right| \right) \cdot \mu_y\left(p_y + \frac{g m^2 \Delta z_{50}}{p_z} \right) \cdot \\
& \cdot B_n\left(-\frac{q_x \Delta z_{53}}{p_z d}, y - \frac{p_y \Delta z_{53}}{p_z} - \frac{g m^2 \Delta z_{53}^2}{2p_z^2} \right) \cdot \\
& \cdot \theta\left(\frac{S_y}{2} - \left| y - y_{S_y} - \frac{p_y \Delta z_{54}}{p_z} - \frac{g m^2 \Delta z_{54}^2}{2p_z^2} \right| \right) \Bigg]
\end{aligned} \tag{D.16}$$

With the definition

$$\mu_z(p_z) = p_z \cdot \exp\left\{ -\frac{(p_z - p_w)^2}{2 m k_B T} \right\} \tag{D.17}$$

In analogy to (4.3). The additional factor p_z^2 in (4.3) originates from the integration over a finite solid angle element. This is already inherently contained in the above computation which is why we do not include the factor here. The reaming factor p_z shows up because our detector is integrating the flux of the molecules. Note that we also do not consider normalization factors here. In (D.16) we also reinserted the expression (D.12). The final expression (D.16) is equation (5.25).

D.2. Symmetry properties of the Talbot coefficients

The unconditional Talbot coefficients (5.32) and the zero photon absorption ($l = 0$) conditional Talbot coefficients (5.35) both possess a useful symmetry property:

$$B_n\left(\xi, y\right) = B_{-n}\left(-\xi, y\right) \tag{D.18}$$

To show this we make use of the following properties of the Bessel function for integer n [290]:

$$J_{-n}\left(x\right) = \left(-1\right)^n \cdot J_n\left(x\right) = J_n\left(-x\right) \tag{D.19}$$

We also use the relation [217]

$$\left(\frac{u-v}{u+v}\right)^{-\frac{n}{2}} \cdot \operatorname{sgn}\left(u+v\right)^n = \left(\frac{u+v}{u-v}\right)^{\frac{n}{2}} \cdot \operatorname{sgn}\left(u-v\right)^n \tag{D.20}$$

for $u, v \in \mathbb{R}, n \in \mathbb{Z}$. The relation is trivial for $\operatorname{sgn}\left(u+v\right)^n = \operatorname{sgn}\left(u-v\right)^n$. If this is not the case the fractions on both sides become negative and exponentiation by $\pm\frac{n}{2}$ gives different results depending on which principal branch we are on.

We can now prove (D.18) for the case (5.32). According to (5.33) and (5.34) exchanging $\xi \to -\xi$ corresponds to replacing $\zeta_{\mathsf{coh}} \to -\zeta_{\mathsf{coh}}$.

$$\begin{aligned}
B_{-n}\left(-\xi, y\right) &= e^{-\zeta'_{\mathsf{abs}}} \left(\frac{-\zeta_{\mathsf{coh}} + \zeta'_{\mathsf{abs}}}{-\zeta_{\mathsf{coh}} - \zeta'_{\mathsf{abs}}}\right)^{-\frac{n}{2}} \cdot J_{-n}\left(\operatorname{sgn}\left(-\zeta_{\mathsf{coh}} - \zeta'_{\mathsf{abs}}\right)\sqrt{\zeta_{\mathsf{coh}}^2 - \zeta'^2_{\mathsf{abs}}}\right) \\
&= e^{-\zeta'_{\mathsf{abs}}} \left(\frac{\zeta_{\mathsf{coh}} - \zeta'_{\mathsf{abs}}}{\zeta_{\mathsf{coh}} + \zeta'_{\mathsf{abs}}}\right)^{-\frac{n}{2}} \cdot \operatorname{sgn}\left(\zeta_{\mathsf{coh}} + \zeta'_{\mathsf{abs}}\right)^n \cdot J_n\left(\sqrt{\zeta_{\mathsf{coh}}^2 - \zeta'^2_{\mathsf{abs}}}\right) \\
&= e^{-\zeta'_{\mathsf{abs}}} \left(\frac{\zeta_{\mathsf{coh}} + \zeta'_{\mathsf{abs}}}{\zeta_{\mathsf{coh}} - \zeta'_{\mathsf{abs}}}\right)^{\frac{n}{2}} \cdot \operatorname{sgn}\left(\zeta_{\mathsf{coh}} - \zeta'_{\mathsf{abs}}\right)^n \cdot J_n\left(\sqrt{\zeta_{\mathsf{coh}}^2 - \zeta'^2_{\mathsf{abs}}}\right) \\
&= e^{-\zeta'_{\mathsf{abs}}} \left(\frac{\zeta_{\mathsf{coh}} + \zeta'_{\mathsf{abs}}}{\zeta_{\mathsf{coh}} - \zeta'_{\mathsf{abs}}}\right)^{\frac{n}{2}} \cdot J_n\left(\operatorname{sgn}\left(\zeta_{\mathsf{coh}} - \zeta'_{\mathsf{abs}}\right)\sqrt{\zeta_{\mathsf{coh}}^2 - \zeta'^2_{\mathsf{abs}}}\right) = B_n\left(\xi, y\right)
\end{aligned} \tag{D.21}$$

Similarly we can treat the case (5.35):

$$\begin{aligned}
B_{-n}\left(-\xi, y; l=0\right) &= e^{-\frac{\bar{n}_0}{2}} \left(\frac{-\zeta_{\mathsf{coh}} - \zeta_{\mathsf{abs}}}{-\zeta_{\mathsf{coh}} + \zeta_{\mathsf{abs}}}\right)^{-\frac{n}{2}} \cdot J_{-n}\left(\operatorname{sgn}\left(-\zeta_{\mathsf{coh}} + \zeta_{\mathsf{abs}}\right)\sqrt{\zeta_{\mathsf{coh}}^2 - \zeta_{\mathsf{abs}}^2}\right) \\
&= e^{-\frac{\bar{n}_0}{2}} \left(\frac{\zeta_{\mathsf{coh}} + \zeta_{\mathsf{abs}}}{\zeta_{\mathsf{coh}} - \zeta_{\mathsf{abs}}}\right)^{-\frac{n}{2}} \cdot \operatorname{sgn}\left(\zeta_{\mathsf{coh}} - \zeta_{\mathsf{abs}}\right)^n \cdot J_n\left(\sqrt{\zeta_{\mathsf{coh}}^2 - \zeta_{\mathsf{abs}}^2}\right) \\
&= e^{-\frac{\bar{n}_0}{2}} \left(\frac{\zeta_{\mathsf{coh}} - \zeta_{\mathsf{abs}}}{\zeta_{\mathsf{coh}} + \zeta_{\mathsf{abs}}}\right)^{\frac{n}{2}} \cdot \operatorname{sgn}\left(\zeta_{\mathsf{coh}} + \zeta_{\mathsf{abs}}\right)^n \cdot J_n\left(\sqrt{\zeta_{\mathsf{coh}}^2 - \zeta_{\mathsf{abs}}^2}\right) \\
&= e^{-\frac{\bar{n}_0}{2}} \left(\frac{\zeta_{\mathsf{coh}} - \zeta_{\mathsf{abs}}}{\zeta_{\mathsf{coh}} + \zeta_{\mathsf{abs}}}\right)^{\frac{n}{2}} \cdot J_n\left(\operatorname{sgn}\left(\zeta_{\mathsf{coh}} + \zeta_{\mathsf{abs}}\right)\sqrt{\zeta_{\mathsf{coh}}^2 - \zeta_{\mathsf{abs}}^2}\right) = B_n\left(\xi, y; l=0\right)
\end{aligned} \tag{D.22}$$

Finally we can also infer from (D.22) that (D.16) holds for the conditional Talbot coefficients with $l = 1$ as defined in (5.37). This can easily be seen because all factorial pre factors are equal to 1 in this case. We then just need to relabel the sum $m \to k - m$ and arrive at the desired result:

$$\begin{aligned}
B_n\left(-\xi, y; l=1\right) &= \sum_{k=0}^{1}\sum_{m=0}^{k}\left(\frac{\bar{n}_0}{4}\right)^k \cdot \zeta_{\mathsf{abs}}^{1-k} \cdot B_{-n+k-2m}\left(\zeta, y; l=0\right) \\
&= \sum_{k=0}^{1}\sum_{m=0}^{k}\left(\frac{\bar{n}_0}{4}\right)^k \cdot \zeta_{\mathsf{abs}}^{1-k} \cdot B_{-n-k+2m}\left(\zeta, y; l=0\right) = B_{-n}\left(\xi, y; l=1\right)
\end{aligned} \tag{D.23}$$

The property (D.18) is useful because it implies that the integrand in (D.16) is symmetric under exchange of $q_x \leftrightarrow -q_x$ *after* summing over all n. This means that the Fourier transform of the flux is symmetric in q_x and we can simplify the computation described in section 6 by only evaluating the cases $q_x \geq 0$. This symmetry can easily be seen by recognizing that q_x and n only appear in the Talbot coefficients $B_n\left(\xi, \tilde{y}\right)$ and the function $\chi^{(x)}_{z_2'}\left(s_x, \tilde{q}_x\right)$ in (D.16). $\chi^{(x)}_{z_2'}\left(s_x, \tilde{q}_x\right)$ defined in (D.8) is clearly symmetric if both its argument change their sign $\left(\tilde{q}_x, s_x \to -\tilde{q}_x, -s_x\right)$. Therefore $\chi^{(x)}_{z_2'}\left(s_x, \tilde{q}_x\right)$ appearing in (D.16) is also symmetric under simultaneous exchange of $q_x, n \to -q_x, -n$. The same is true for the Talbot coefficients as a consequence of (D.18). Thus the whole integrand shares this symmetry. Because we are summing over all $n \in \mathbb{Z}$ we can simply relabel the summation index $n \to -n$ and the expression becomes symmetric in $q_x \leftrightarrow -q_x$.

The Talbot coefficients presented here also have the useful property that they are always real. For (5.32) this is only non-trivial for the case $\zeta_{\mathsf{coh}} < \zeta_{\mathsf{abs}'}$. Then the argument of the Bessel function is imaginary. For purely imaginary x $J_n(x)$ is real for n even and imaginary for n odd. Similarly the prefactor raised to the power of $\frac{n}{2}$ is imaginary for only odd n and real otherwise. Thus the product in (5.32) is always real. A similar argument can be made for (5.35). (5.37) is then also obviously real.

List of Figures

List of Tables

Acronyms

BBO	barium borate	28, 32
BP	band pass	45
cw	continuous wave	2
DFT	density-functional theory	11
GHZ	Greenberger-Horne-Zeilinger	5
HV	high vacuum	18
IVR	intramolecular vibrational randomization	13
KDTLI	Kapitza–Dirac–Talbot–Lau interferometer	6
LBO	lithium triborate	28
LIF	laser-induced fluorescence	17
MOT	magneto-optical trap	6
PcH$_2$	phthalocyanine $C_{32}H_{18}N_8$	42, 46
PBS	polarizing beam splitter	28, 29
PPG	photoremovable protecting group	15
REMPI	resonance-enhanced multiphoton ionization	17
SHG	second harmonic generation	28
SHRIMP	single-molecule high-resolution imaging with photo-bleaching	44
SLM	spatial light modulator	43
STM	scanning tunneling microscope	4
TPP	tetraphenylporphyrin $C_{44}H_{30}N_4$	6, 47
TLI	Talbot–Lau interferometer	6
UHV	ultra high vacuum	35
UV	ultra violet	i

References

[1] Brand, C. *et al.* "Bragg Diffraction of Large Organic Molecules". *Physical Review Letters* **125,** 033604 (July 2020).

[2] Brand, C. *et al.* "An Atomically Thin Matter-Wave Beamsplitter". *Nature Nanotechnology* **10,** 845–848 (Oct. 2015).

[3] Haslinger, P. *et al.* "A Universal Matter-Wave Interferometer with Optical Ionization Gratings in the Time Domain". *Nature Physics* **9,** 144–148 (Mar. 2013).

[4] Juffmann, T., Ulbricht, H. & Arndt, M. "Experimental Methods of Molecular Matter-Wave Optics". *Reports on Progress in Physics* **76,** 086402 (Aug. 2013).

[5] Fein, Y. Y. *et al.* "Quantum Superposition of Molecules beyond 25 kDa". *Nature Physics* **15,** 1242–1245 (Dec. 2019).

[6] Pedalino, S. *Experiments with the Long-Baseline Matter-Wave Interferometer.* MA thesis (University of Vienna, Vienna, 2020).

[7] Kiałka, F. *et al.* "Concepts for Long-Baseline High-Mass Matter-Wave Interferometry". *Physica Scripta* **94,** 034001 (Mar. 2019).

[8] Nairz, O., Brezger, B., Arndt, M. & Zeilinger, A. "Diffraction of Complex Molecules by Structures Made of Light". *Physical Review Letters* **87,** 160401 (Sept. 2001).

[9] Cotter, J. P. *et al.* "Coherence in the Presence of Absorption and Heating in a Molecule Interferometer". *Nature Communications* **6,** 7336 (Nov. 2015).

[10] Klán, P. & Wirz, J. *Photochemistry of Organic Compounds: From Concepts to Practice* 1st ed. (Wiley, Feb. 2009).

[11] Weinstain, R., Slanina, T., Kand, D. & Klán, P. "Visible-to-NIR-Light Activated Release: From Small Molecules to Nanomaterials". *Chemical Reviews* **120,** 13135–13272 (Dec. 2020).

[12] Einstein, A. "Über einen die Erzeugung und Verwandlung des Lichtes betreffenden heuristischen Gesichtspunkt". *Annalen der Physik* **322,** 132–148 (1905).

[13] de Broglie, L. "Waves and Quanta". *Nature* **112,** 540–540 (Oct. 1923).

[14] Schrödinger, E. "An Undulatory Theory of the Mechanics of Atoms and Molecules". *Physical Review* **28,** 1049–1070 (Dec. 1926).

[15] Davisson, C. & Germer, L. H. "Diffraction of Electrons by a Crystal of Nickel". *Physical Review* **30,** 705–740 (Dec. 1927).

[16] Davisson, C. & Germer, L. H. "The Scattering of Electrons by a Single Crystal of Nickel". *Nature* **119,** 558–560 (Apr. 1927).

[17] Thomson, G. P. & Reid, A. "Diffraction of Cathode Rays by a Thin Film". *Nature* **119,** 890–890 (June 1927).

[18] Rupp, E. "Über Elektronenbeugung an Ionenkristallen". *Annalen der Physik* **395,** 497–506 (1929).

[19] Rupp, E. "Über Elektronenreflexion und Beugung an Einkristallflächen". *Annalen der Physik* **393,** 801–813 (1929).

[20] Bühl, A. "Elektronenbeugung und inneres Potential der Metalle". *Die Naturwissenschaften* **20,** 577–578 (July 1932).

[21] Farnsworth, H. E. "Diffraction of Low-Speed Electrons by Single Crystals of Copper and Silver". *Physical Review* **40,** 684–712 (June 1932).

[22] Young, T. "I. The Bakerian Lecture. Experiments and Calculations Relative to Physical Optics". *Philosophical Transactions of the Royal Society of London* **94,** 1–16 (Nov. 1803).

[23] Möllenstedt, G. & Düker, H. "Beobachtungen und Messungen an Biprisma-Interferenzen mit Elektronenwellen". *Zeitschrift für Physik* **145,** 377–397 (June 1956).

[24] Jönsson, C. "Elektroneninterferenzen an mehreren künstlich hergestellten Feinspalten". *Zeitschrift für Physik* **161,** 454–474 (Aug. 1961).

[25] Möllenstedt, G. "Some Remarks on the Quantum Mechanics of the Electron". *Physica B+C* **151,** 201–205 (July 1988).

[26] Akoury, D. *et al.* "The Simplest Double Slit: Interference and Entanglement in Double Photoionization of H $_2$". *Science* **318,** 949–952 (Nov. 2007).

[27] Aharonov, Y. & Bohm, D. "Significance of Electromagnetic Potentials in the Quantum Theory". *Physical Review* **115,** 485–491 (Aug. 1959).

[28] Chambers, R. G. "Shift of an Electron Interference Pattern by Enclosed Magnetic Flux". *Physical Review Letters* **5,** 3–5 (July 1960).

[29] Boersch, H., Hamisch, H., Grohmann, K. & Wohlleben, D. "Experimenteller Nachweis der Phasenschiebung von Elektronenwellen durch das magnetische Vektorpotential". *Zeitschrift für Physik* **165,** 79–93 (Feb. 1961).

[30] Möllenstedt, G. & Bayh, W. "Kontinuierliche Phasenschiebung von Elektronenwellen im kraftfeldfreien Raum durch das magnetische Vektorpotential eines Solenoids". *Physik Journal* **18,** 299–305 (July 1962).

[31] Tonomura, A. *et al.* "Observation of Aharonov-Bohm Effect by Electron Holography". *Physical Review Letters* **48,** 1443–1446 (May 1982).

[32] Knoll, M. & Ruska, E. "Das Elektronenmikroskop". *Zeitschrift für Physik* **78,** 318–339 (May 1932).

[33] Mulvey, T. "Origins and Historical Development of the Electron Microscope". *British Journal of Applied Physics* **13,** 197–207 (May 1962).

[34] Ruska, E. "The Development of the Electron Microscope and of Electron Microscopy". *Reviews of Modern Physics* **59,** 627–638 (July 1987).

[35] Rüdenberg, R. in *Advances in Imaging and Electron Physics* 171–205 (Elsevier, 2010).

[36] Kapitza, P. L. & Dirac, P. A. M. "The Reflection of Electrons from Standing Light Waves". *Mathematical Proceedings of the Cambridge Philosophical Society* **29,** 297–300 (May 1933).

[37] Freimund, D. L., Aflatooni, K. & Batelaan, H. "Observation of the Kapitza–Dirac Effect". *Nature* **413,** 142–143 (Sept. 2001).

[38] Bucksbaum, P. H., Schumacher, D. W. & Bashkansky, M. "High-Intensity Kapitza-Dirac Effect". *Physical Review Letters* **61,** 1182–1185 (Sept. 1988).

[39] Crommie, M. F., Lutz, C. P. & Eigler, D. M. "Confinement of Electrons to Quantum Corrals on a Metal Surface". *Science* **262,** 218–220 (Oct. 1993).

[40] Ji, Y. *et al.* "An Electronic Mach–Zehnder Interferometer". *Nature* **422,** 415–418 (Mar. 2003).

[41] Gronniger, G., Barwick, B. & Batelaan, H. "A Three-Grating Electron Interferometer". *New Journal of Physics* **8,** 224–224 (Oct. 2006).

[42] Uchida, M. & Tonomura, A. "Generation of Electron Beams Carrying Orbital Angular Momentum". *Nature* **464,** 737–739 (Apr. 2010).

[43] Verbeeck, J., Tian, H. & Schattschneider, P. "Production and Application of Electron Vortex Beams". *Nature* **467,** 301–304 (Sept. 2010).

[44] McMorran, B. J. *et al.* "Electron Vortex Beams with High Quanta of Orbital Angular Momentum". *Science* **331,** 192–195 (Jan. 2011).

[45] Hasselbach, F. "Progress in Electron- and Ion-Interferometry". *Reports on Progress in Physics* **73,** 016101 (Jan. 2010).

[46] Chadwick, J. "Possible Existence of a Neutron". *Nature* **129,** 312–312 (Feb. 1932).

[47] Mitchell, D. P. & Powers, P. N. "Bragg Reflection of Slow Neutrons". *Physical Review* **50,** 486–487 (Sept. 1936).

[48] von Halban, H. "Preuve Experimentale de La Diffraction Des Neutrons". *Acad. Sci. Paris* **203,** 73–75 (1936).

[49] Rupp, E. "Beugung schneller Protonen an Goldfolien". *Zeitschrift für Physik* **78,** 722–727 (Nov. 1932).

[50] Maier-Leibnitz, H. & Springer, T. "Ein Interferometer Für Langsame Neutronen". *Zeitschrift für Physik* **167,** 386–402 (Aug. 1962).

[51] Shull, C. G. "Single-Slit Diffraction of Neutrons". *Physical Review* **179,** 752–754 (Mar. 1969).

[52] Kurz, H. & Rauch, H. "Beugung thermischer Neutronen an einem Strichgitter". *Zeitschrift für Physik A Hadrons and nuclei* **220,** 419–426 (Oct. 1969).

[53] Zeilinger, A., Gähler, R., Shull, C. G., Treimer, W. & Mampe, W. "Single- and Double-Slit Diffraction of Neutrons". *Reviews of Modern Physics* **60,** 1067–1073 (Oct. 1988).

[54] Eder, K., Gruber, M., Zeilinger, A., Gähler, R. & Mampe, W. "Diffraction of Very Cold Neutrons at Phase Gratings". *Physica B: Condensed Matter* **172,** 329–338 (June 1991).

[55] Rauch, H., Treimer, W. & Bonse, U. "Test of a Single Crystal Neutron Interferometer". *Physics Letters A* **47,** 369–371 (Apr. 1974).

[56] Colella, R., Overhauser, A. W. & Werner, S. A. "Observation of Gravitationally Induced Quantum Interference". *Physical Review Letters* **34,** 1472–1474 (June 1975).

[57] Anandan, J. "Gravitational and Rotational Effects in Quantum Interference". *Physical Review D* **15,** 1448–1457 (Mar. 1977).

[58] Rauch, H. *et al.* "Verification of Coherent Spinor Rotation of Fermions". *Physics Letters A* **54,** 425–427 (Oct. 1975).

[59] Rupp, R. A., Hehmann, J., Matull, R. & Ibel, K. "Neutron Diffraction from Photoinduced Gratings in a PMMA Matrix". *Physical Review Letters* **64,** 301–302 (Jan. 1990).

[60] Schellhorn, U., Rupp, R. A., Breer, S. & May, R. P. "The First Neutron Interferometer Built of Holographic Gratings". *Physica B: Condensed Matter* **234–236,** 1068–1070 (June 1997).

[61] Hasegawa, Y., Loidl, R., Badurek, G., Baron, M. & Rauch, H. "Violation of a Bell-like Inequality in Single-Neutron Interferometry". *Nature* **425,** 45–48 (Sept. 2003).

[62] Hasegawa, Y. *et al.* "Engineering of Triply Entangled States in a Single-Neutron System". *Physical Review A* **81,** 032121 (Mar. 2010).

[63] Danner, A. *et al. Three-Path Quantum Cheshire Cat Observed in Neutron Interferometry.* Mar. 2023. arXiv: `2303.18092 [quant-ph]`.

[64] Rauch, H. & Werner, S. A. *Neutron Interferometry: Lessons in Experimental Quantum Mechanics, Wave-Particle Duality, and Entanglement* Second Edition (Oxford University Press, Oxford, United Kingdom, 2015).

[65] Stern, O. "Beugung von Molekularstrahlen am Gitter einer Krystallspaltfläche". *Die Naturwissenschaften* **17,** 391–391 (May 1929).

[66] Estermann, I. & Stern, O. "Beugung von Molekularstrahlen". *Zeitschrift für Physik* **61,** 95–125 (Jan. 1930).

[67] Altshuler, S., Frantz, L. M. & Braunstein, R. "Reflection of Atoms from Standing Light Waves". *Physical Review Letters* **17,** 231–232 (Aug. 1966).

[68] Moskowitz, P. E., Gould, P. L., Atlas, S. R. & Pritchard, D. E. "Diffraction of an Atomic Beam by Standing-Wave Radiation". *Physical Review Letters* **51,** 370–373 (Aug. 1983).

[69] Gould, P. L., Ruff, G. A. & Pritchard, D. E. "Diffraction of Atoms by Light: The near-Resonant Kapitza-Dirac Effect". *Physical Review Letters* **56,** 827–830 (Feb. 1986).

[70] Bernhardt, A. F. & Shore, B. W. "Coherent Atomic Deflection by Resonant Standing Waves". *Physical Review A* **23,** 1290–1301 (Mar. 1981).

[71] Grinchuk, V. *et al.* "Scattering of an Atomic Beam by a Short Light Pulse". *Physics Letters A* **86,** 136–138 (Nov. 1981).

[72] Martin, P., Oldaker, B., Miklich, A. & Pritchard, D. "Bragg Scattering of Atoms from a Standing Light Wave". *Physical Review Letters* **60,** 515–518 (Feb. 1988).

[73] Keith, D. W., Schattenburg, M. L., Smith, H. I. & Pritchard, D. E. "Diffraction of Atoms by a Transmission Grating". *Physical Review Letters* **61,** 1580–1583 (Oct. 1988).

[74] Carnal, O. & Mlynek, J. "Young's Double-Slit Experiment with Atoms: A Simple Atom Interferometer". *Physical Review Letters* **66,** 2689–2692 (May 1991).

[75] Shimizu, F., Shimizu, K. & Takuma, H. "Double-Slit Interference with Ultracold Metastable Neon Atoms". *Physical Review A* **46,** R17–R20 (July 1992).

[76] Keith, D. W., Ekstrom, C. R., Turchette, Q. A. & Pritchard, D. E. "An Interferometer for Atoms". *Physical Review Letters* **66,** 2693–2696 (May 1991).

[77] Rasel, E. M., Oberthaler, M. K., Batelaan, H., Schmiedmayer, J. & Zeilinger, A. "Atom Wave Interferometry with Diffraction Gratings of Light". *Physical Review Letters* **75,** 2633–2637 (Oct. 1995).

[78] Bordé, C. "Atomic Interferometry with Internal State Labelling". *Physics Letters A* **140,** 10–12 (Sept. 1989).

[79] Riehle, F., Kisters, T., Witte, A., Helmcke, J. & Bordé, C. J. "Optical Ramsey Spectroscopy in a Rotating Frame: Sagnac Effect in a Matter-Wave Interferometer". *Physical Review Letters* **67,** 177–180 (July 1991).

[80] Kasevich, M. & Chu, S. "Atomic Interferometry Using Stimulated Raman Transitions". *Physical Review Letters* **67,** 181–184 (July 1991).

[81] Clauser, J. F. "Ultra-High Sensitivity Accelerometers and Gyroscopes Using Neutral Atom Matter-Wave Interferometry". *Physica B+C* **151,** 262–272 (July 1988).

[82] Kasevich, M. & Chu, S. "Measurement of the Gravitational Acceleration of an Atom with a Light-Pulse Atom Interferometer". *Applied Physics B Photophysics and Laser Chemistry* **54,** 321–332 (May 1992).

[83] Gustavson, T. L., Bouyer, P. & Kasevich, M. A. "Precision Rotation Measurements with an Atom Interferometer Gyroscope". *Physical Review Letters* **78,** 2046–2049 (Mar. 1997).

[84] Snadden, M., McGuirk, J., Bouyer, P., Haritos, K. & Kasevich, M. "Measurement of the Earth's Gravity Gradient with an Atom Interferometer-Based Gravity Gradiometer". *Physical Review Letters* **81,** 971–974 (Aug. 1998).

[85] Gustavson, T. L., Landragin, A. & Kasevich, M. A. "Rotation Sensing with a Dual Atom-Interferometer Sagnac Gyroscope". *Classical and Quantum Gravity* **17,** 2385–2398 (June 2000).

[86] Peters, A., Chung, K. Y. & Chu, S. "High-Precision Gravity Measurements Using Atom Interferometry". *Metrologia* **38,** 25–61 (Feb. 2001).

[87] McGuirk, J. M., Foster, G. T., Fixler, J. B., Snadden, M. J. & Kasevich, M. A. "Sensitive Absolute-Gravity Gradiometry Using Atom Interferometry". *Physical Review A* **65,** 033608 (Feb. 2002).

[88] Dubetsky, B. & Kasevich, M. A. "Atom Interferometer as a Selective Sensor of Rotation or Gravity". *Physical Review A* **74,** 023615 (Aug. 2006).

[89] Stockton, J. K., Takase, K. & Kasevich, M. A. "Absolute Geodetic Rotation Measurement Using Atom Interferometry". *Physical Review Letters* **107,** 133001 (Sept. 2011).

[90] Asenbaum, P., Overstreet, C., Kim, M., Curti, J. & Kasevich, M. A. "Atom-Interferometric Test of the Equivalence Principle at the 10 - 12 Level". *Physical Review Letters* **125,** 191101 (Nov. 2020).

[91] Shimizu, F., Shimizu, K. & Takuma, H. "Stark Phase Shift and Deflection in the Ultracold Atomic Interferometer". *Japanese Journal of Applied Physics* **31,** L436 (Apr. 1992).

[92] Rieger, V., Sengstock, K., Sterr, U., Müller, J. & Ertmer, W. "Atom-Interferometric Determination of the Dc-Stark Shift of the Mg-intercombination Line". *Optics Communications* **99,** 172–176 (June 1993).

[93] Ekstrom, C. R., Schmiedmayer, J., Chapman, M. S., Hammond, T. D. & Pritchard, D. E. "Measurement of the Electric Polarizability of Sodium with an Atom Interferometer". *Physical Review A* **51,** 3883–3888 (May 1995).

[94] Miffre, A., Jacquey, M., Büchner, M., Trénec, G. & Vigué, J. "Atom Interferometry Measurement of the Electric Polarizability of Lithium". *The European Physical Journal D* **38,** 353–365 (May 2006).

[95] Fein, Y. Y. *et al.* "Quantum-Assisted Measurement of Atomic Diamagnetism". *Physical Review X* **10,** 011014 (Jan. 2020).

[96] Gupta, S., Dieckmann, K., Hadzibabic, Z. & Pritchard, D. E. "Contrast Interferometry Using Bose-Einstein Condensates to Measure h / m and α". *Physical Review Letters* **89,** 140401 (Sept. 2002).

[97] Fattori, M., Lamporesi, G., Petelski, T., Stuhler, J. & Tino, G. "Towards an Atom Interferometric Determination of the Newtonian Gravitational Constant". *Physics Letters A* **318,** 184–191 (Nov. 2003).

[98] Rosi, G., Sorrentino, F., Cacciapuoti, L., Prevedelli, M. & Tino, G. M. "Precision Measurement of the Newtonian Gravitational Constant Using Cold Atoms". *Nature* **510,** 518–521 (June 2014).

[99] Parker, R. H., Yu, C., Zhong, W., Estey, B. & Müller, H. "Measurement of the Fine-Structure Constant as a Test of the Standard Model". *Science* **360,** 191–195 (Apr. 2018).

[100] Weitz, M., Young, B. C. & Chu, S. "Atomic Interferometer Based on Adiabatic Population Transfer". *Physical Review Letters* **73,** 2563–2566 (Nov. 1994).

[101] Clauser, J. F. & Li, S. "Talbot-vonLau Atom Interferometry with Cold Slow Potassium". *Physical Review A* **49,** R2213–R2216 (Apr. 1994).

[102] Giltner, D. M., McGowan, R. W. & Lee, S. A. "Theoretical and Experimental Study of the Bragg Scattering of Atoms from a Standing Light Wave". *Physical Review A* **52,** 3966–3972 (Nov. 1995).

[103] Müller, H., Chiow, S.-w., Long, Q., Herrmann, S. & Chu, S. "Atom Interferometry with up to 24-Photon-Momentum-Transfer Beam Splitters". *Physical Review Letters* **100,** 180405 (May 2008).

[104] Chiow, S.-w., Kovachy, T., Chien, H.-C. & Kasevich, M. A. "102 $\hbar$ k Large Area Atom Interferometers". *Physical Review Letters* **107,** 130403 (Sept. 2011).

[105] Fujita, J. *et al.* "Manipulation of an Atomic Beam by a Computer-Generated Hologram". *Nature* **380,** 691–694 (Apr. 1996).

[106] Morinaga, M. *et al.* "Holographic Manipulation of a Cold Atomic Beam". *Physical Review Letters* **77,** 802–805 (July 1996).

[107] Doak, R. B. *et al.* "Towards Realization of an Atomic de Broglie Microscope: Helium Atom Focusing Using Fresnel Zone Plates". *Physical Review Letters* **83,** 4229–4232 (Nov. 1999).

[108] Shimizu, F. & Fujita, J.-i. "Reflection-Type Hologram for Atoms". *Physical Review Letters* **88,** 123201 (Mar. 2002).

[109] Anderson, M. H., Ensher, J. R., Matthews, M. R., Wieman, C. E. & Cornell, E. A. "Observation of Bose-Einstein Condensation in a Dilute Atomic Vapor". *Science* **269,** 198–201 (July 1995).

[110] Davis, K. B. *et al.* "Bose-Einstein Condensation in a Gas of Sodium Atoms". *Physical Review Letters* **75,** 3969–3973 (Nov. 1995).

[111] Wang, Y.-J. *et al.* "Atom Michelson Interferometer on a Chip Using a Bose-Einstein Condensate". *Physical Review Letters* **94,** 090405 (Mar. 2005).

[112] Judd, T. E. *et al.* "Zone-Plate Focusing of Bose–Einstein Condensates for Atom Optics and Erasable High-Speed Lithography of Quantum Electronic Components". *New Journal of Physics* **12,** 063033 (June 2010).

[113] Kohstall, C. *et al.* "Observation of Interference between Two Molecular Bose–Einstein Condensates". *New Journal of Physics* **13,** 065027 (June 2011).

[114] Müntinga, H. *et al.* "Interferometry with Bose-Einstein Condensates in Microgravity". *Physical Review Letters* **110,** 093602 (Feb. 2013).

[115] Ufrecht, C., Roura, A. & Schleich, W. P. *Bose-Einstein Condensates in Microgravity and Fundamental Tests of Gravity.* July 2021. arXiv: `2107.03709 [physics, physics:quant-ph]`.

[116] Schöllkopf, W. & Toennies, J. P. "Nondestructive Mass Selection of Small van Der Waals Clusters". *Science* **266,** 1345–1348 (Nov. 1994).

[117] Bordé, C., Courtier, N., du Burck, F., Goncharov, A. & Gorlicki, M. "Molecular Interferometry Experiments". *Physics Letters A* **188,** 187–197 (May 1994).

[118] Chapman, M. S. *et al.* "Optics and Interferometry with Na 2 Molecules". *Physical Review Letters* **74,** 4783–4786 (June 1995).

[119] Arndt, M. *et al.* "Wave–Particle Duality of C60 Molecules". *Nature* **401,** 680–682 (Oct. 1999).

[120] Juffmann, T. *et al.* "Real-Time Single-Molecule Imaging of Quantum Interference". *Nature Nanotechnology* **7,** 297–300 (May 2012).

[121] Brand, C. *et al.* "A Green's Function Approach to Modeling Molecular Diffraction in the Limit of Ultra-Thin Gratings". *Annalen der Physik* **527,** 580–591 (Oct. 2015).

[122] Knobloch, C. *et al.* "On the Role of the Electric Dipole Moment in the Diffraction of Biomolecules at Nanomechanical Gratings". *Fortschritte der Physik* **65,** 1600025 (June 2017).

[123] Brezger, B., Arndt, M. & Zeilinger, A. "Concepts for Near-Field Interferometers with Large Molecules". *Journal of Optics B: Quantum and Semiclassical Optics* **5,** S82–S89 (Apr. 2003).

[124] Brezger, B. *et al.* "Matter-Wave Interferometer for Large Molecules". *Physical Review Letters* **88,** 100404 (Feb. 2002).

[125] Hackermüller, L. *et al.* "Wave Nature of Biomolecules and Fluorofullerenes". *Physical Review Letters* **91,** 090408 (Aug. 2003).

[126] Berninger, M., Stefanov, A., Deachapunya, S. & Arndt, M. "Polarizability Measurements of a Molecule via a Near-Field Matter-Wave Interferometer". *Physical Review A* **76,** 013607 (July 2007).

[127] Gerlich, S. *et al.* "A Kapitza–Dirac–Talbot–Lau Interferometer for Highly Polarizable Molecules". *Nature Physics* **3,** 711–715 (Oct. 2007).

[128] Hornberger, K. *et al.* "Theory and Experimental Verification of Kapitza–Dirac–Talbot–Lau Interferometry". *New Journal of Physics* **11,** 043032 (Apr. 2009).

[129] Hackermüller, L. *et al.* "Optical Polarizabilities of Large Molecules Measured in Near-Field Interferometry". *Applied Physics B* **89,** 469–473 (Dec. 2007).

[130] Gerlich, S. *et al.* "Matter-Wave Metrology as a Complementary Tool for Mass Spectrometry". *Angewandte Chemie International Edition* **47,** 6195–6198 (Aug. 2008).

[131] Gring, M. *et al.* "Influence of Conformational Molecular Dynamics on Matter Wave Interferometry". *Physical Review A* **81,** 031604 (Mar. 2010).

[132] Eibenberger, S., Gerlich, S., Arndt, M., Tüxen, J. & Mayor, M. "Electric Moments in Molecule Interferometry". *New Journal of Physics* **13,** 043033 (Apr. 2011).

[133] Mairhofer, L. *et al.* "Quantum-Assisted Metrology of Neutral Vitamins in the Gas Phase". *Angewandte Chemie International Edition* **56,** 10947–10951 (Aug. 2017).

[134] Tüxen, J., Gerlich, S., Eibenberger, S., Arndt, M. & Mayor, M. "Quantum Interference Distinguishes between Constitutional Isomers". *Chemical Communications* **46,** 4145 (2010).

[135] Brand, C. *et al.* "Conformer Selection by Matter-Wave Interference". *Physical Review Letters* **121,** 173002 (Oct. 2018).

[136] Gerlich, S. *et al.* "Quantum Interference of Large Organic Molecules". *Nature Communications* **2,** 263 (Sept. 2011).

[137] Eibenberger, S., Gerlich, S., Arndt, M., Mayor, M. & Tüxen, J. "Matter–Wave Interference of Particles Selected from a Molecular Library with Masses Exceeding 10 000 Amu". *Physical Chemistry Chemical Physics* **15,** 14696 (2013).

[138] Jochim, S. *et al.* "Bose-Einstein Condensation of Molecules". *Science* **302,** 2101–2103 (Dec. 2003).

[139] Regal, C. A., Ticknor, C., Bohn, J. L. & Jin, D. S. "Creation of Ultracold Molecules from a Fermi Gas of Atoms". *Nature* **424,** 47–50 (July 2003).

[140] Zwierlein, M. W. *et al.* "Observation of Bose-Einstein Condensation of Molecules". *Physical Review Letters* **91,** 250401 (Dec. 2003).

[141] Bell, M. T. & P. Softley, T. "Ultracold Molecules and Ultracold Chemistry". *Molecular Physics* **107,** 99–132 (Jan. 2009).

[142] Dörre, N. *et al.* "Photofragmentation Beam Splitters for Matter-Wave Interferometry". *Physical Review Letters* **113,** 233001 (Dec. 2014).

[143] Rodewald, J. *et al.* "Isotope-Selective High-Order Interferometry with Large Organic Molecules in Free Fall". *New Journal of Physics* **20,** 033016 (Mar. 2018).

[144] Shayeghi, A. *et al.* "Matter-Wave Interference of a Native Polypeptide". *Nature Communications* **11,** 1447 (Dec. 2020).

[145] Bonin, K. D. & Kresin, V. V. *Electric-Dipole Polarizabilities of Atoms, Molecules, and Clusters* (WORLD SCIENTIFIC, Oct. 1997).

[146] Hohm, U. "Polarizabilities of Atoms and Molecules, New Insights into an Old Subject". *Vacuum* **58,** 117–134 (Aug. 2000).

[147] Miller, T. M. & Bederson, B. in *Advances in Atomic and Molecular Physics* 1–55 (Elsevier, 1978).

[148] Mitroy, J., Safronova, M. S. & Clark, C. W. "Theory and Applications of Atomic and Ionic Polarizabilities". *Journal of Physics B: Atomic, Molecular and Optical Physics* **43,** 202001 (Oct. 2010).

[149] Atkins, P. W. & Friedman, R. *Molecular Quantum Mechanics* 3. ed., reprint. (with corr.). (Univ. Press, Oxford [u.a.], 1997).

[150] Steck, D. A. *Quantum and Atom Optics* (June 2023).

[151] Bogaard, M. P. & Orr, B. J. in *Molecular Structure and Properties* (ed Buckingham, A. D.) 149–194 (Butterworths, London ; Boston, 1975).

[152] Berestetskii, V. B., Lifshits, E. M., Pitaevskii, L. P., Sykes, J. B. & Bell, J. S. *Quantum Electrodynamics* 2nd ed (Butterworth-Heinemann, Oxford, 1982).

[153] Krems, R. V. *Molecules in Electromagnetic Fields: From Ultracold Physics to Controlled Chemistry* 1st edition (John Wiley & Sons, Hoboken, NJ, 2019).

[154] Sakurai, J. J. & Napolitano, J. *Modern Quantum Mechanics:* 2nd ed. (Cambridge University Press, Sept. 2017).

[155] Bishop, D. M. "Molecular Vibrational and Rotational Motion in Static and Dynamic Electric Fields". *Reviews of Modern Physics* **62,** 343–374 (Apr. 1990).

[156] Hu, A., York, D. M. & Woo, T. K. "Time-Dependent Density Functional Theory Calculations of Molecular Static and Dynamic Polarizabilities, Cauchy Coefficients and Their Anisotropies with Atomic Numerical Basis Functionsq". *Journal of Molecular Structure* (2002).

[157] Mkadmh, A. M., Hinchliffe, A. & Abu-Awwad, F. M. "Atom Additive Model Based on Dipole Field Tensor to Compute Static Average Molecular Dipole Polarizabilities". *Journal of Molecular Structure: THEOCHEM* **901,** 9–17 (May 2009).

[158] Lopes, P. E. M., Roux, B. & MacKerell, A. D. "Molecular Modeling and Dynamics Studies with Explicit Inclusion of Electronic Polarizability: Theory and Applications". *Theoretical Chemistry Accounts* **124,** 11–28 (Sept. 2009).

[159] Miller, K. J. "Calculation of the Molecular Polarizability Tensor". *Journal of the American Chemical Society* **112,** 8543–8551 (Nov. 1990).

[160] Applequist, J., Carl, J. R. & Fung, K.-K. "Atom Dipole Interaction Model for Molecular Polarizability. Application to Polyatomic Molecules and Determination of Atom Polarizabilities". *Journal of the American Chemical Society* **94,** 2952–2960 (May 1972).

[161] Booth, L. S. *et al.* "Modelling of the Dynamic Polarizability of Macromolecules for Single-Molecule Optical Biosensing". *Scientific Reports* **12,** 1995 (Feb. 2022).

[162] Kang, Y. K. & Jhon, M. S. "Additivity of Atomic Static Polarizabilities and Dispersion Coefficients". *Theoretica Chimica Acta* **61,** 41–48 (1982).

[163] Laidig, K. E. "Atomic Origins of Molecular Polarizabilities". *Canadian Journal of Chemistry* **74,** 1131–1138 (June 1996).

[164] Miller, K. J. "Additivity Methods in Molecular Polarizability". *Journal of the American Chemical Society* **112,** 8533–8542 (Nov. 1990).

[165] Hohm, U. & Kerl, K. "A Michelson Twin Interferometer for Precise Measurements of the Refractive Index of Gases between 100 K and 1300 K". *Measurement Science and Technology* **1,** 329–336 (Apr. 1990).

[166] Kerl, K., Hohm, U. & Varchmin, H. "Polarizability α (ω, T, ρ) of Small Molecules in the Gas Phase". *Berichte der Bunsengesellschaft für physikalische Chemie* **96,** 728–733 (May 1992).

[167] Miller, T. M. & Bederson, B. in *Advances in Atomic and Molecular Physics* 37–60 (Elsevier, 1989).

[168] Maltsev, V. A., Nerushev, O. A., Novopashin, S. A. & Selivanov, B. A. "Anomalous Polarizability of Fullerene". *Chemical Physics Letters* **212,** 480–482 (Sept. 1993).

[169] Miles, R. B., Lempert, W. R. & Forkey, J. N. "Laser Rayleigh Scattering". *Measurement Science and Technology* **12,** R33–R51 (May 2001).

[170] Holmgren, W. F., Revelle, M. C., Lonij, V. P. A. & Cronin, A. D. "Absolute and Ratio Measurements of the Polarizability of Na, K, and Rb with an Atom Interferometer". *Physical Review A* **81,** 053607 (May 2010).

[171] Fein, Y. Y., Geyer, P., Kiałka, F., Gerlich, S. & Arndt, M. "Improved Accuracy Fullerene Polarizability Measurements in a Long-Baseline Matter-Wave Interferometer". *Physical Review Research* **1,** 033158 (Dec. 2019).

[172] Lakowicz, J. R. & Masters, B. R. "Principles of Fluorescence Spectroscopy, Third Edition". *Journal of Biomedical Optics* **13,** 029901 (2008).

[173] Jablonski, A. "Efficiency of Anti-Stokes Fluorescence in Dyes". *Nature* **131,** 839–840 (June 1933).

[174] *Fundamentals of Fluorescence Imaging* (ed Cox, G. C.) (Jenny Stanford Publishing, Singapore, 2018).

[175] Turro, N. J. *Modern Molecular Photochemistry* (Benjamin/Cummings Pub. Co, Menlo Park, Calif, 1978).

[176] Jameson, D. M. *Introduction to Fluorescence* (CRC Press, Taylor & Francis Group, Boca Raton, 2014).

[177] Valeur, B. *Molecular Fluorescence: Principles and Applications* (Wiley-VCH, Weinheim ; New York, 2002).

[178] Kubitscheck, U. *Fluorescence Microscopy: From Principles to Biological Applications* 2nd ed (Wiley-VCH, Weinheim, 2017).

[179] Smalley, R. E. "Vibrational Randomization Measurements with Supersonic Beams". *The Journal of Physical Chemistry* **86,** 3504–3512 (Sept. 1982).

[180] Uzer, T. & Miller, W. "Theories of Intramolecular Vibrational Energy Transfer". *Physics Reports* **199,** 73–146 (Jan. 1991).

[181] Baer, T. & Hase, W. L. *Unimolecular Reaction Dynamics: Theory and Experiments* (Oxford University Press, New York, 1996).

[182] Wayne, R. P. *Photochemistry* (Butterworths, London, 1970).

[183] Štacko, P. & Šolomek, T. "Photoremovable Protecting Groups: Across the Light Spectrum to Near-Infrared Absorbing Photocages". *CHIMIA* **75,** 873 (Oct. 2021).

[184] Hansen, M. J. "Wavelength-Selective Cleavage of Photoprotecting Groups: Strategies and Applications in Dynamic Systems". *Chem Soc Rev* (2015).

[185] Schätti, J. *et al.* "Neutralization of Insulin by Photocleavage under High Vacuum". *Chemical Communications* **55,** 12507–12510 (2019).

[186] Hua, Y. *et al.* "Giving the Green Light to Photochemical Uncaging of Large Biomolecules in High Vacuum". *JACS Au* **3,** 2790–2799 (Oct. 2023).

[187] Klán, P. *et al.* "Photoremovable Protecting Groups in Chemistry and Biology: Reaction Mechanisms and Efficacy". *Chemical Reviews* **113,** 119–191 (Jan. 2013).

[188] Barltrop, J. A., Plant, P. J. & Schofield, P. "Photosensitive Protective Groups". *Chemical Communications (London),* 822–823 (Jan. 1966).

[189] Šolomek, T., Wirz, J. & Klán, P. "Searching for Improved Photoreleasing Abilities of Organic Molecules". *Accounts of Chemical Research* **48,** 3064–3072 (Dec. 2015).

[190] Minezawa, N. & Gordon, M. S. "Photoisomerization of Stilbene: A Spin-Flip Density Functional Theory Approach". *The Journal of Physical Chemistry A* **115,** 7901–7911 (July 2011).

[191] Cattaneo, P. & Persico, M. "An Abinitio Study of the Photochemistry of Azobenzene". *Physical Chemistry Chemical Physics* **1,** 4739–4743 (Jan. 1999).

[192] *Photochromism: Molecules and Systems* Rev. ed (eds Dürr, H. & Bouas-Laurent, H.) (Elsevier, Amsterdam ; Boston, 2003).

[193] Fukaminato, T. *et al.* "Single-Molecule Fluorescence Photoswitching of a Diarylethene-Perylenebisimide Dyad: Non-destructive Fluorescence Readout". *Journal of the American Chemical Society* **133,** 4984–4990 (Apr. 2011).

[194] Szymański, W., Beierle, J. M., Kistemaker, H. A. V., Velema, W. A. & Feringa, B. L. "Reversible Photocontrol of Biological Systems by the Incorporation of Molecular Photoswitches". *Chemical Reviews* **113,** 6114–6178 (Aug. 2013).

[195] Irie, M., Fukaminato, T., Matsuda, K. & Kobatake, S. "Photochromism of Diarylethene Molecules and Crystals: Memories, Switches, and Actuators". *Chemical Reviews* **114,** 12174–12277 (Dec. 2014).

[196] Fukaminato, T., Ishida, S. & Métivier, R. "Photochromic Fluorophores at the Molecular and Nanoparticle Levels: Fundamentals and Applications of Diarylethenes". *NPG Asia Materials* **10,** 859–881 (Sept. 2018).

[197] Li, Z., He, C., Lu, Z., Li, P. & Zhu, Y.-P. "Recent Progress in All-Visible-Light-Triggered Diarylethenes". *Dyes and Pigments* **182,** 108623 (Nov. 2020).

[198] Weinkauf, R., Schermann, J.-P., de Vries, M. & Kleinermanns, K. "Molecular Physics of Building Blocks of Life under Isolated or Defined Conditions". *The European Physical Journal D - Atomic, Molecular, Optical and Plasma Physics* **20,** 309–316 (Sept. 2002).

[199] De Vries, M. S. & Hobza, P. "Gas-Phase Spectroscopy of Biomolecular Building Blocks". *Annual Review of Physical Chemistry* **58,** 585–612 (May 2007).

[200] *Gas-Phase IR Spectroscopy and Structure of Biological Molecules* (eds Rijs, A. M. & Oomens, J.) (Springer International Publishing, Cham, 2015).

[201] Nimmrichter, S., Hornberger, K., Ulbricht, H. & Arndt, M. "Absolute Absorption Spectroscopy Based on Molecule Interferometry". *Physical Review A* **78,** 063607 (Dec. 2008).

[202] Rodewald, J. *et al.* "New Avenues for Matter-Wave-Enhanced Spectroscopy". *Applied Physics B* **123,** 3 (Jan. 2017).

[203] Arndt, M. *et al.* "Matter-Wave Interferometry with Composite Quantum Objects". *arXiv:1501.07770 [quant-ph].* arXiv: `1501.07770 [quant-ph]` (Jan. 2015).

[204] Hecht, E. *Optics* 4th (Addison Wesley, San Francisco, 2002).

[205] Nimmrichter, S. & Hornberger, K. "Theory of Near-Field Matter-Wave Interference beyond the Eikonal Approximation". *Physical Review A* **78,** 023612 (Aug. 2008).

[206] Pauly, H. *Atom, Molecule, and Cluster Beams I* (Springer Berlin Heidelberg, Berlin, Heidelberg, 2000).

[207] Sclafani, M. *Molecular Beam Methods for Quantum Optics Experiments: Sources, Detection Schemes and Coherent Manipulation.* PhD thesis (University of Vienna, Vienna, 2013).

[208] Scoles, G. *Atomic and Molecular Beam Methods : 1 (1988)* (Oxford Univ. Press, Oxford [u.a.], 1988).

[209] Goodman, J. W. *Statistical Optics* 2nd ed. (Wiley, Hoboken, New Jersey, 2015).

[210] Hornberger, K., Gerlich, S., Haslinger, P., Nimmrichter, S. & Arndt, M. "Colloquium: Quantum Interference of Clusters and Molecules". *Reviews of Modern Physics* **84,** 157–173. arXiv: `1109.5937` (Feb. 2012).

[211] Baumgratz, T., Cramer, M. & Plenio, M. B. "Quantifying Coherence". *Physical Review Letters* **113,** 140401 (Sept. 2014).

[212] Saleh, B. E. A. & Teich, M. C. *Fundamentals of Photonics* 3rd (Wiley, USA, 2019).

[213] Tumulka, R., Viale, A. & Zanghì, N. "Reduced Coherence in Double-Slit Diffraction of Neutrons". *Physical Review A* **75,** 055602 (May 2007).

[214] Cotter, J. P. *et al.* "In Search of Multipath Interference Using Large Molecules". *Science Advances* **3,** e1602478 (Aug. 2017).

[215] Brand, C., Troyer, S., Knobloch, C., Cheshnovsky, O. & Arndt, M. "Single-, Double-, and Triple-Slit Diffraction of Molecular Matter-Waves". *arXiv:2108.06565 [quant-ph].* arXiv: `2108.06565 [quant-ph]` (Aug. 2021).

[216] Juffmann, T., Nimmrichter, S., Arndt, M., Gleiter, H. & Hornberger, K. "New Prospects for de Broglie Interferometry: Grating Diffraction in the Far-Field and Poisson's Spot in the Near-Field". *Foundations of Physics* **42,** 98–110 (Jan. 2012).

[217] Walter, K. *Coherence and Decoherence in High-mass Matter-wave Interferometry.* PhD thesis (Duisburg-Essen, Duisburg, Sept. 2016).

[218] Cronin, A. D., Schmiedmayer, J. & Pritchard, D. E. “Optics and Interferometry with Atoms and Molecules”. *Reviews of Modern Physics* **81,** 1051–1129 (July 2009).

[219] Hornberger, K., Sipe, J. E. & Arndt, M. “Theory of Decoherence in a Matter Wave Talbot-Lau Interferometer”. *Physical Review A* **70,** 053608 (Nov. 2004).

[220] Nairz, O., Arndt, M. & Zeilinger, A. “Experimental Verification of the Heisenberg Uncertainty Principle for Fullerene Molecules”. *Physical Review A* **65,** 032109 (Feb. 2002).

[221] Franken, P. A., Hill, A. E., Peters, C. W. & Weinreich, G. “Generation of Optical Harmonics”. *Physical Review Letters* **7,** 118–119 (Aug. 1961).

[222] Coherent, Inc. *Operator’s Manual Verdi V-8/V-10 Diode-Pumped Lasers.* Aug. 2005.

[223] Sirah Lasertechnik. *WaveTrain Manual.*

[224] Spectra Physics. in (https://www.spectra-physics.com/f/wavetrain-2-cw-frequency-doubler, Accessed 2023-26-05).

[225] Butcher, P. N. & Cotter, D. *The Elements of Nonlinear Optics. Cambridge Studies in Modern Optics* **9** (Cambridge University Press, Cambridge ; New York, 1990).

[226] Mills, D. L. *Nonlinear Optics: Basic Concepts* (Springer-Verlag, Berlin ; New York, 1991).

[227] Yao, J. & Wang, Y. *Nonlinear Optics and Solid-State Lasers: Advanced Concepts, Tuning-Fundamentals and Applications* (Springer Berlin Heidelberg, Berlin, Heidelberg, 2012).

[228] He, G. & Liu, S. H. *Physics of Nonlinear Optics* (World Scientific, Singapore ; River Edge, NJ, 1999).

[229] New, G. *Introduction to Nonlinear Optics* (Cambridge University Press, Cambridge ; New York, 2011).

[230] Armstrong, J. A., Bloembergen, N., Ducuing, J. & Pershan, P. S. “Interactions between Light Waves in a Nonlinear Dielectric”. *Physical Review* **127,** 1918–1939 (Sept. 1962).

[231] Kleinman, D. A. “Theory of Second Harmonic Generation of Light”. *Physical Review* **128,** 1761–1775 (Nov. 1962).

[232] Maker, P. D., Terhune, R. W., Nisenoff, M. & Savage, C. M. “Effects of Dispersion and Focusing on the Production of Optical Harmonics”. *Physical Review Letters* **8,** 21–22 (Jan. 1962).

[233] Drever, R. W. P. *et al.* “Laser Phase and Frequency Stabilization Using an Optical Resonator”. *Applied Physics B Photophysics and Laser Chemistry* **31,** 97–105 (June 1983).

[234] Boyd, G. D. & Kleinman, D. A. “Parametric Interaction of Focused Gaussian Light Beams”. *Journal of Applied Physics* **39,** 3597–3639 (1968).

[235] Risk, W. P., Gosnell, T. R. & Nurmikko, A. V. *Compact Blue-Green Lasers* (Cambridge University Press, Cambridge, 2003).

[236] Boyd, G. D., Ashkin, A., Dziedzic, J. M. & Kleinman, D. A. “Second-Harmonic Generation of Light with Double Refraction”. *Physical Review* **137,** A1305–A1320 (Feb. 1965).

[237] Kleinman, D. A., Ashkin, A. & Boyd, G. D. “Second-Harmonic Generation of Light by Focused Laser Beams”. *Physical Review* **145,** 338–379 (May 1966).

[238] Brand, C. *et al.* “A Fiber-Based Beam Profiler for High-Power Laser Beams in Confined Spaces and Ultra-High Vacuum”. *Optics Express* **28,** 6164 (Mar. 2020).

[239] Born, M. “Zur Quantenmechanik der Stoßvorgänge”. *Zeitschrift für Physik* **37,** 863–867 (Dec. 1926).

[240] Knobloch, C. G. *Coherent Matter Wave Manipulation Techniques.* PhD thesis (University of Vienna, 2018).

[241] Gordon, M. P., Ha, T. & Selvin, P. R. "Single-Molecule High-Resolution Imaging with Photobleaching". *Proceedings of the National Academy of Sciences* **101,** 6462–6465 (Apr. 2004).

[242] Edwards, L. & Gouterman, M. "Porphyrins: XV. Vapor Absorption Spectra and Stability: Phthalocyanines". *Journal of Molecular Spectroscopy* **33,** 292–310 (Feb. 1970).

[243] Eastwood, D., Edwards, L., Gouterman, M. & Steinfeld, J. "Spectra of Porphyrins: Part VII. Vapor Absorption and Emission of Phthalocyanines". *Journal of Molecular Spectroscopy* **20,** 381–390 (Aug. 1966).

[244] Edwards, L., Dolphin, D., Gouterman, M. & Adler, A. "Porphyrins XVII. Vapor Absorption Spectra and Redox Reactions: Tetraphenylporphins and Porphin". *Journal of Molecular Spectroscopy* **38,** 16–32 (Apr. 1971).

[245] Fonda, H. N. *et al.* "Spectroscopic, Photophysical, and Redox Properties of Some Meso-Substituted Free-Base Porphyrins". *The Journal of Physical Chemistry* **97,** 7024–7033 (July 1993).

[246] Yang, Y.-J., Li, S.-X., Chen, D.-L. & Long, Z.-W. "Geometric Structure, Electronic, and Spectral Properties of Metal-free Phthalocyanine under the External Electric Fields". *ACS Omega* **7,** 41266–41274 (Nov. 2022).

[247] Semyannikov, P. P., Basova, T. V., Grankin, V. M. & Igumenov, I. K. "Vapour Pressure of Some Phthalocyanines". *Journal of Porphyrins and Phthalocyanines* **04,** 271–277 (Apr. 2000).

[248] Claessens, C. G., Hahn, U. & Torres, T. "Phthalocyanines: From Outstanding Electronic Properties to Emerging Applications". *The Chemical Record* **8,** 75–97 (2008).

[249] *Phthalocyanines: Properties and Applications* (eds Leznoff, C. C. & Lever, A. B. P.) (VCH, Weinheim New York Cambridge, 1989).

[250] Seybold, P. G. & Gouterman, M. "Porphyrins: XIII: Fluorescence Spectra and Quantum Yields". *Journal of Molecular Spectroscopy* **31,** 1–13 (Jan. 1969).

[251] Vincett, P. S., Voigt, E. M. & Rieckhoff, K. E. "Phosphorescence and Fluorescence of Phthalocyanines". *The Journal of Chemical Physics* **55,** 4131–4140 (Oct. 1971).

[252] Whalley, M. "182. Conjugated Macrocycles. Part XXXII. Absorption Spectra of Tetrazaporphins and Phthalocyanines. Formation of Pyridine Salts". *Journal of the Chemical Society (Resumed),* 866 (1961).

[253] Ramprasad, R. & Shi, N. "Polarizability of Phthalocyanine Based Molecular Systems: A First-Principles Electronic Structure Study". *Applied Physics Letters* **88,** 222903 (May 2006).

[254] Shayeghi, A. *Private Communication.* 2021.

[255] Marsh, D. & Mink, L. "Microscale Synthesis and Electronic Absorption Spectroscopy of Tetraphenylporphyrin H2(TPP) and Metalloporphyrins ZnII(TPP) and NiII(TPP)". *Journal of Chemical Education* **73,** 1188 (Dec. 1996).

[256] Bonderman, D. P., Cater, E. D. & Bennett, W. E. "Vapor Pressures, Mass Spectra, Magnetic Susceptibilities, and Thermodynamics of Some Phthalocyanine Compounds". *Journal of Chemical & Engineering Data* **15,** 396–400 (July 1970).

[257] Perlovich, G. L., Golubchikov, O. A. & Klueva, M. E. "Thermodynamics of Porphyrin Sublimation". *Journal of Porphyrins and Phthalocyanines* **04,** 699–706 (Dec. 2000).

[258] Mullins, J. A., Adler, A. D. & Hochstrasser, R. M. "Vapor Spectra of Porphyrins". *The Journal of Chemical Physics* **43,** 2548–2550 (Oct. 1965).

[259] Ventura, B., Flamigni, L., Marconi, G., Lodato, F. & Officer, D. L. "Extending the Porphyrin Core: Synthesis and Photophysical Characterization of Porphyrins with π-Conjugated β-Substituents". *New J. Chem.* **32,** 166–178 (2008).

[260] Deachapunya, S. *et al.* "Thermal and Electrical Properties of Porphyrin Derivatives and Their Relevance for Molecule Interferometry". *The Journal of Chemical Physics* **126,** 164304 (Apr. 2007).

[261] Oja, V. & Suuberg, E. M. "Vapor Pressures and Enthalpies of Sublimation of Polycyclic Aromatic Hydrocarbons and Their Derivatives". *Journal of Chemical & Engineering Data* **43,** 486–492 (May 1998).

[262] Thummala, S. *The Characterization of Organic Semiconductors Using UV-visible Spectroscopy.* MA thesis (e College of Graduate Studies Texas A&M University-Kingsville, Texas, Dec. 2015).

[263] Rath, M. C. & Mukherjee, T. "Photophysics of 6,11-Dihydroxynaphthacene-5,12-Dione in Different Organic Solvents". *J. Chem. Soc.* (1997).

[264] Kim, J.-M., Kim, J.-Y., Kim, T.-H., Han, D. K. & Ahn, K.-D. "Color and Fluorescence Imaging with T-Boc-protected Dihydroxynaphthacenedione". *Chemistry Letters* **29,** 360–361 (Apr. 2000).

[265] Shayeghi, A. *Private Communication.* 2022.

[266] Hua, Y. *Private Communication.* 2023.

[267] Mayor, M. *Private Communication.* 2022.

[268] Nimmrichter, S. *Matter Wave Talbot–Lau Interferometry beyond the Eikonal Approximation.* Diploma (Technische Universität München, München, 2007).

[269] Schleich, W. *Quantum Optics in Phase Space* 1st ed (Wiley-VCH, Berlin ; New York, 2001).

[270] Nimmrichter, S. *Macroscopic Matter Wave Interferometry.* PhD thesis (University of Vienna, Vienna, 2013).

[271] Martinetz, L. *Private Communication.* 2023.

[272] Walter, K., Nimmrichter, S. & Hornberger, K. "Multiphoton Absorption in Optical Gratings for Matter Waves". *Physical Review A* **94,** 043637 (Oct. 2016).

[273] Savitzky, A. & Golay, M. J. E. "Smoothing and Differentiation of Data by Simplified Least Squares Procedures." *Analytical Chemistry* **36,** 1627–1639 (July 1964).

[274] Calvete, M., Yang, G. Y. & Hanack, M. "Porphyrins and Phthalocyanines as Materials for Optical Limiting". *Synthetic Metals* **141,** 231–243 (Mar. 2004).

[275] Maeda, Y., Okada, T. & Mataga, N. "Picosecond Spectroscopy of Trans-Thioindigo and the Mechanism of Trans → Cis Photoisomerization". *The Journal of Physical Chemistry* **88,** 1117–1119 (Mar. 1984).

[276] Ross, D. L. "Photochromic Indigoids. I: A Photochromic Element Based on the Cis-Trans Photoisomerization of a Thioindigo Dye". *Applied Optics* **10** (Mar. 1971).

[277] Grellmann, K. H. & Hentzschel, P. "Mechanism of the Photochemical Cis$\rightleftharpoons$trans Isomerization of Thioindigo and 6,6′-Diethoxy-Thioindigo in Solution". *Chemical Physics Letters* **53,** 545–551 (Feb. 1978).

[278] Wyman, G. M. & Zarnegar, B. M. "Excited State Chemistry of Indigoid Dyes. I. Fluorescence versus Cis-Trans Isomerization". *The Journal of Physical Chemistry* **77,** 831–837 (Mar. 1973).

[279] Memming, R. & Kobs, K. "Cis→trans-Photoisomerization of Thioindigo". *Berichte der Bunsengesellschaft für physikalische Chemie* **85,** 238–242 (Mar. 1981).

[280] Rogers, D. A., Margerum, J. D. & Wyman, G. M. "Spectroscopic Studies on Dyes. IV. The Fluorescence Spectra of Thioindigo Dyes". *Journal of the American Chemical Society* **79,** 2464–2468 (May 1957).

[281] Kirsch, A. D. & Wyman, G. M. "Excited State Chemistry of Indigoid Dyes. 5. The Intermediacy of the Triplet State in the Direct Photoisomerization and the Effect of Substituents". *The Journal of Physical Chemistry* **81,** 413–420 (Mar. 1977).

[282] Karstens, T., Kobs, K., Memming, R. & Schroppel, F. "Photoisomerizarion Mechanism of Thioindigo Dyes. Thioindigo in Nonpolar Solvents". *Chemical Physics Letters* **48** (June 1977).

[283] Ibrahim, M. *et al.* "On the Spectroscopic Analyses of Thioindigo Dye". *Spectrochimica Acta Part A: Molecular and Biomolecular Spectroscopy* **113,** 332–336 (Sept. 2013).

[284] Breuer, H.-D. & Jacob, H. "Photoisomerization of Thioindigo Adsorbed on Alumina". *CHEMICAL PHYSICS LETTERS* **73** (1980).

[285] Breuer, H. D., Jacob, H. & Düster, G. "Photoacoustic Study of the Photochemistry of Adsorbed Indigoid Dyes". *Applied Optics* **21,** 41 (Jan. 1982).

[286] Koeppe, B. & Römpp, F. "Reversible Spatial Control in Aqueous Media by Visible Light: A Thioindigo Photoswitch That Is Soluble and Operates Efficiently in Water". *Chemistry - A European Journal* **24,** 14382–14386 (Sept. 2018).

[287] Boice, G., Patrick, B. O., McDonald, R., Bohne, C. & Hicks, R. "Synthesis and Photophysics of Thioindigo Diimines and Related Compounds". *The Journal of Organic Chemistry* **79,** 9196–9205 (Oct. 2014).

[288] Fukunishi, K. *et al.* "Cis/Trans Isomerization of Thioindigo Derivatives Adsorbed on Silica Gel Modified with Octadecyl Groups". *Bulletin of the Chemical Society of Japan* **63,** 3701–3703 (Dec. 1990).

[289] Fukunishi, K. *et al.* "Cis/Trans Isomerization of Perinaphthothioindigo Dye Adsorbed on Silica Gel". *Bulletin of the Chemical Society of Japan* **62,** 3733–3735 (Nov. 1989).

[290] Riley, K. F., Hobson, M. P. & Bence, S. J. *Mathematical Methods for Physics and Engineering : A Comprehensive Guide* 3. ed. (Cambridge Univ. Press, Cambridge, 2006).